Resistive Switching in Transition Metal Oxides for Integrated Non-volatile Memory

by

Sanjoy Kumar Nandi

Australian National University

A thesis submitted for the degree of Doctor of Philosophy

Research School of Physics and Engineering

The Australian National University

17th March 2017

To my Parents…

Disclaimer

Except where otherwise indicated, all the research in this thesis is my own work.

Sanjoy Kumar Nandi

17th March 2017

Acknowledgments

I would like to express my deepest gratitude to Chair of Supervisor panel, Prof. Robert Elliman, for his excellent guidance, caring, patience, and providing me freedom for doing research. His encouragement and fruitful discussions made my research progressive and productive. I also acknowledge to him for offering me the opportunity to do this PhD. I want to thank Prof. Geoffery Bicknell for his support and giving me opportunity to jump from galactic to nano scales. I would like to thank Dr. Dinesh Kumar Venkatachalam, for enormous help and input in my research. Without his help I cannot smoothly complete this dissertation. I acknowledge Prof. Pedro Grande and Dr. Maarten Vos for the help on the electron Rutherford back scattering (ERBS) measurements and analysis, and introducing me to ERBS. Their contribution was most essential part of material synthesis and characterization.

I would also like to thank Dr. TayHun Kim and Dr. Kidane Belay, David Llewellyn for guiding me to develop my skills on sample fabrication. Special thanks goes to Dr. Xinjun Liu for his fruitful discussion, ideas and suggestions on experiments and COMSOL modelling. I would like to sincerely thank to Jack, Kang, Tuan for their friendly cooperation and help.

I appreciate valuable suggestions from Prof. Mark Ridgway, Prof. Chennupati Jagadish, and Prof. Hoe Tan during my graduate years. I thank great helps from ANFF members, especially Dr. Fouad and Dr. Kaushal. Their help was very important to run experimental equipment. I also thank all technical staffs of EME including Joshua and Tom. I want to extend my thanks to administrative staffs Julie Arnold and Karen Nulty for their kind support.

I want to thank Dr. Mohammad Ali Nawaz and Dr. Amdadul Haque Chowdhury for their support during my stay and making Australia comfortable. I will definitely miss the wonderful time with them.

I have to thank my parents for their support and the sacrifices they made, accepting my choice to study in Australia. Finally, I am grateful to my beloved wife for her support and sacrifice during my research.

Publications in Refereed Journals

1. Li S, Liu X, **Nandi S**, Venkatachalam D, Elliman Coupling dynamics of Nb/Nb_2O_5 relaxation oscillators. Nanotechnology 28(12) 125201 (2017).

2. Liu X, Li S, **Nandi S**, Venkatachalam D, Elliman. Threshold switching and electrical self-oscillation in niobium oxide films. Journal of Applied Physics 120, 124102 (2016).

3. **Nandi S**, Liu X, Venkatachalam D, Elliman R, Effect of electrode roughness on electroforming in HfO_2 and defect-induced moderation of electric-field enhancement, Physical Review Applied 4 (6) 064010 (2015)

4. **Nandi S**, Liu X, Venkatachalam D, Elliman R Self-assembly of an NbO_2 interlayer and configurable resistive switching in $Pt/Nb/HfO_2/Pt$ structures, Applied Physics Letters 107, 132901(2015).

5. Li S, Liu X, **Nandi S**, Venkatachalam D, Elliman R High-endurance megahertz electrical self-oscillation in Ti/NbO_x bilayer structures, Applied Physics Letters 106(21), 1-4(2015) .

6. **Nandi S**, Liu X, Venkatachalam D, Elliman R Threshold current reduction for the metal-insulator transition in NbO_{2-x}-selector devices: The effect of ReRAM integration, Journal of Physics D: Applied Physics 48(19), 1-8 (2015).

7. Rosa L, Vos M, **Nandi S** Analysis of multi-layer ERBS spectra, Journal of Electron Spectroscopy and Related Phenomena 202, 26-32, (2015).

8. Liu X, **Nandi S**, Venkatachalam D, Belay K, Song S, Elliman R Reduced threshold current in NbO_2 selector by engineering device structure, IEEE Electron Device Letters 35 (10) 1055-1057, (2014)

9. **Nandi S**, Llewellyn D, Llewellyn D, Belay K, Venkatachalam D, Liu X, Elliman R Effect of microstructure on dielectric breakdown in amorphous HfO_2 Films, Microscopy and Microanalysis 20, 3(2014)

10. Vos M, Grande P, Venkatachalam D, **Nandi S**, Elliman R, Oxygen self-diffusion in HfO_2 studied by electron spectroscopy, Physical Review Letters 112, 175901 (2014).

11. Vos M, Liu X, Grande P, **Nandi S**, Venkatachalam D, Elliman R The use of electron Rutherford backscattering to characterize novel electronic materials as illustrated by a case study of sputter-deposited NbO_x films, Nuclear Instruments and Methods in Physics Research: Section B 340, 58-62 (2014).

12. Grande P, Vos M, Venkatachalam D, **Nandi S**, Elliman R Determination of thickness and composition of high-k dielectrics using high-energy electrons, Applied Physics Letters 103, 071911, (2014).

13. Vos M, Grande P, **Nandi S**, Venkatachalam D, Elliman R A high-energy electron scattering study of the electronic structure and elemental composition of O-implanted Ta films used for the fabrication of memristor devices, Journal of Applied Physics 114, 073508 (2013)

Peer Reviewed Conference Proceedings

1. Li S, Liu X, **Nandi S**, Venkatachalam D, Elliman R Temperature Dependence of Threshold Switching in NbO_x Thin Films 2014 Conference on Optoelectronic and Microelectronic Materials and Devices (COMMAD) 138-140

2. Liu X, **Nandi S**, Venkatachalam D, Li S, Belay K, Elliman R Finite Element Modeling of Resistive Switching in Nb_2O_5-based Memory Device 2014 Conference on Optoelectronic and Microelectronic Materials and Devices (COMMAD) 280-283

3. **Nandi S**, Liu X, Li S, Venkatachalam D, Belay K, Elliman R Resistive Switching Behavior in HfO_2 with Nb as an Oxygen Exchange Layer 2014 Conference on Optoelectronic and Microelectronic Materials and Devices (COMMAD) 290-294

Abstract

Transition metal oxides (TMOs) exhibit characteristic resistance changes when subjected to high electric fields due to the creation, drift and diffusion of defects, and this resistive-switching response is of interest for future non-volatile memory applications. Indeed, resistive random access memories (ReRAM) are considered promising alternatives to conventional charge storage-based devices because of their low production cost, simple fabrication, and excellent scalability. However, the realization of reliable ReRAM devices and their integration in large-scale arrays requires further understanding of the switching mechanisms and the development of new strategies for improving integrated device functionality. The aim of this work is to understand the role of the material structure on device reliability and to investigate the integration of passive selector elements with memory devices for use in memory cross-bar arrays. The thesis begins by investigating the properties of relevant oxide films and then addresses three technologically relevant problems. Specifically these include: 1) understanding how the roughness of metal/dielectric interfaces affects dielectric breakdown and switching behaviour; 2) exploring methods for reducing the operating current of selector and memory/selector devices and 3) investigating the effect of operating conditions on the switching response of devices.

The first of these studies is based on Pt/Ti/HfO_2/Pt devices and combines experimental methods and finite element modelling to understand the effect of the Pt/HfO_2 interface roughness on the electroforming and switching response. Atomic force microscopy (AFM) showed that the roughness of Pt electrodes deposited by electron-beam evaporation increased with film thickness due to facetted grain growth. Results show that roughness leads to a reduction in the electroforming voltage of HfO_2, an increase in the failure rate of devices, and a corresponding reduction in resistive switching reliability. Conventional wisdom suggests that these effects result from local electric field enhancement in the vicinity of electrode asperities. However, the effect on electroforming voltage is much less than estimated from simple geometric considerations. Comparison with finite-element modelled showed high-aspect-ratio asperities can produce field enhancements of more than an order of

magnitude but that the generation and redistribution of defects moderates this effect prior to dielectric breakdown. As a consequence, the effect of field enhancement is less than anticipated from the initial electric-field distribution alone. It is argued that the increase in the device failure rate with increasing electrode roughness derives partly from an increase in the film defect density and effective device area and that these effects contribute to the reduction in breakdown voltage.

The second study showed that the leakage current in NbO_{2-x} selector (1S) elements is shown to be reduced by the properties of an adjacent memory (1M) element when integrated into a hybrid selector-memory device structure. This is shown to result from current confinement in conductive filaments formed in the memory layer. Finite element modelling of the selector-memory structures is used to confirm the observations and to explore material dependencies. The thermal and electrical conductivities of the memory layer are shown to influence the threshold current, but the dominant effect is due to current confinement.

The final study explores the effect of device operating conditions on its operation and identifies an alternative approach for reducing the forming and RESET current in integrated memory/selector devices. This study is based on $Pt/Nb/HfO_2/Pt$ devices which require a very "soft" electroforming process. Such devices are shown to undergo configurable switching controlled by the SET compliance current. When operated at a low compliance-current ($\sim$100 μA), devices show uniform bipolar resistive switching behaviour. As the compliance current is increased ($\sim$500 μA), the switching mode changes to integrated threshold-resistive (1S1M) switching, and at still higher currents ($\sim$1 mA), it changes to symmetric threshold switching (1S) characteristic of threshold switching in $NbO_{2-\delta}$. These switching transitions are shown to be consistent with the development of an $NbO_{2-\delta}$ interlayer at the Nb/HfO_2 interface that is limited by the set compliance current due to its effect on oxygen transport and local Joule heating. The proposed mechanism is supported by finite element modelling of the 1S1M response assuming the presence of such an interlayer. These findings help to understand role of interface reactions in controlling device performance and provide a means for the self-assembly of integrated 1S1M resistive random access memory structures.

Contents

CHAPTER 1

Introduction

1.1. Introduction

Non-volatile memory (NVM) is one of the most essential elements of modern electronics. Since the 1990s, the dominant form of NVM has been floating gate FLASH memory due to its scalability and fast read/write speeds [1]. FLASH memory consists of a transistor with a floating gate, that is a gate insulated by dielectric on all sides, which allows charge to be trapped and stored [Fig. 1.1(a)]. However, FLASH memory approaches scaling limit and introduces complexity for integration of high-density memory application (below 25 nm) [2]. Different types of non-volatile random-access (RAM) memory devices, such as phase change RAM (PCRAM), magnetoresistive RAM, (MRAM), ferroelectric RAM (FeRAM), and resistive RAM (ReRAM), have been actively studied in a last couple of decades to find alternative to FLASH. Among these, resistive random access memory (ReRAM) devices based on non-volatile resistive switching have attracted particular attention due to their scalability, lower power consumption, faster switching speeds, longer retention times, and simpler device structure [3]. ReRAM has a simple metal-insulator-metal (MIM) structure that can be switched between high and low resistance states [Fig. 1.1(b)]. The resistance of the device is controlled by the distribution and redistribution of ions (cation and anion) in response to an applied electric field. Additionally ReRAM can be easily integrated into solid-state circuits, is compatible with complementary-metal-oxide-

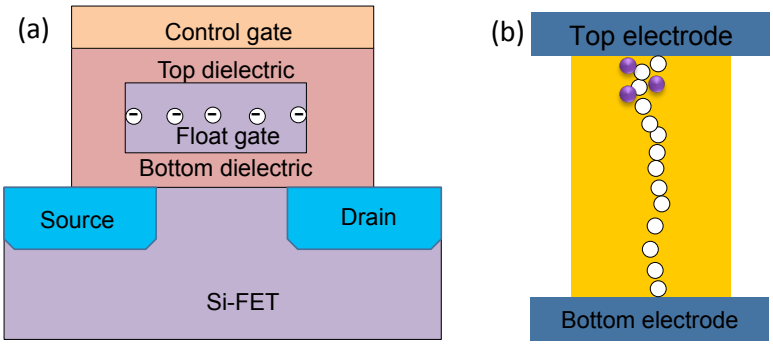

Figure 1.1 Schematic diagram of (a) FLASH and (b) resistive switching device for a single memory cell.

Table 1.1 Comparison FLASH memory with emerging memory technologies.

Type	FLASH	Emerging Memory		
		ReRAM	PCM	MRAM
Cell Size	16 nm	5 nm	45 nm	5 nm
Cell area	$5F^2$	$4F^2$	$4F^2$	$4F^2$
Write/erase time	1 ms/1ms	<1 μs/ $<1\mu$s	1μs/100 ns	10 ns/ 10ns
Endurance	$>10^5$	$>10^{12}$	10^5	10^{14}

semiconductor (CMOS) technology and possesses all the properties required for universal memory. A comparison of emerging memory technologies with FLASH is presented in Table-1.1.

Historically, resistive switching was first reported by Hickmott in MIM stacks with binary oxides as an insulator, such as ZrO_2, Ta_2O_5, SiO_x, Al_2O_3 [4]. In recent years, a large variety of materials, including binary oxides, ternary perovskites, chalcogenides, solid-state electrolytes and organic materials have been shown to exhibit resistive switching effects (Table-1.2) [5]. However, there is particular interest in binary transition metal oxides (TMOs) due to simple structure, thermal stability and their excellent switching characteristics and compatibility with conventional CMOS processes [6, 7]. Resistive switching in these oxides can be classified based on the dominent physical mechanism such as phase transformation, electrostatic, mechanical, chemical and electronic effects. Waser et al [8] have classified redox-based switching mechanism in TMOs into two subclasses: electrochemical metallization mechanism (ECM) and valance change mechanism (VCM). Both types of ReRAM are based on a "filament model" which gives a qualitative explanation for the switching in TMO.

Table 1.2 Types of resistive switching materials

No.	Class of Materials	Materials
1	Binary oxides	NiO [11], CuO [12], CoO_x [13], FeO_x [14], ZnO [15], Gd_2O_3 [16], MnO_x [17], NbO_x [18], HfO_2 [19] WO_x [20], Al_2O_3 [21], TiO_x [22], TaO_x [23], SiO_2 [24]
2	Nitride	AlN [25], NbN [26], NiN [27]
3	Ternary perovskites	$SrTiO_3$ [28] and $SrZrO_3$ [29]
4	Solid-state electrolytes	GeS [30], GeSe [31] Cu_2S [32]
5	Organic materials	rotaxane [33], anthracene [34], tetracene [35], copper tetra(butylphenyl)porphyrin [36], polymethacrylate derivatives, phenylene ethynylenes [37]

In ECM based ReRAM, the MIM structure contains an electrochemically active electrode metal, such as Ag [9] and an electrochemically inert counter electrode, such as Pt, Au, W, etc. In ECM cells highly mobile ions, such as Ag^+ ions drift toward the inert electrode and discharge at the inert electrode leading to a filament formation of Ag dendrites, setting the device into ON-state. When a bias of reverse polarity is applied dendrites dissolve and switch the device into an OFF-state.

Contrary, in TMO based VCM, both electrodes are electrochemically inert and the switching mechanism is triggered by anionic motion, such as oxygen ions, which corresponds to the oxygen vacancies, leading to a local stoichiometry change. The redox reaction is expressed by a valance change of cation sublattice which leads to a change in local conductivity in front of the electrode interface. The filament formation and rupture process of VCM is discussed in detail in the following section.

1.2. Basic Operational Principles of ReRAM

1.2.1. Microscopic Origin of Ionic Migration

As-fabricated ReRAM devices are usually in an insulating state and requires an "electroforming" step to transform the device from its initial insulating state to a low-resistance state (LRS). During a subsequent voltage sweep the device can revert to a high-resistance-state (HRS). This OFF state is non-volatile. Subsequently, while

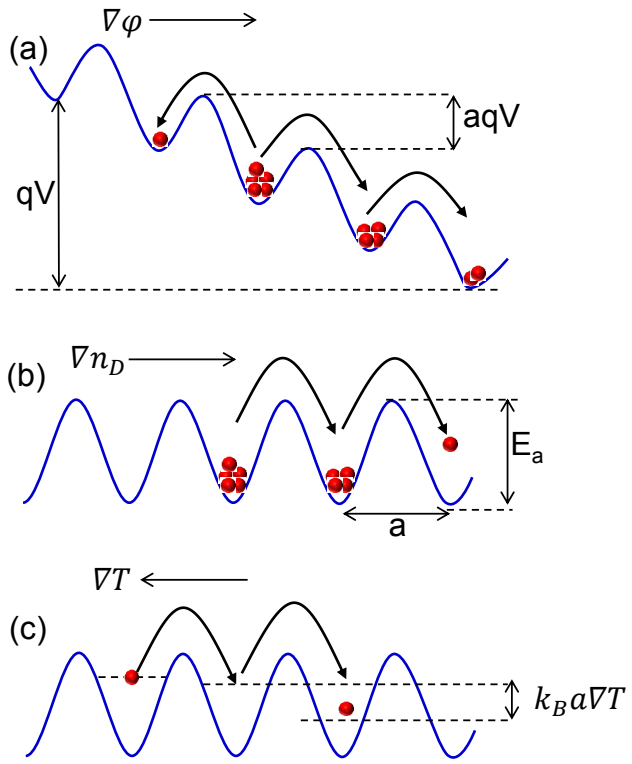

Figure 1.2 Microscopic origin of defect migration (a) electric field (b) Fick diffusion and (c) Soret effect.

sweeping again, the current in the device increases abruptly at SET (from HRS to LRS) voltage (V_{set}) and, the device reverts to a LRS, a non-volatile "ON" state is achieved. It is necessary to enforce a current compliance limit during the forming and SET process to avoid catastrophic breakdown of the device for either switching mode. The bipolar switching mode is polarity dependent.

The resistive switching in VCM has been shown to result from the formation and rupture of a filamentary conduction path formed in the oxide layer by defects. In general, there are three mechanisms working together for ionic motion and rearrangement: electric-field gradient, ionic concentration gradient, and temperature gradient [38].

In the presence of an electric field anions move toward to the cathode whereas cations move toward the anode. Ions migrate in a periodic potential by a hopping process [Fig. 1.2(a)] in the presence of an electric field. The hopping velocity [39] can be expressed as

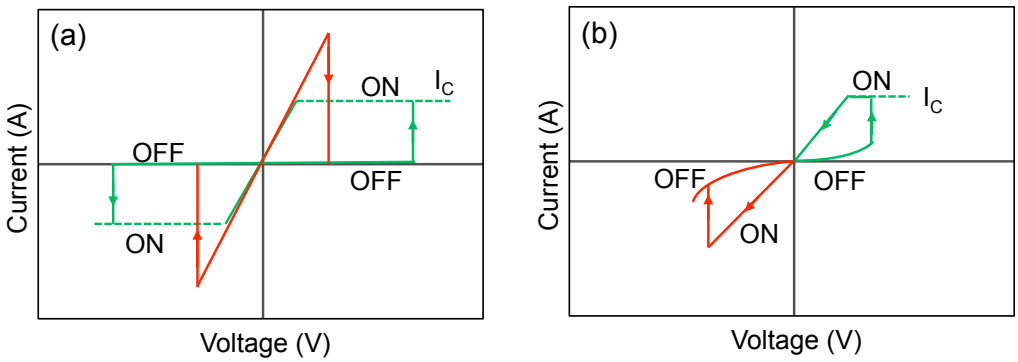

Figure 1.3 I-V characteristics of (a) unipolar switching and (b) bipolar switching.

$$v_{hop} = a\omega exp\left(-\frac{\Delta E_{i,0}}{k_B T}\right) sinh\left(\frac{aq}{2k_B T}E\right) \tag{1.1}$$

where ω (10^{13} Hz) [40] is the attempt rate, $E_{i,0}$ (∼1 eV) is the activation energy for hopping without an electric field and a (∼0.4 nm) is the interatomic distance. The hopping rate at room temperature is approximately one hopping per hour assuming E ∼0.1 V/nm, which is too low to explain resistive switching. Resistive switching has been observed in materials with nanosecond switching time [41]. Therefore, some other mechanisms must contribute to switching.

When a bias is applied across the device, it induces electric current and local Joule heating [42]. Joule heating additionally provides two more ionic motions due to Fick diffusion and Soret effect (thermodiffusion). Joule heating results from the induced high current density in the filamentary conduction path and can increase the local temperature by several hundred degrees, estimates that have been confirmed by direct temperature measurements [42]. At these temperatures, the switching speed is consistent with those observed experimentally. The temperature gradient induces the anisotropic hopping due to Fick diffusion as a result ions move from a high concentration region (hot region) to a lower concentration region (cooler region). This motion due to concentration gradient (∇n_D) is called Fick diffusion, which becomes imperative at high local temperature and hopping rate increases expressively according to Eq. 1.1. Thermodiffusion restores the oxygen vacancy concentration to its original configuration [Fig. 1.2(c)].

Several in-situ observations of these forces by transmission electron microscopy [43–45], scanning transmission X-ray microscopy [46], conducting atomic force microscopy (CAFM) [47, 48], infrared spectroscopy [42, 49] were performed to understand the switching mechanisms associated. These studies confirmed that drift and diffusion are dominant driving mechanism associated with SET and RESET operations. In general, Fick diffusion mechanisms are polarity independent as a result causes a unipolar or non-polar operation of resistive switching. Therefore, the SET and RESET operations can be achieved with same polarity, called unipolar operation as shown in Fig. 1.3(a). In the unipolar case, the RESET voltage is always smaller than the SET voltage ($V_{reset} < V_{set}$) and, RESET current is always higher than set compliance current ($I_{reset} > I_{set}$).

Contrary, the direction of an electric field is polarity dependent and supposed to be the dominating effect in bipolar switching mechanism. The sign of the RESET voltage is opposite to that of SET voltage. For instance, Fig. 1.3(b) shows the bipolar switching where a device goes for a set operation with a positive bias and reset with a negative bias. The switching modes in ReRAM depend on choice of switching materials and electrode materials; fabrication and operating conditions. In the following section we discuss the switching mechanisms further in details.

1.2.2. Electroforming

As-fabricated devices are generally in a high resistance state and require a forming process, analogous to soft dielectric breakdown, to create a filamentary defect path that transforms the device into a low resistance state. Usually, during the forming process the current is limited to protect the device from irreversible electric breakdown. Dielectric breakdown is a complex subject that has been studied in depth for decades, with initial studies dating back to the pioneering work of Frohlich [50]. Both the thermochemical model of McPherson [51,52] and the percolation model of Stathis [53] are widely used to describe electroforming process in TMOs (HfO_2, Ta_2O_5, ZrO_2 etc.). According to thermochemical model of McPherson [51, 52], an applied electric field distorts and weakens metal-oxygen bonds, increasing the probability of defect

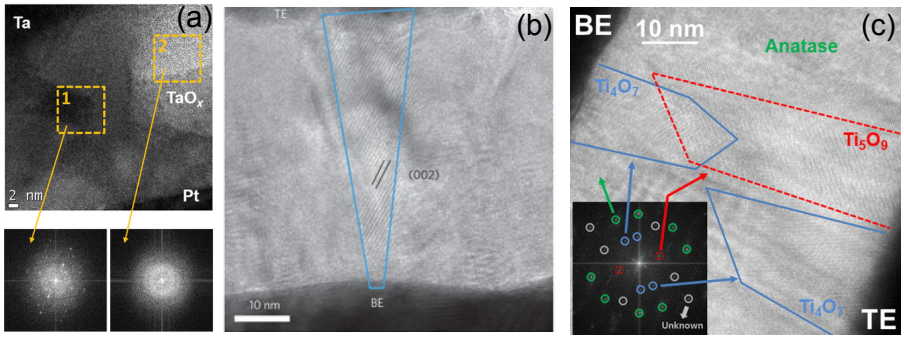

Figure 1.4 High-resolution TEM image of (a) oxygen deficient region in the filament region in Ta_2O_5 (taken from Ref. [55]) (b) a cone-shaped CF of a Magnéli phase (Ti_4O_7) in a TiO_2 matrix (taken from Ref. [43])and (c) an hourglass-shaped CF of two Magnéli phases (Ti_4O_7 and Ti_5O_9) (taken from Ref. [56]).

formation at a given temperature. The activation energy for defect generation is reduced by the presence of electric field and leads to an increase in defect density. The defect generation in the bulk is homogeneous and each vacancy associated with the creation of Frenkel pairs by breaking metal-oxygen (M-O) bonds in the bulk. The activation energy for defect generation in the bulk is higher than that of at the interface or grain boundaries (in polycrystalline oxides). The Frenkel pair generated in the bulk can recombine without activation energy within a timescale of picoseconds [54]. Therefore, in an amorphous oxide film defects are generated heterogeneously at the interface and these defects migrate in the film during forming process. The increase in defect concentration increases the electrical conductivity of the layer that manifests as an increase in leakage current and a concomitant increase in temperature due to Joule heating. This increase in temperature accelerates the generation and migration of defects, providing a positive feedback that leads to dielectric breakdown. Irreversible hard-breakdown is generally prevented by limiting the maximum current in the device. The filament is then comprised of a network of charged oxygen vacancies (V_O^{2+}) and has a resistance that is sensitive to the vacancy distribution. Therefore, the filament is formed by the local microstructural and stoichiometric changes due to generation/migration of oxygen vacancies and confirmed by several experimental observations as shown in Fig. 1.4.

1.3. Switching Mechanism

1.3.1. Unipolar Switching

During the SET process drift dominates, then charged vacancies move toward the cathode and an asymmetric filament forms as shown in Fig. 1.5(a). The unipolar RESET process is dominated by the thermal mechanism. The high-density current flows through the conducting filament, disrupting the filament due to a dissolution mechanism of defects or due to a local thermal-induced oxidation [Fig. 1.5(b)]. The vacancy distribution in the filamentary region is considered to be highly non-uniform and vacancies diffuse from high concentration regions to low concentration regions to minimise the Gibbs free energy [Fig. 1.2(b)]. As a result a gap opens in the conducting filament. The conducting filament would disrupt where temperature is highest, and most probably the switching spot is in the bulk of the switching material. In thermochemical memory (TCM) thermochemical processes dominate over the electrochemical process [10]; and the change in resistance in a memory device occurs due to thermally induced stoichiometry and redox reactions. Due to thermal nature of RESET process, this type of switching is inherently unipolar.

The filamentary nature of switching is evident from its temperature, thickness and area dependencies. The SET/RESET voltage is independent of the thickness of the switching matrix indicating the formation/rupture of the conducting filament is localized [57, 58]. The resistance of the LRS weakly depends on the device area, which confirms the filamentary switching. However, the resistance of the HRS shows both area dependent and independent nature. Area dependence of the HRS indicates that during the RESET process the conducting filament is ruptured completely [8] whereas area independence indicates the filament is partially dissolved as a result of localized current flow [59]. Therefore, the nature of the RESET process determines area dependence of the HRS and a similar dependency is obsered as a function of temperature [8]. However, the conductance of LRS decreases slightly with temperature indicating metallic state of LRS [8].

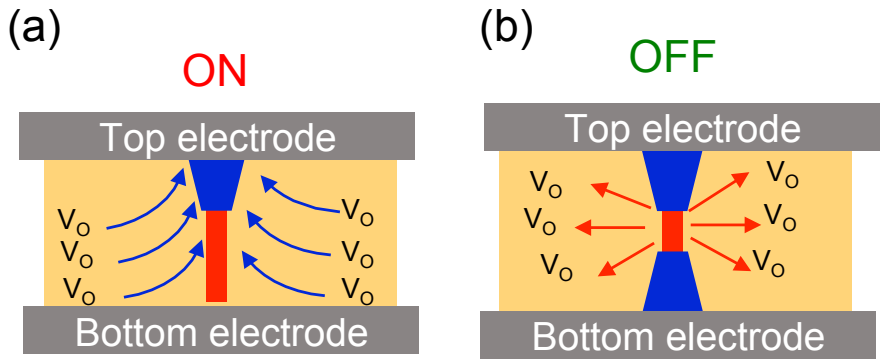

Figure 1.5 Unipolar switching mechanisms: (a) SET and (b) RESET.

1.3.2. Bipolar Switching

In the case of bipolar switching the growth and dissolution of the conducting filament is dominated by the applied electric field as shown in Fig. 1.6. The SET process is similar to the forming process or a unipolar SET process; V_O^{2+} vacancies drift towards the cathode in response to the applied electric field and form a conducting filament between electrodes [Fig. 1.6(a)]. The SET voltage is smaller than the forming voltage as as only the partial broken filament needs to be reconstructed. When the polarity of the applied voltage is reversed, oxygen ions and vacancies drift back towards each other and annihilate, opening a gap in the conductive filament [Fig. 1.6(b)]. The bipolar switching behavior is then induced by connecting and rupturing the conducting filament. The gradual bipolar RESET behavior suggests a gradual rupture of the filament, due to the reverse migration of ions/vacancies during reset process, which arupture the conducting filament.

Experimental observations of Zhou et al confirmed that an interfacial suboxide layer acts as oxygen reservoir and is responsible for bipolar switching [60]. Therefore, the use of a sub-stoichiometric oxide generally leads to improved device performance, reliability and endurance. One common approach is to use a reactive metal (oxygen exchange layer) in contact with the oxide [61]. Oxygen vacancies are formed by chemical reaction between the oxide and oxygen-scavenging metal cap, then control the switching behavior and may influence filament formation and provide a means of improving device reliability [62]. The use of substoichiometric oxides mitigates the

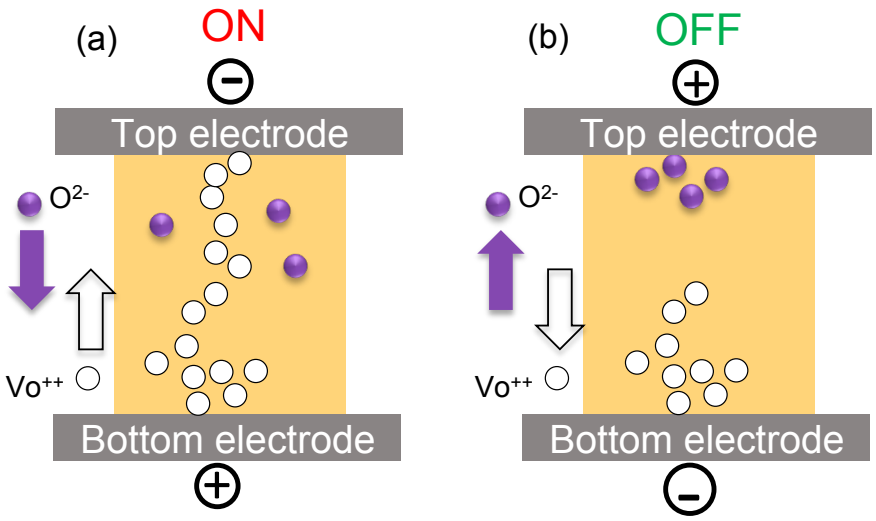

Figure 1.6 Schematic representation of bipolar switching mechanism: (a) SET process and (b) RESET process.

need for defect generation (V_O^{2+}) is determined by the film composition and generally leads to improved device performance, reliability and endurance. This is obtained by using a reactive metal (oxygen exchange layer such as Al, Ta, Hf, Ti) in contact with the oxide [62, 63] or by deliberately forming an oxygen deficient layer (such as TaO_x, HfO_x). The growth of such a layer is confirmed by both simulation [64] and in situ TEM [65]. The oxygen deficient layer acts as a series resistor and the resistance is comparable to the LRS of the resistive switching layer. This series resistance efficiently prevents the adverse effects of the current (voltage) overshoot during the conducting filament formation and rupture [66]. However, the coexistence of the two switching modes operating in opposite polarities is common in the same device [67]. This is due to formation of two different switchable layers adjacent to the interfaces at the top and bottom electrodes during the electroforming process. This type of switching is discussed in detail in Ref. [67].

1.4. Threshold Switching in TMOs

Threshold switching is a volatile resistive switching phenomena with characteristics as shown in Fig. 1.7(a). Under voltage controlled operation the device switches from an insulating state (OFF) to a conducting state (ON) and turns back to the OFF -state when the bias is removed. The I-V characteristics show hysteresis with

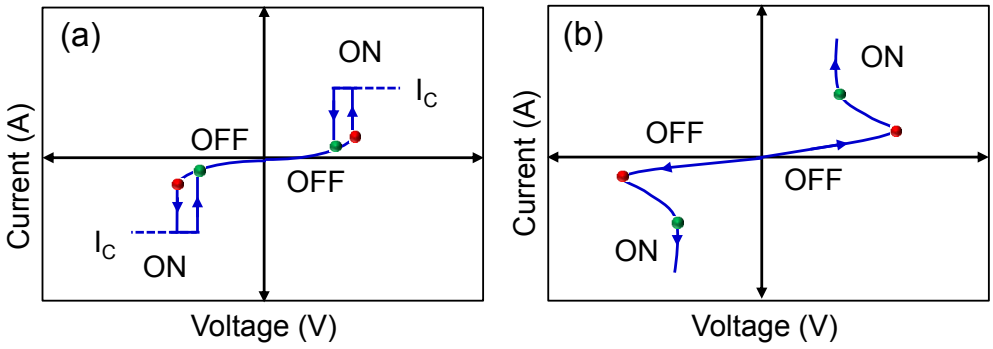

Figure 1.7 (a) Voltage controlled current-voltage characteristics of threshold switching. (b) Current controlled I-V characteristics shows a negative deferential resistance region.

switching to the ON state occurring at a "threshold voltage", and switching back to the OFF-state occurring at lower "hold voltage", as shown in Fig. 1.7(a). Under current controlled operation the device exhibits negative differential resistance (NDR) as shown in Fig. 1.7(b).

Threshold switching has been observed in a wide range of transition metal oxides (e.g. VO_2, Ti_2O_3, NbO_2, Fe_3O_4) [62, 63, 68, 69], with particularly impressive results reported for VO_{5-x} [70, 71] and NbO_{5-x} [72, 73] suboxides. A threshold switching device also requires an electroforming process. In contrast to the thermochemical model of the electroforming process, the switchable filament in these oxides is induced by a phase transition from higher oxides to less resistive oxides (e.g. VO_2, NbO_2) [69].

Several mechanism have been proposed to explain threshold switching but the dominant process is still under debate. In this work, we have adopted a model based on a Joule-heating induced insulator-metal-tansition (IMT) where localized heating in a filament converts the filament from an insulating state to a metallic state, giving an abrupt change in current. VO_2 is one of the best studied materials and is widely exploited [74]. It undergoes a thermally-induced Mott-Peierls transition at a temperature of 340 K [75] [Fig. 1.8]. Below this transition temperature, the lattice is monoclinic and the conduction electrons are localized to the paired vanadium atoms [Fig. 1.8(a)]. At the transition temperature, the large vibrational amplitude stabilizes the VO_2 into a tetragonal structure, where electrons are free to move throughout the lattice [Fig. 1.8(b)]. When current/bias increases up to a threshold

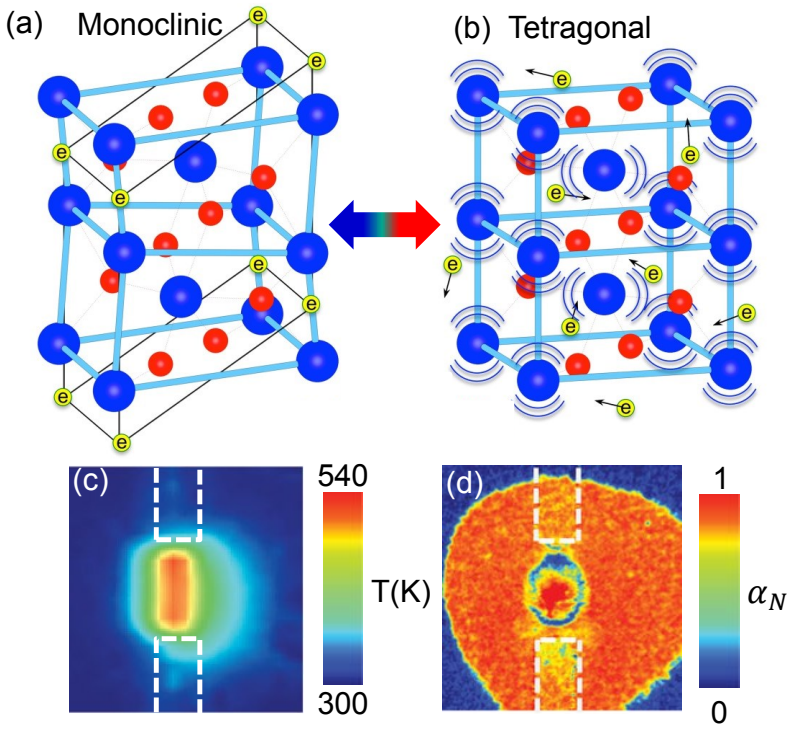

Figure 1.8 (a) Monoclinic structure of VO_2 in its insulating phase, where vanadium atoms (blue) paired with oxygen (red), with dimers are bound by electrons. (b) Conducting phase of VO_2, large vibrational motions stabilize the tetragonal phase and free up conduction electrons. (taken from Ref. [77]) (c) Blackbody spectro-microscopy and (d) scanning transmission X-ray microscopy of planar VO_2 device (taken from Ref. [49]).

value the device resistance increases over several orders of magnitude and turns "ON" due to an IMT transition, while being insulating at lower voltages. The IMT transition of VO_2 in a planar device is confirmed by direct observation by blackbody spectro-microscopy and scanning transmission X-ray microscopy (STXM) as shown in Fig. 1.8(c-d) [49]. The IMT in NbO_2 is believed to result from a similar thermally induced Mott-Peierls transition in which the NbO_2 lattice undergoes a structural transition from a distorted (insulating) rutile structure to an undistorted (metallic) rutile structure at high temperatures [76].

1.5. Current Issues of Resistive Switching

Even though excellent switching characteristics have been observed experimentally in TMO based resistive switching devices, the current challenges for ReRAM technology are uniformity and reliability. Microstructure of switching and electrode materials

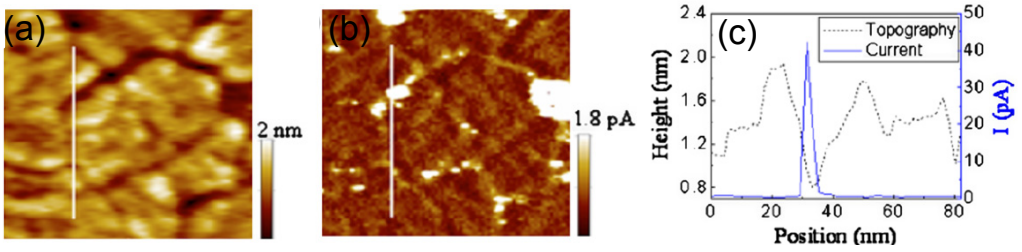

Figure 1.9 (a) Surface topography and (b) current map of polycrystalline HfO_2. The tip was biased at 6.5 V and the image has a dimension of 168×168 nm. (c) Topography and current along line drawn in (a) and (b) (taken from Ref. [78]).

can influence both reliability and uniformity. The integration of ReRAM high density memory array requires an integrated selector-memory structure. These issues will be discussed in the following sections.

1.5.1. Microstructure Effect on ReRAM Reliability

1.5.1.1. Effect of Grain Boundaries

The resistive switching mechanism is controlled by electrode and oxide materials, and the microstructure of the oxide layer can affect the electrical properties of the MIM structure. Several studies [79–81] have been conducted to understand the mechanism of dielectric breakdown in polycrystalline and amorphous films. From first principle calculations, it has been demonstrated that positive and neutral vacancies segregate to grain boundaries and can trap electrons [80, 82]. The current through the crystalline matrix then preferentially flows along the highly conductive grain boundaries and breakdown occurs preferentially at the grain boundaries [79, 80, 83]. Therefore, a larger leakage current is expected in polycrystalline oxides compared to amorphous oxides. Indeed, highly conducting grain boundaries are observed in polycrystalline HfO_2 by conducting atomic force microscopy measurements as depicted in Fig. 1.9 [78]. Apart from the breakdown phenomenon, the microstructure of the switching matrix can also affect the performances of the resistive switching memory.

As grain boundaries are more conductive than bulk, it is expected that the current parallel to the switchable filament in a polycrystalline film will be higher than that

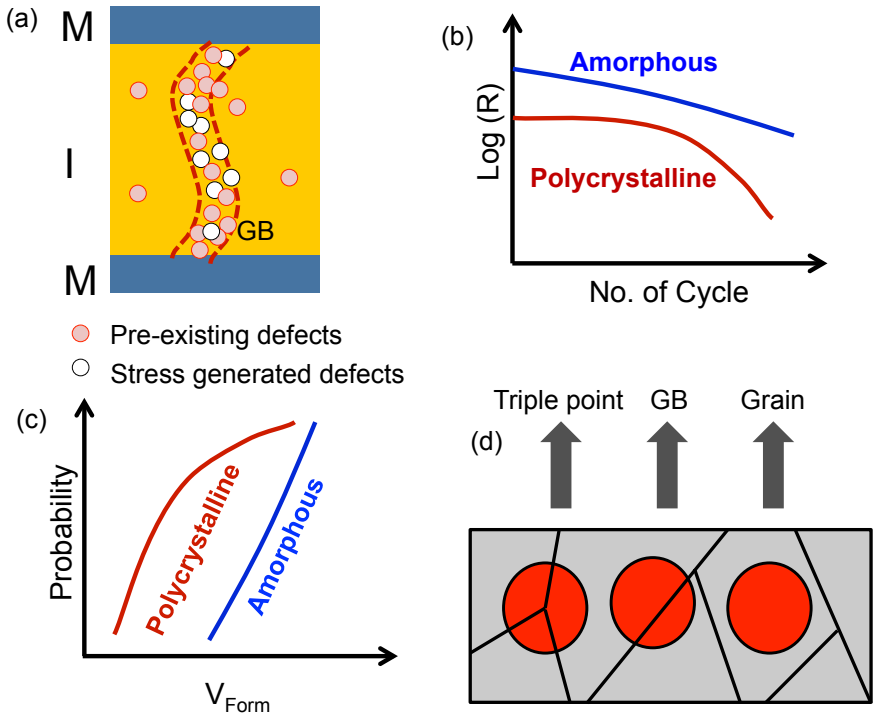

Figure 1.10 Schematic representation of (a) a filament and bulk of a polycrystalline based MIM structure; (b) variation of resistance with switching cycles, (c) variation of forming voltage in amorphous and polycrystalline films, and (d) grain boundary per device in a polycrystalline switching material, when device size is comparable with grain size. The red circles are devices and black lines represent grain boundaries (redrawn from Ref. [84]).

in the amorphous film [Fig. 1.10(a)]. This is because of the higher relative portion of the active area to the non-active area in a crystalline film [85]. This implies that, with switching cycles, the filament is likely to widen laterally, which deprives low power operation and reduces the memory window [Fig. 1.10(c)]. Grain boundaries also affect forming and set/reset resistance and voltage distributions in amorphous and polycrystalline film [Fig. 1.10(c)] [86, 87]. Controlling the grain size distribution is another challenge. For example, an extreme is being a situation where one device spans a grain boundary while second one has two or none [Fig. 1.10(d)]. As a result, aggressively downscaled devices could have very severe variability in switching parameters if based on polycrystalline films.

1.5.1.2. Effect of Interface Roughness

Theoretical and experimental studies [88] have shown that the electrical performance of capacitor like structures is affected by surface roughness. This can be a dominant

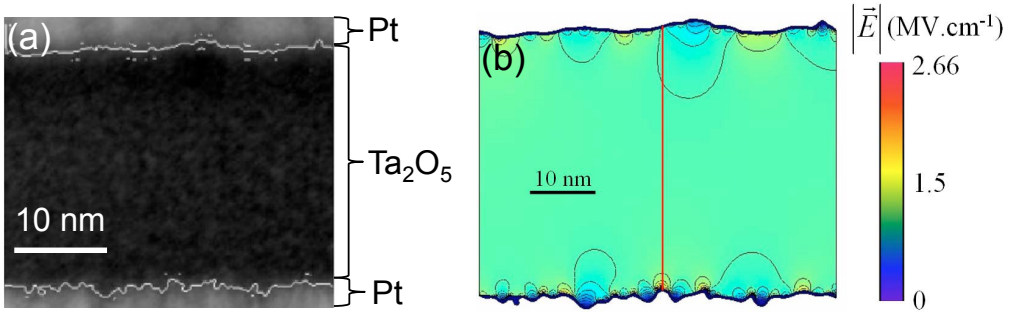

Figure 1.11 (a) A TEM micrograph of MIM capacitor with interface profile superimposition on original TEM picture. (b) In situ electric field distribution in the in dielectric layer MIM capacitor, which shows that the electric field is maximum at the top of the asperity along the red line (taken from Ref. [90]).

effect when the roughness is comparable with the thickness of the dielectric layer. Asperities at the interface increase the electric field and result in premature dielectric breakdown at the weak point locations. However, in reality the electric field distribution will be inhomogeneous and will show significant enhancement in the vicinity of electrode asperities [89]. The electric field amplification at the top of the vicinity of the asperity is called lightning-rod electric field amplification. Gaillard et al [90] showed that the electric field enhancement at the interface is responsible for asymmetric current-voltage characteristics of the MIM structure [Fig. 1.11(b)].

According to the electrochemical model [51, 52] of dielectric breakdown vacancies are produced by a field-enhanced activation process and thereby reduce the activation energy for bond-breaking. Dielectric breakdown voltage distribution is therefore expected to spread significantly due to rougher interfaces. In addition, studies show that the variation in operating voltage/current is affected by the electrode roughening [86, 91].

1.5.1.3. Sneak Current Issue in ReRAM

A crossbar is a set of closely spaced parallel electrode lines running at right angles to each other where switching material is sandwiched at each crosspoint as shown in Fig. 1.12(a). Information at each crosspoint is stored as a HRS or LRS of the device. If F is the width of each line and spacing between two lines, then the area of each cell

is $4F^2$. By stacking n crossbars on each other, the memory density can be further increased to $4F^2/n$, where each cell can be operated without influencing each other. Due to its simple structure this concept is used for high-density memory integration without any transistor. However, the realization of these simple architectures is hindered by an inherent problem called sneak currents [92]. This arises from the fact that a nearby unselected memory cell passes current in either direction when it is in "ON" (low resistance) state and can thereby introduce unintended addressing of memory elements via indirect addressing routes, as shown in Fig. 1.12(a). This also results in data reading errors. Sneak current paths limit the size of crossbar arrays and increase the energy consumption of the memory devices. To avoid the general problem of sneak paths a selection device such as a diode (1D1R structure), a transistor (1T1R structure), or a selector (1S1M structure) is required in combination with the memory element, as shown in Fig. 1.12(b). A diode is used for unipolar memory devices that operate with a single polarity write/erase voltage [93] . In this case, the diode allows current to pass through a memory element under one polarity of applied voltage and reduce the current that flows under the reverse polarity. But a bipolar device uses both polarities to write/erase voltages and generally requires a more complicated device, such as a transistor [94]. However, the incorporation of transistors into a crossbar memory array adds significant complexity to the device structure. As a consequence, there is enormous interest in developing passive selector elements capable of operating with bipolar memory devices. A bidirectional threshold switch is a potential candidate for the selector element for bipolar switching. Indeed, integrated hybrid 1S1M (Selector + Memory) devices have been fabricated using simple bilayer material structures [95, 96]. It is possible to select the particular memory device by applying bias of opposite polarity to the word and bit line. In this case only the selected cell will have bias above the threshold voltage and can be turned ON while others remain OFF. The most important advantages of 1S1M structure are highly scalable and stackable, which is essential for high memory density.

For example, hybrid 1S1M devices based on Pt(W)/Nb_2O_{5-x}/NbO_{2-x}/Pt have been shown to meet many of the requirements for next generation nonvolatile memory arrays [97]. In this case the NbO_{2-x} layer exhibited volatile threshold switching

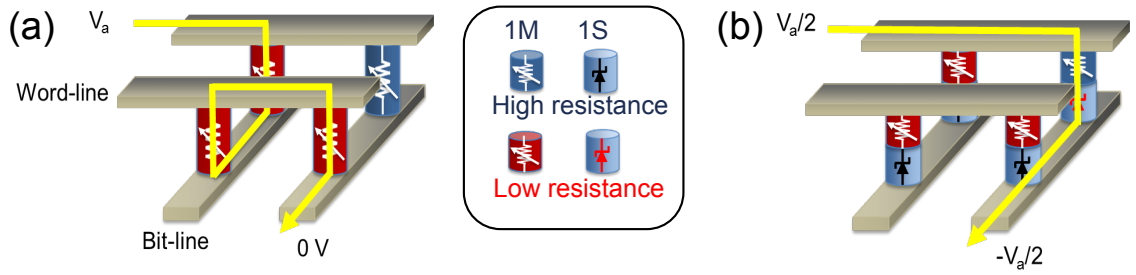

Figure 1.12 (a) A 2×2 crossbar memory array, where during data reading current leakage through sneak current paths introduces addressing errors. (b) The use of hybrid selector-memory structures to overcome the sneak path problem.

and acted as the selector element; and the Nb_2O_{5-x} layer exhibited non-volatile resistive switching acted as the memory element. The suboxide, NbO_{2-x}, is of particular interest as a selector device due to high temperature stability than VO_2 and reasonable resistance ratio ($>10^2$ in practice). NbO_x based selector elements require relatively high operating currents (1-100 mA) compared to resistive-switching memory (1-100μA) devices [18, 98]. The OFF-state leakage current of the selector element is required to be as low as possible (ideally several orders lower than ON-state current). The turn ON/OFF voltage of the selector should be compatible with the memory element with which it is paired. For example, if the selector ON bias is much smaller than the memory element, applied $V_{read}/2$ will degrade effective selectivity.

1.6. Aim of Thesis Work

This dissertation aims to understand the effect of electrode roughness on ReRAM reliability and develop integrated selector-memory (1S1M) devices for crossbar application. These issues are discussed in brief below:

- Several studies [88–90] showed that the interface roughness induces electric-field enhancement. However, the role electric field enhancement in electroforming process in not clearly understood. In this dissertation, I will address this by correlating electrode roughness with the breakdown/switching characteristics of amorphous HfO_2. In addition, a physics-based forming model will be developed

to understand the role of field enhancement on field-induced defect generation.

- Reduction of leakage current in 1S1M device structures is extremely important for high density memory. In the present work, I have explored a strategy based on reducing the active volume of the threshold switching material and maximising the local temperature rise for a given electric stress. This is achieved by controlling the filament size in the memory layer and confining the electric-field and/or current in a specific region in order to reach the IMT with a lower current. Finite element models also will be developed by combining threshold and memory switching for to understand physics of different 1S1M systems.

- 1S1M device structures typically require high forming currents to initiate the selector response, and because the memory elements are necessarily subjected to the same current they are typically formed in a low resistance state. As a consequence, the memory element initially requires large operating currents and exhibits unipolar operation (thermally driven) with large on/off resistance ratios. This does not preclude subsequent bipolar operation, but it can directly affect device uniformity and reliability. Finally, the goal is to develop low power 1S1M devices with a self-ensemble NbO_{2-x} layer.

1.7. Thesis Outline

This dissertation is organized in 7 chapters. Chapter 2 covers a brief description of experimental techniques for characterizing films used for ReRAM devices, and the electrical measurement system. Chapter 3 highlights the role of stoichiometry and electronic structure of HfO_2 and NbO_x films. Chapter 4 demonstrates the effect of bottom electrode roughness on electroforming and switching properties. In addition simulation results are presented to explain electric-field moderation by defects. Chapter 5 shows the effect of electric field confinement on leakage current in homogeneous and heterogeneous 1S1M structures. In Chapter 6, I show the effect of compliance current on switching modes in $Pt/Nb/HfO_2/Pt$ device structure. Finally, in Chapter 7 I have drawn a conclusion based on experimental and simulation results.

CHAPTER 2

Experimental Techniques

2.1. Introduction

This chapter provides a brief overview of the sample preparation techniques and major characterisation tools used in this research. Specific experimental details are contained in the relevant chapters. Atomic layer deposition and RF sputtering were used to deposit oxide thin films. The major analytical tools to characterise thin film quality, stoichiometry and thickness are Rutherford Back-scattering Spectroscopy (RBS), Electron Rutherford Back-scattering Spectroscopy (ERBS), Atomic Force Microscopy (AFM), Transmission Electron Microscopy (TEM) and x-ray Diffraction (XRD). Some high resolution TEM analysis was done externally (Nanolab [99]) and all other experiments were done with equipment available in the department. The current-voltage characteristics of resistive switching devices were measured using a parametric analyser.

2.2. Device Structure Fabrication

Metal-insulator-metal (MIM) structures were fabricated on thermally oxidized (100) silicon wafers with an oxide thickness of 300 nm Fig. 2.1(a). The bottom electrodes comprised a 10 nm Ti wetting layer and a Pt layer with a thickness in the range

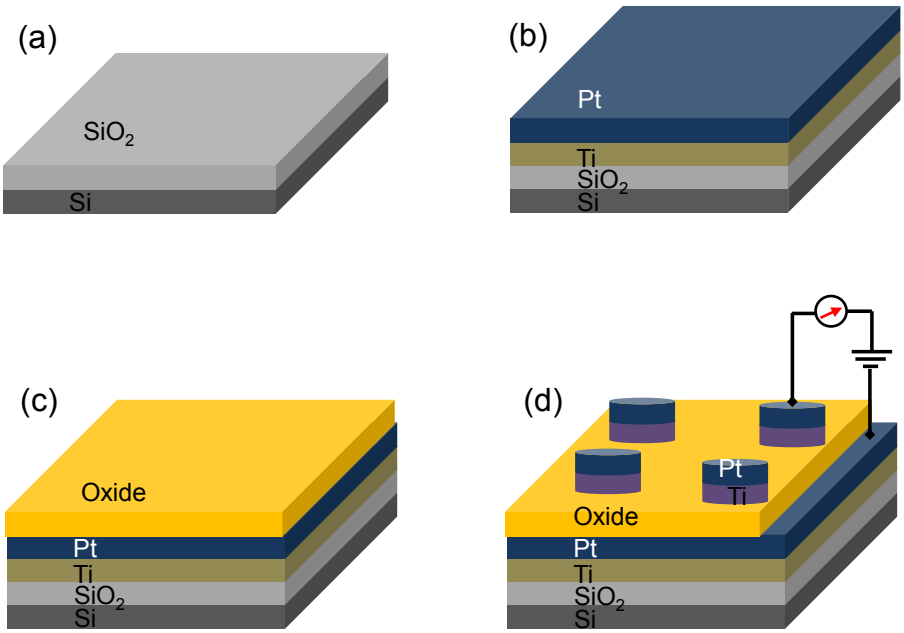

Figure 2.1 Schematic device fabrication process: (a) oxidized silicon wafer, (b) Pt layer deposited with Ti wetting layer, (c) oxide layer deposited by either ALD or sputter deposition and (d) finally top electrode deposited through a shadow mask.

from 25-150 nm [2.1(b)]. These films were deposited by electron beam evaporation without breaking vacuum and were deposited at an average rate of 2 Å/s for both Ti and Pt. The bottom electrodes were deposited on a 4 inch wafer and then cleaved into pieces (typically, 1×1 square inch). Then oxide layers were deposited on a piece of Pt, and a part of it was masked during sputtered deposition to access the bottom electrode. For the ALD films, one edge was etched for the same reason. For a bilayer integrated selector-memory ReRAM both selector and memory layers were deposited without an intermediate electrode. Finally, top electrodes (∼50-70 nm) of 100-250 μm diameter were deposited through a shadow mask by electron-beam evaporation or sputter deposition technique to complete the asymmetric MIM test structures.

2.3. Thin film Deposition

2.3.1. Atomic Layer Deposition

Atomic layer deposition (ALD) is based on self-limiting absorption of reactant species to grow thin films. In the present case HfO_2 layers were deposited using a

Cambridge Nanotechnology Savannah ALD system [100]. The ALD system uses tetrakis-(dymethylamido)-hafnium ($Hf(NMe_2)_4$) as the source Hf and HfO_2 vapour as the oxidant with an N_2 purge between pulses. Deposition was performed at 200° C and the growth rate was ∼1 Å/cycle at this temperature.

2.3.2. Sputter Deposition

NbO_x films were prepared by DC-magnetron sputtering from a Nb (99.999 %) metal target using a commercial deposition system (ACT 2400 UHV) [101]. The stoichiometry of the NbO_x films was controlled by varying the partial pressure of oxygen (P_{O_2}: from 0 to 40 %). The Nb metal was also deposited from same target. The sputtering atmosphere was maintained at a pressure of 4 mT during deposition, and the discharge power was maintained at 300 W. All depositions were performed with the substrate held at room temperature.

2.3.3. Electron Beam Deposition

Pt, Ti and Nb layers were deposited by electron-beam (e-beam) evaporation using a commercial deposition system (Temscal BJD-1800) [102]. In the e-beam process, a focused high-energy electron beam is generated from an electron gun that is directed to the target metal to melt and evaporate it from a crucible. The substrate temperature during deposition ranged from room temperature to 60° C. The deposition rate was 2 Å/s with a base pressure of 10^{-6} Torr and working pressure of $\sim 10^{-5}$ Torr.

2.4. Thin film Characterization

2.4.1. Surface Morphology

The surface topography of bottom electrodes and oxide layers was measured in tapping mode using a Digital Instruments Multimode Nanoscope III atomic force microscopy (AFM). Tapping mode eliminates shear forces and prevents the surface damage by intermittently contacting the sample surface. The root-mean-square

(RMS) roughness and height distribution were calculated for different scan areas in the range of 0.25-25 μm^2 using a modular program for scanning probe microscopy called Gwyddion [103].

2.4.2. Crystallinity of Thin Films

The crystallinity of deposited thin films was measured by Grazing Incidence Angle X-ray Diffractions (GIAXRD) using conventional $\theta/2\theta$ scanning methods with a fixed grazing angle of incidence. The fixed angle was chosen to be 0.5^o to minimize reflection from the substrate. Samples were scaned from 20 to 70^o. The diffraction spectra were measured using a Panalytical X'pert Pro^{TM} [104] system with CuKα radiation at 1.545 Å. Obtained spectra were analyzed by X'pert HighScore software [105].

2.4.3. Stoichiometry and Electronic Structure Analysis

The stoichiometries and compositions of oxides were measured using Rutherford Back-scattering Spectroscopy (RBS) and Electron Rutherford back-scattering Spectroscopy (ERBS). The RBS analysis was performed with 2 MeV He^{2+} ions whereas ERBS uses a monoenergetic electron beam. RBS is widely used in determining the composition of thin films and details can be found elsewhere [106]. Here, the ERBS technique is discussed briefly.

The experimental set up of the ERBS technique is shown in Fig. 2.2. A highly mono-energetic electron beam and a high resolving power electron energy analyzer are used. The spectrometer has two electron beam guns (A and B); each has barium oxide as a cathode. Barium oxide is used as it has low work function and thermal energy spread at low temperature. The scattering angles for gun A and B are 120^o and 45^o, respectively, as shown in the lower panel of Fig. 2.2. The sample holder is surrounded by a hemisphere of metal, which is kept at a high potential (20-40 keV). The electron analyser is kept at an angle of 135^o with respect to the incident beam.

Especially for energies (E_0) greater than 20 keV, the recoil of an electron scattering elastically over large angles from an atom is such that it transfers a measurable

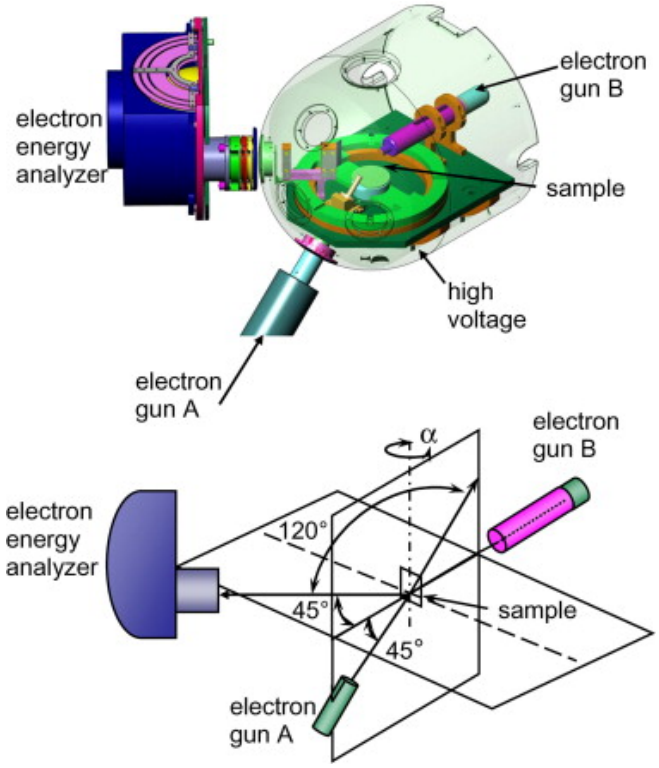

Figure 2.2 Experimental setup of the electron Rutherford back scattering. The upper part illustrates different parts of the spectrometer. The lower part demonstrates the geometry of the electron scattering. The sample orientation is $\alpha = 0^o$ and $\alpha = 125^o$ with respect the gun A and B respectively.

amount of energy to this atom; an energy that depends on the atomic mass (M_i). The elastic scattering peak therefore has different components, each corresponding to scattering from an atom with a specific mass. For instance, for electrons scattered from HfO_2, the elastic peak has two components, one corresponding to the scattering from Hf atoms and another from O. The intensity of each peak depends on the Hf and O concentrations and scattering cross-sections but also on the inelastic mean free path (IMFP) of the medium. As the IMFP can be considered equal for electrons scattered from different elements, the stoichiometry of the outermost layer can be generally be determined from the ratio of elastic peak area and scattering cross sections.

Both inelastically and elastically scattered electrons can be measured in (Reflection) electron energy loss spectroscopy ((R) EELS) experimental setup. A REELS probe can be used to measure the band structure of a semiconductor or insulator. At band

gap, energy loss is the minimum and the onset of the energy loss spectrum is thus a signature of the band gap in the near surface area of the sample.

2.5. Shadow Masks

Shadow masks were used to pattern top electrodes. The benefits of this approach are that it is a simple process which avoids contamination with organics at the sample interface from photoresists. For this work the shadow mask had three parts: 1) base plate, 2) mask and 3) fastening frame as shown in 2.3.The base plate holds nine samples at a time. The mask is fixed by fastening it with a frame with screws. The mask has holes with diameters varying from 100-250 μm.

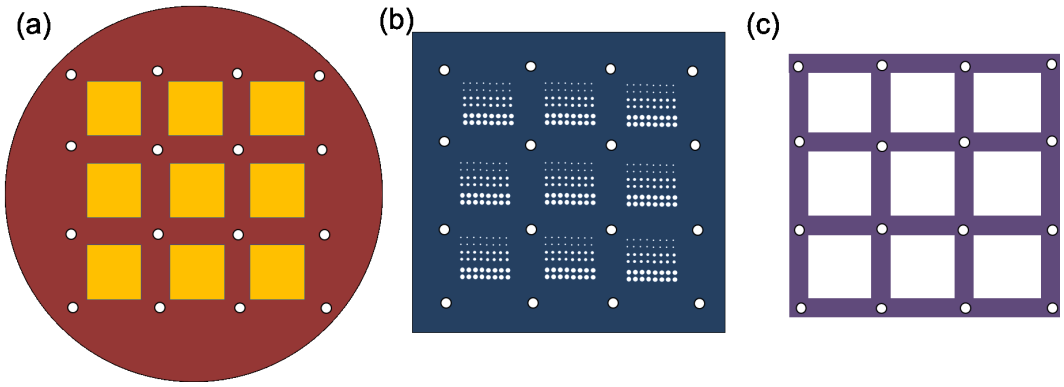

Figure 2.3 Schematic of the shadow mask used in this work, (a) shadow mask holder, (b) shadow mask and (d) fastening frame for samples.

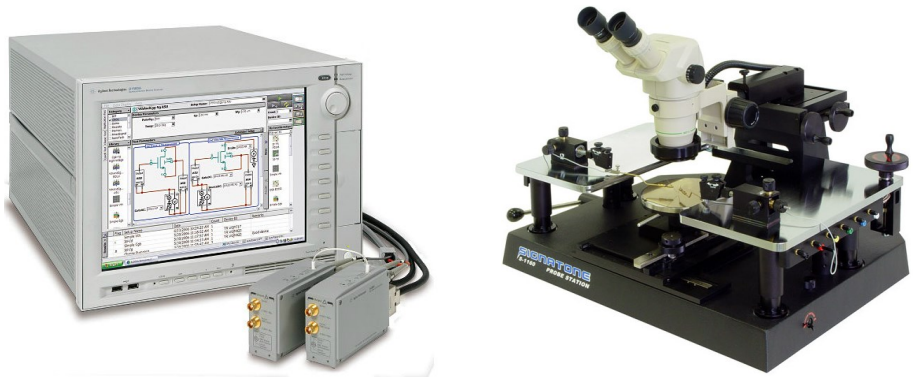

Figure 2.4 (a) The Agilent B1500A parameter analyser system and (b) Signatone 1160B probe station with hot chuck.

2.6. Electrical Measurement Systems

Electrical measurements of ReRAM devices were performed using an Agilent B1500A AC/DC parameter analyser (Fig. 2.4) [107]. This system supports current-voltage (IV), capacitance-voltage (CV), and pulse/dynamic measurements. The B-1500A was connected to a S-1160 probe station [108], which was equipped with four probes (5 μm W) attached to X-Y-Z manipulators.

CHAPTER 3

Stoichiometric and Electronic Structure Analysis

3.1. Introduction

Resistive switching in metal-insulator-metal (MIM) structures is controlled by the composition and electronic structure of the switching layer [109]. Therefore, characterizing these properties is a mandatory step in their development [110, 111]. There is a wide range of techniques used for electronic and stoichiometric analysis. For example, X-ray photoemission spectroscopy is most commonly used for ultra thin layers and ion scattering Rutherford backscattering spectroscopy (RBS) or medium energy ion scattering (MEIS) are often used for thicker layers [112]. In this chapter, we study the electronic properties and stoichiometries of ALD grown HfO_2 and plasma sputtered NbO_x films using a technique called electron Rutherford back scattering (ERBS) spectroscopy (briefly discussed in Chapter 2). In short it is based on the analysis of elastic and inelastic scattering high-energy electrons backscattered from the sample. For electron energies greater than 20 keV, energy lost in elastic collision is sufficient to distinguish scattering from different atoms. The energy spectrum can therefore be used to analyse stoichiometry and thickness of the overlays. Scattering electrons that undergo additional energy loss can also be detected and provide information about the electronic structure of materials (e.g. bandgap). This corresponds to reflection

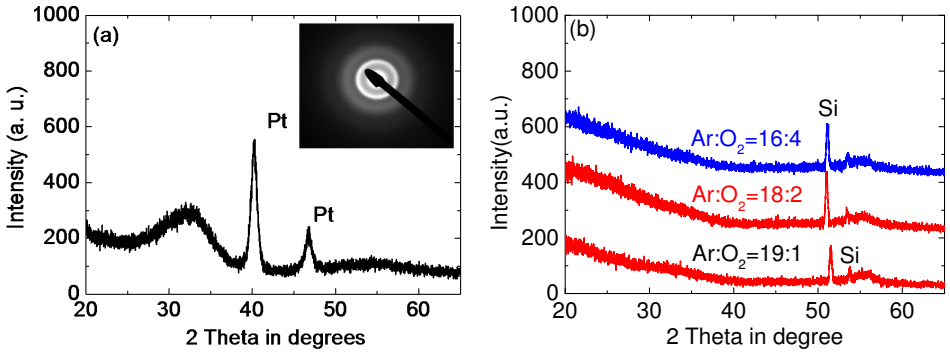

Figure 3.1 GIAXRD spectra of (a) a 20 nm as-deposited HfO_2 layer on Pt film and the inset shows diffraction pattern from transmission electron measurement, and (b) NbO_x as function of $Ar : O_2$ partial pressure.

electron energy loss spectroscopy (REELS) [113]. In this way, we obtain a fairly detailed picture of the elemental composition and electronic properties of HfO_2 and NbO_x films, which is utilized to chose proper oxides for device fabrication.

3.2. Sample Preparation

Two series of samples (HfO_2, NbO_x) were prepared for stoichiometric and electronic structure measurements. The HfO_2 series of films were fabricated on thermally oxidized (300 nm SiO_2) silicon wafers (100 mm p-type, (100) oriented) using an atomic-layer deposition (ALD) system. Films of 2-40 nm thickness were deposited using a Cambridge NanoTech Savannah ALD system. Substrates were held at 200^o during deposition and the HfO_2 layer was grown using alternating pulses of pure tetrakis-(dimethylamido)-hafnium ($Hf(NMe_2)_4$) and H_2O vapor, with an N_2 purge of the reaction chamber between pulses. After deposition the wafers were diced into 1×1 cm square samples. A grazing incidence-angle X-ray diffractions (GIAXRD) spectrum of an as-deposited film is shown in Fig. 3.1(a), and exhibits a broad peak centered at 2Θ value of 32^o, consistent with the amorphous structure of HfO_2. That is, no diffraction peak for crystalline HfO_2 is observed in the as-deposited HfO_2 film, only peaks from the underlying Pt film. The inset of Fig. 3.1(a) shows an electron diffraction pattern of a 20 nm thick HfO_2 deposited on $Pt/Ti/SiO_2/Si$ substrate. The selected area electron diffraction pattern is also characteristic of amorphous HfO_2. The surface roughness of the HfO_2 layers were measured using atomic force

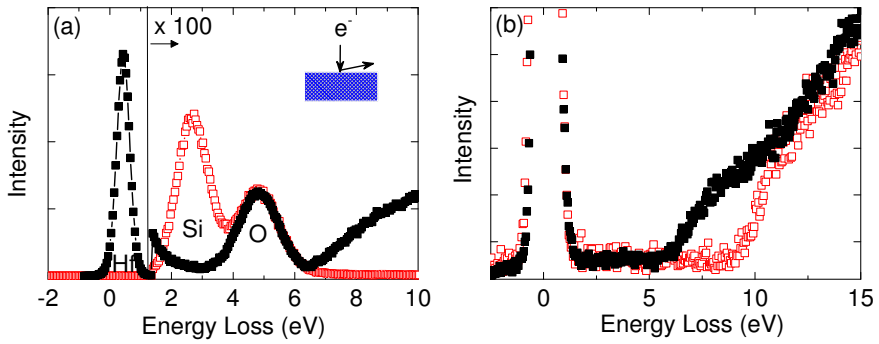

Figure 3.2 (a) Energy loss of spectra of HfO_2 (black closed squares) and SiO_2 (red open squares) for 40 keV electrons backscattered at 135.5^o from sample surfaces. (b) Energy loss spectra measured with 5 keV electrons. This minimum energy loss corresponds to the signature band gap.

microscopy (AFM) in tapping mode. AFM scans were taken over 1 μm $\times$ 1 μm, 2 μm $\times$ 2 μm and 5 μm $\times$ 5 μm areas and the roughness calculated for each scan.

The series of NbO_x films were deposited on Si substrates by reactive dc magnetron sputtering from a metal target at room temperature. The stoichiometry of NbO_x was controlled by changing the argon to oxygen mass flow ratio (19:1, 18:2, 16:4, 12:8). The total gas flow was maintained at 20 sccm at a constant total pressure of 4 mTorr and deposition was performed using a constant discharge power of 300 W. The deposition time was constant for all depositions (450 s). It is difficult to measure accurate stoichiometry of oxides grown on Si using RBS because the O signal is superimposed on a background due to ions backscattered from Si. To overcome this limitation a second set of samples was grown on a vitreous carbon substrate. A relatively thick thermally-grown Nb_2O_5 film was also prepared as a reference by annealing Nb metal for 30 minutes at 600° C in an oxygen ambient. The as-deposited NbO_x films were also amorphous as shown in Fig. 3.1(b).

3.3. High-Energy Electron Scattering Analysis

3.3.1. ALD HfO_2

Fig. 3.2(a) shows ERBS spectra of HfO_2 and SiO_2 taken with 40 keV electrons incident normal to the surface and detected with a scattering angle of 135.5°. Two

peaks can be observed at energies corresponding to those of electrons elastically scattered from Hf or -Si and -O. The width of the peaks is related to the momentum distribution of the target atoms. Scattering parameters calculated for Hf, Si and O atoms from the ERBS spectrum are shown in Table 3.1. The huge elastic cross-section difference between Hf and O is reflected in their relative peak heights. The intensity of each peak will not only depend on the Hf and O concentrations and scattering cross-sections but also on the inelastic mean free path of electrons in the medium. For better visualization, the Hf peak is divided by 100 and; the O peak for both HfO_2 and SiO_2 is normalized so that both peaks have same area. From the ratio of the elastic peak areas of Hf (or Si) and O we can obtain the nominal stoichiometry using calculated parameters from the NIST electron elastic-scattering cross-section database [114](see Table 3.1). In this case the nominal stoichiometries were confirmed to be 1:2 within 5% for both oxides.

A similar measurement was performed for $E_0 = 5$ keV as shown in Fig. 3.2(b). In this case the where elastic scattering peaks are not resolved. These spectra clearly show the onset electron excitations in HfO_2 and SiO_2 at the band gap energy. For HfO_2 the onset is observed at 6.1 eV and for Si it is 9.1 eV. Since the electrons lose 0.4 eV during elastic scattering from Hf, the onset at 6.1 eV corresponds to an inelastic energy loss of 5.7 eV, consistent with the reported bandgap of HfO_2 [115]. Similarly, the bandgap of SiO_2 is measured to be 8.7 eV, consistent with the value reported in Ref. [116].

In Fig. 3.3 we show ERBS spectra of HfO_2 on SiO_2 for different thicknesses of HfO_2. These measurements were taken with 40 keV electrons at three different geometries, while keeping the same scattering angle. The elastic peak of Hf is normalized to the same area. Each spectrum in Fig. 3.3 can be considered as a linear combination of scattering from HfO_2 and SiO_2. It is reasonable to consider an exponential attenuation of the elastic peak as a result of inelastic excitation along the incoming and outgoing path of electrons. Therefore, the intensities of I_{Hf}, I_{Si}, and I_O for a HfO_2 layer on SiO_2 can be expressed as:

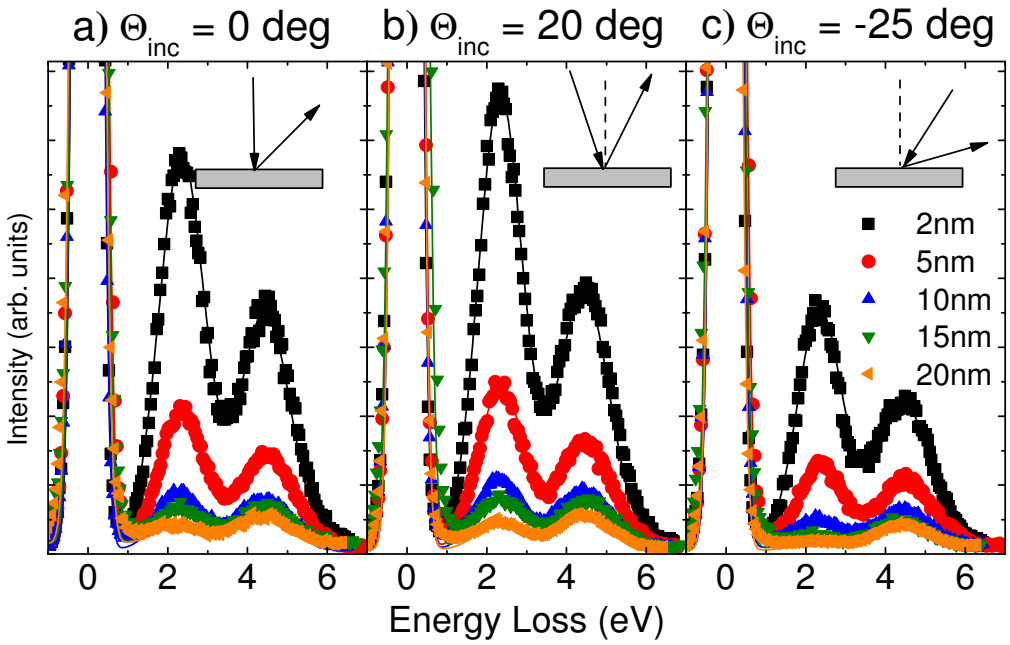

Figure 3.3 Energy loss spectra taken with 40 keV electrons on different thickness of HfO_2 deposited on SiO_2 for normal (a), tilted (b) and (c) incidences according to sketches displayed in the figure. The Hf peak was normalized to the same area and the solid lines correspond to the best fitting of the data according to Eqs. (3.1-3.3).

$$I_{Hf} = \frac{\alpha C_{Hf}\sigma_{Hf}\lambda_{HfO_2}t}{t_{eff}\,(1-\exp(-t_{eff}/\lambda_{HfO_2}))} \tag{3.1}$$

$$I_{Si} = \frac{\alpha C_{Si}\sigma_{Si}\lambda_{SiO_2}t}{t_{eff}\,(1-\exp(-t_{eff}/\lambda_{HfO_2}))} \tag{3.2}$$

$$I_{Si} = \frac{\alpha C_{Si}\sigma_{O}t}{t_{eff}\,(C^{HfO_2}\lambda_{HfO_2}\,(1-\exp(-t_{eff}/\lambda_{HfO_2})) - C^{SiO_2}\lambda_{SiO_2}\exp(-t_{eff}/\lambda_{HfO_2}))} \tag{3.3}$$

respectively, where σ_x and C_x are the elastic cross-section and concentration for the element x. Note that there are two concentrations ($C_O^{HfO_2}$, $C_O^{SiO_2}$) for the O atoms. The inelastic mean free path in SiO_2 and HfO_2 are denoted by λ_{HfO_2} and λ_{SiO_2} respectively (λ_{HfO_2} =33 nm, λ_{SiO_2}= 55 nm) and $t_{eff} = t(1/\cos\Theta_1 + 1/\cos\Theta_2)$ is the maximum trajectory length through an overlayer of thickness t. Θ_1 and Θ_2 are the angles of incidence and detection relative to the surface normal, and t is the thickness of the sample. The common constant, α depends on time, current, spectrometer solid angle and detector efficiency.

Table 3.1 Parameters used to simulate the ERBS spectrum from Eq. (3.1-3.3) for 40 keV electrons. Peak position was taken from the relativistic kinematical factor [117]. The peak width (FWHM) is taken from the mean kinetic energy according to [118]. The energy resolution is 0.3 eV. The inelastic mean free paths are 33 nm and 55 nm for HfO_2 and SiO_2 respectively, were used.

Element	Cross-section σ_x (cm^2/sr)	Relative to Rutherford	Concentration C_x (10^{22} atoms/cm^3)	Peak position (eV)	Peak FWHM (eV)	Mean kinetic energy (meV)
Hf	1.23×10^{-20}	1.92	2.77	0.44	0.35	37
Si	2.18×10^{-22}	0.92	2.33	2.78	1.28	68-78
O	6.87×10^{-23}	0.89	5.53(HfO_2)	4. 88	1.43	60-68
			4.66 (SiO_2)	4. 88	1.43	60-68

Table 3.2 Results for the thicknesses of HfO_2 and SiO_2 films according to ERBS, RBS and MEIS techniques. Also presented AFM measured roughness.

Nominal (nm)	ERBS (nm)	RBS (nm)	MEIS (nm)	AFM R_{RMS}(nm)
2	2.1	1.8	1.9	0.18
5	5.6	4.7	—	0.16
10	10.2	9.0	10.5	0.27
15	14.6	13.7	—	0.31
20	19.0	19.2	20.5	0.30

Fig. 3.3 shows best fits to the measured spectra based on Eqs. (3.1-3.3). The area under each spectrum corresponds to the sum of Gaussian function for each element, where the path widths are fixed, as determined from thick-film measurements, such as Fig. 3.3 . The normalization constant α was then adjusted to match the measured spectra and thereby determine the film thickness. Table 3.2 compares the thickness of the HfO_2 films measured by different techniques. This measurement validates the layer-by-layer growth mode of ALD as according to Eq. 3.2 the signal of Si would be attenuated differently for rougher HfO_2 layers. This is consistent with AFM analyses that show that the root mean square (RMS) roughness of the HfO_2 film is about 1.5-9% of the thickness of the film as show in Table 3.2.

In this case the measured stoichiometries result in a 5-10% uncertainty, which may arise from a number of sourcees including uncertainties in IMFP. For thinner films it is observed that the thickness measurement mainly depends on λ_{SiO_2} [Eqs. (3.1-3.3)], whereas for thicker films it depends on both λ_{SiO_2} and λ_{HfO_2}. The measured uncertainty of λ_{SiO_2} and λ_{HfO_2} at these energy ranges is of the order of 10%.

Selected HfO_2 samples were also analyzed by standard RBS and MEIS techniques. Because these layers were grown on SiO_2 it was difficult to to extract the oxygen content of the HfO_2 film. Therefore, we estimated the thickness of HfO_2 by measuring the area of Hf peak relative to Si contribution from SiO_2 and assuming that the films were stoichiometric. A similar approach was used for MWIS analysis.

Fig. 3.4 shows the measured MEIS spectra of 2 nm HfO_2 measured with 100 keV H^+ ion at three different geometries. Analysis was done using simulation software

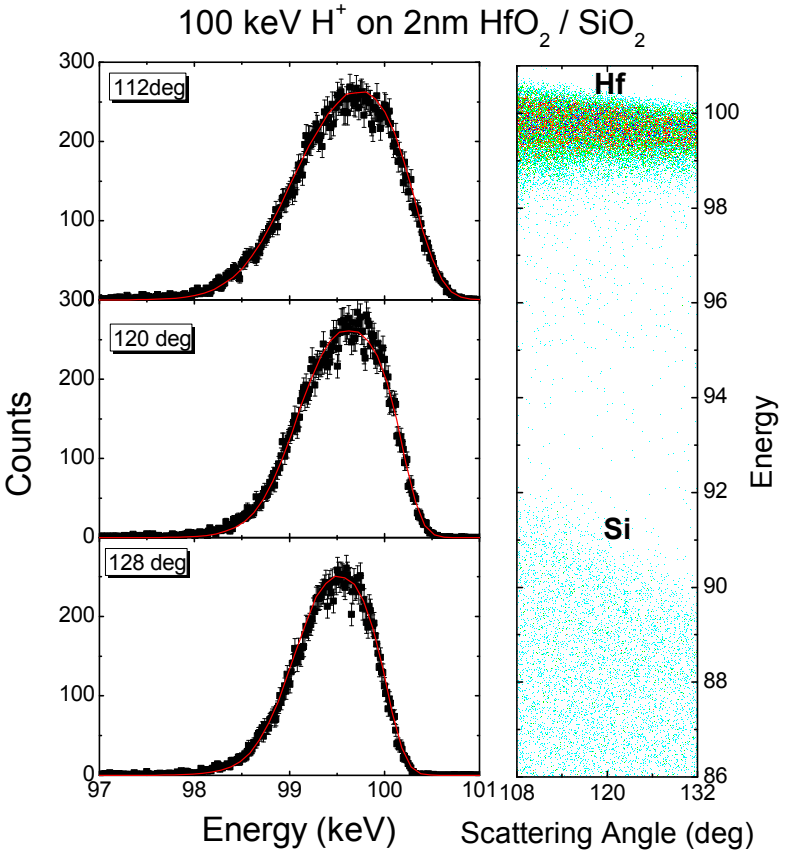

Figure 3.4 Typical MEIS spectra for 100 keV H^+ on the 2 nm HfO_2 sample. The incoming beam is along the surface normal. On the right the 2D map of scattering intensities as a function of detected energy at different scattering angles.

PowerMeis [119]. The experimental measurement shows a homogeneous and unform thickness of HfO_2 with a sharp SiO_2/HfO_2 interface. Similar behavior is observed for other samples. The MEIS and RBS results are compared with ERBS and shown in Table 3.2. For RBS and MEIS analyses, the stopping power was determined from SRIM [120], and in the MEIS case straggle values were calculated from the Yang-O'Connor-Wang formula [120].

3.3.2. Sputtered NbO_x

In Fig. 3.5 the ERBS spectrum of a NbO_x film deposited on Si at a high oxygen partial pressure ($Ar:O_2$ = 12:8) is compared with thermally grown Nb_2O_5. The plasma deposited film shows three distinct peaks corresponding to Nb (main peak), Si (central peak) and O (peak at highest energy loss). The energy difference between

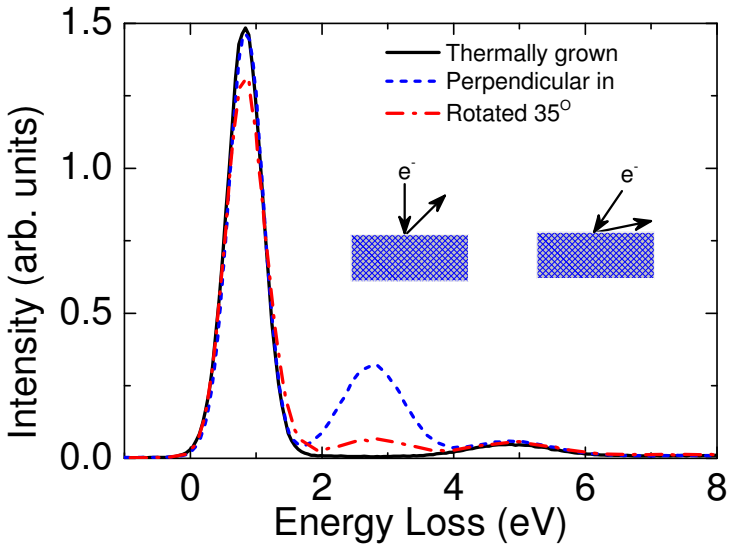

Figure 3.5 The energy loss spectra in the elastic peak region for a NbO_x sample (Ar:O_2=12:8) for two different geometries compared to the spectrum of a thick, thermally grown Nb_2O_5 layer.

the Nb and Si peaks is ∼2 eV, and that of Si and O is ∼4 eV. These values are in good agreement with calculated values based on elastic scattering (1.95 and 4.04 eV). The contribution of Si is reduced by rotating the sample 35°, which makes the measurement more surface sensitive. In this geometry, the outgoing beam is 80° from the surface normal. As described in the previous section, the thickness and stoichiometry of NbO_x can be calculated from the peak area of Nb and O. The corresponding values are 9 nm and x=2.9, assuming an inelastic mean free path in Nb_2O_5 of 41.5 nm. It is worthwhile to point out that the thickness obtained for the measurements at the two different geometries was the same.

Fig. 3.6 shows spectra of NbO_x films deposited with different O partial pressure, where Nb peaks were normalized to unity. Interestingly, now the Nb:O peak area ratio depends on the O_2 partial pressure. For the 16:4 mixture the peak area ratio can still not be distinguished from that of the thermally grown film, but for films deposited at the lower oxygen flow rate the O peak is clearly less intense and the films are sub-stoichiometric (compared to Nb_2O_5).The thickness and stoichiometry calculated from these spectrum are summarized in Table 3.3 and compared with RBS analysis. It is important to note that a Si peak is observed for the 16:4 mixture due to a thinner oxide layer, while indicating much thicker overlayers for other conditions.

Table 3.3 Comparison of thickness and stoichiometry as obtained by ERBS and RBS as function of oxygen flow rate during deposition. Note however, that a separate series of samples are grown same time on carbon for RBS analysis.

$Ar : O_2$	t (nm) ERBS	Nb_2O_x ERBS	t (nm) RBS	Nb_2O_x RBS
191:	>50	Nb_2O_4	93	$Nb_2O_{4.3}$
18:2	>50	$Nb_2O_{4.3}$	88	-
16:4	39	Nb_2O_5	37	$Nb_2O_{5.5}$
12:8	9	Nb_2O_5	8	$Nb_2O_{5.8}$

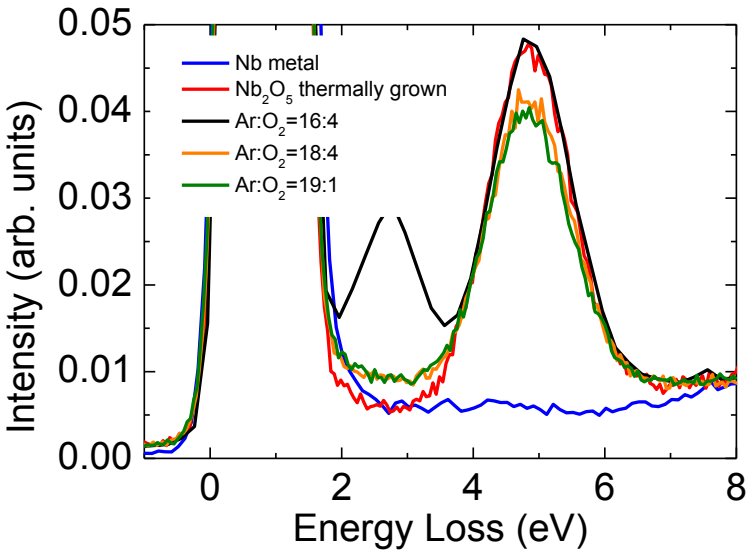

Figure 3.6 (a) The elastic peak region of the loss spectra of NbO_x for different oxygen flow rate of oxygen is compared with Nb (metal) and different thermally grown Nb_2O_5 .

To determine the band gap of NbO_x films, the incident electron beam energy was reduced to 5 keV. The energy loss spectra for samples deposited with an $Ar : O_2$ pressure ratio of 16:4 and 19:1 are shown in Fig. 3.7. For sample 16:4 the stoichiometry is close to Nb_2O_5 and the onset of the inelastic energy loss is ∼3.8 eV, which is higher than the usual band gap of Nb_2O_5 (3.4 eV). For the sample with a stoichiometry close to Nb_2O_4, there is an increase of the loss spectrum at a similar energy loss, but there is extra intensity extending all the way to the elastic peak. This behavior is quite universal. We have observed it for other oxides and it has been seen in many other REELS experiments (see Ref. [121]). The tail extending from the elastic peak region is believed to be due to partial filling of states where the cation is not fully oxidized.

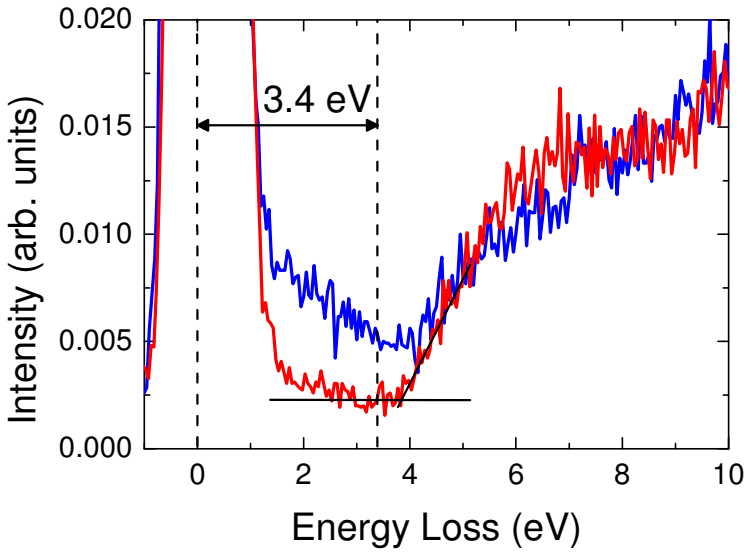

Figure 3.7 Energy loss spectra taken at 5 keV for samples grown with an Ar:O_2 pressure ratio of 16:4 (red line) and 19:1 (blue line). The sample grown under low O_2 flux has a less pronounced minimum after the elastic peak.

3.4. Conclusion

In summary, we have shown that the ERBS technique can be used to determine the stoichiometry and the thickness of thin oxide films, and to provide information about their electronic structures. Such information was use in the present study to optimize film stoichiometry for particular applications.

CHAPTER 4

Effect of Electrode Roughness on ReRAM Reliability

4.1. Introduction

Resistive random access memory devices (ReRAM) generally require an electroforming step to initiate resistive switching [122, 123]. This step is analogous to soft dielectric breakdown and results in a filamentary conductive path through the dielectric. The electrochemical model of breakdown considers a dielectric film subjected to a uniform electric field and predicts the random and homogeneous generation of defects within the dielectric layer [51, 52]. In this model the concentration of defects gradually increases to a percolation threshold for continuous conduction at which point there is a sudden increase in current. In reality breakdown is usually a heterogeneous process, dominated by intrinsic defects in the dielectric film and defect generation at the metal/dielectric interface, a process that is accelerated by electric field enhancement at electrode asperities [90, 124–126]. For example, rough electrodes are known to increase the leakage current [88] and reduce the yield of thin-film oxide capacitors [91, 127–129]. The physical understanding of these processes is based on models of the electric field distribution at the metal/dielectric interface. However, these models generally assume a static field distribution and ignore the effect of defect generation and migration (drift and diffusion) on the local electric field distribution.

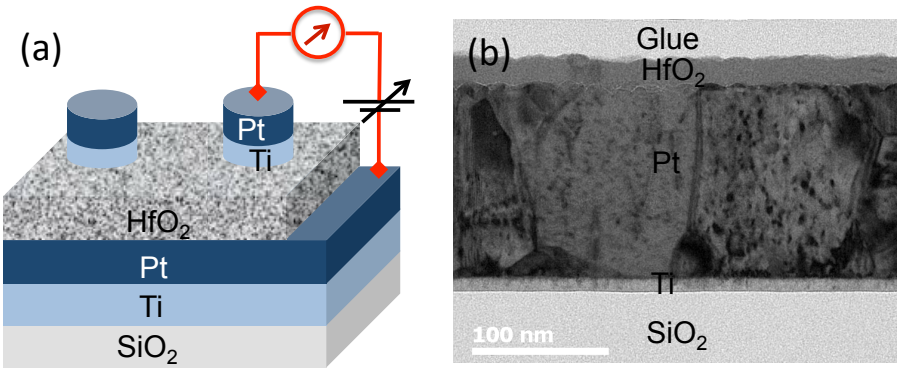

Figure 4.1 (a) Schematic of the device structure and (b) XTEM of a 150 nm Pt with 20 nm HfO_2 showing both bottom and top interfaces.

In this chapter, we investigate the reliability of Pt/Ti/HfO_2/Pt structures as a function of bottom electrode roughness. In addition, we introduce a finite element model of dielectric breakdown that includes the effect of defect generation and migration on the the local electric field to understand the role roughness induced electric field enhancement.

4.2. Experimental Procedure

Simple MIM test-structures, as shown in Fig. 4.1(a), were fabricated on thermally oxidized (100) silicon wafers with an oxide thickness of 300 nm. The bottom electrodes comprised a 10 nm Ti wetting layer and a Pt layer with a thickness in the range from 25-150 nm. These films were deposited by electron beam evaporation without breaking vacuum and were deposited at an average rate of 2 Å/s for both Ti and Pt. The film thicknesses were determined by a crystal oscillator during deposition and subsequently confirmed by cross-sectional transmission electron microscopy (TEM). A 20 nm thick HfO_2 layer was deposited on the Pt bottom electrode by atomic layer deposition (ALD). This was achieved by heating the sample to 200° C and exposing it to alternate pulses of tetrakis-(dymethylamido)-hafnium (TEMAH, $Hf(NMe_2)_4$) and H_2O vapor, with an N_2 purge between pulses. Top electrodes of 150 μm diameter and comprising 10 nm Ti and 50 nm Pt were then deposited through a shadow mask by electron-beam evaporation to complete the asymmetric MIM test structures. The roughness of the bottom Pt electrode and of the deposited HfO_2 film were measured using atomic force microscopy (AFM) in tapping mode. AFM scans were taken

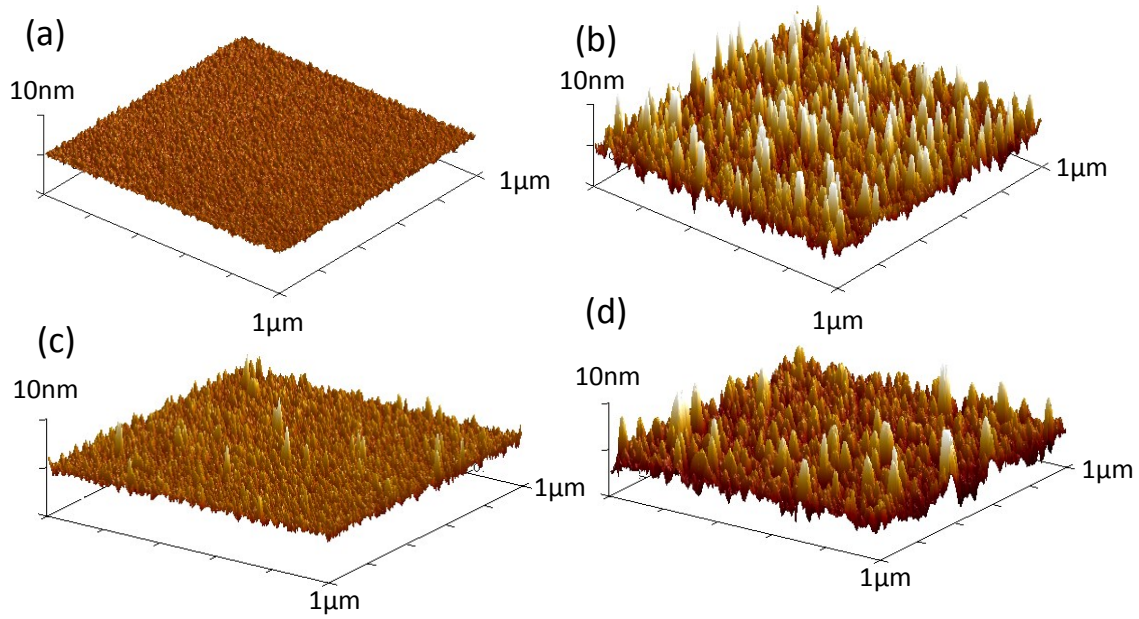

Figure 4.2 3-D topography AFM images of (a) 25 nm and (b)150 nm as grown Pt films. (c) 25 nm and (d) 150 nm Pt after 20 nm HfO_2 deposition, which corresponds to the top interface.

over 1 μm $\times$ 1 μm, 2 μm $\times$ 2 μm areas and the roughness calculated for each scan to confirm that the measurement was independent of scan area.

4.3. Effect of Roughness on ReRAM

4.3.1. Roughness of Pt Electrodes

A TEM image of a 150 nm thick Pt bottom-contact layer is shown in Fig. 4.1(b). The film is observed to be polycrystalline with individual grains having lateral dimensions in the range 50-100 nm. The roughness of the bottom electrode is clearly evident but details are difficult to interpret due to the finite thickness of the sample cross-section. More quantitative analysis is provided by AFM imaging of the surface, as shown in Fig. 4.2(a-d). These compare images from the thinnest (25 nm) and thickest (150 nm) Pt electrodes prior to [Fig. 4.2(a-b)] and following [Fig. 4.2(c-d)] HfO_2 deposition and clearly show an increase in film roughness with increasing film thickness. This dependence is shown more explicitly in Fig. 4.3(a), which plots the root-mean-square (RMS) roughness of the bottom electrode before and after HfO_2 deposition as a function of Pt film thickness. This shows that the RMS roughness varies by a factor of 6-7 between the thinnest ($R_{RMS} = 0.44$ nm) and thickest ($R_{RMS} = 2.62$

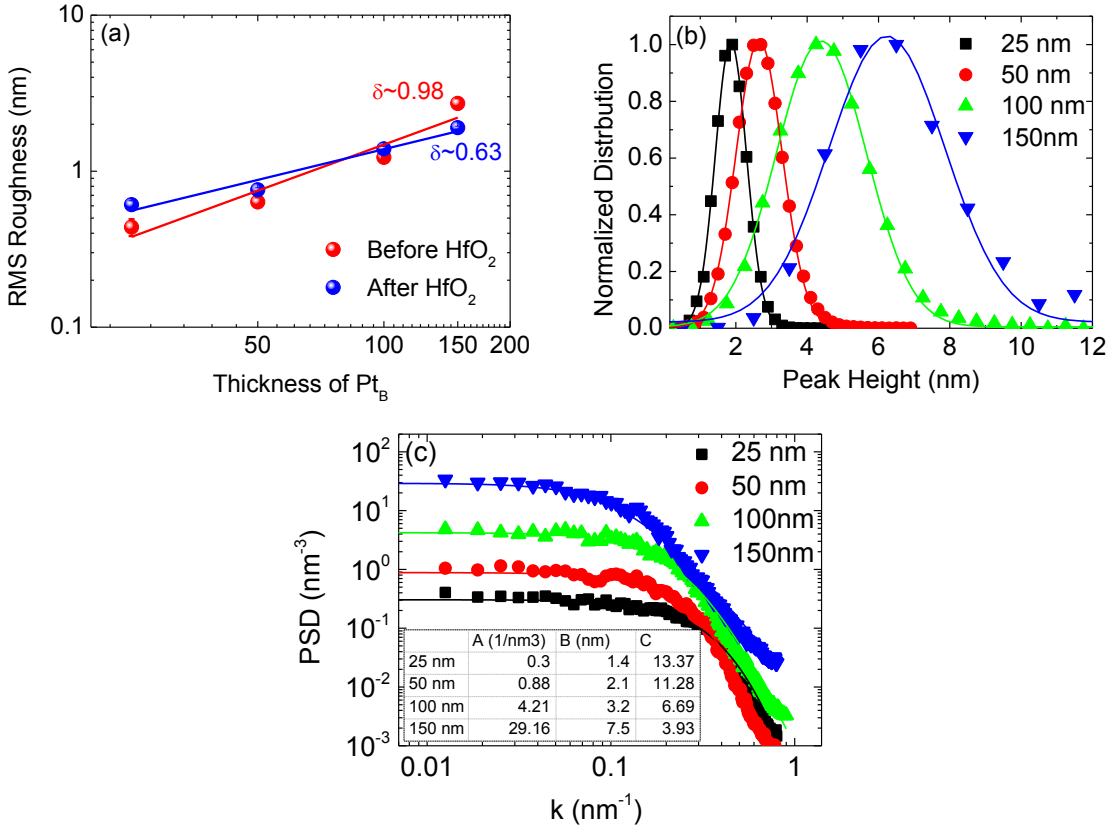

Figure 4.3 (a) RMS roughness of bottom Pt electrode before and after HfO_2 deposition as a function of film thickness. (b) Height distribution of the surface roughness for different thickness of Pt and (c) PSD profiles of the same Pt layers, calculated from AFM measurements. The fit to the ABC model Eq. 4.1 is shown by solid lines. Inset represents fitting coefficients of PSD spectra.

nm) films. The dependence of roughness on film thickness is typically described by a power-law equation of the form $R_{RMS} \sim t^{\delta}$ where R_{RMS} is the root-mean square roughness, t is the film thickness and δ is a coefficient that depends on the mode of film growth. In the current case δ is in the range 0.7-1.0, which is consistent with the roughness origination from faceted grain growth [130]. By way of comparison, the SiO_2 substrate was found to have an RMS roughness of 0.16 nm.

Because dielectric breakdown is a weakest-link process it is expected to depend on extreme features rather than the average or RMS roughness of the electrode. Consequently it is important to consider the full surface-height distribution of the electrodes. Fig. 4.3(b) shows the measured height distribution for each film, where the height is measured relative to the lowest height in the scanned area. It is clear that the thickest bottom electrode has the largest spread in peak heights. Indeed,

the maximum peak-to-valley distance measured for the 150 nm Pt electrode is 25 nm whereas that for the ∼25 nm Pt film is only ∼5 nm.

Finally, we consider the lateral scale of the surface topography. This is achieved by considering the power spectral density (PSD) of the surface height distributions, which decomposes the surface profile into its spatial wavelengths [131]. For a condensed description of the Pt films, the spectra were fitted using the k-correlation model (also called the ABC model) assuming perfectly isotropic surfaces [132]. This model allows quantitative comparison between samples over large length scales.

According to this model, the PSD is defined as

$$\mathrm{PSD} = \frac{\mathrm{A}}{\left(1 + \mathrm{B}^2\mathrm{k}^2\right)^{\mathrm{C}/2}} \tag{4.1}$$

where A, B and C are model parameters and k is the web vector. The amplitude of the PSD is a measure of the roughness component with particular spatial frequency, and the distributions show two regions with different slopes: a relatively flat region at low spatial frequencies and a steeper region at higher spatial frequencies. The parameter A describes the low-frequency ($k \ll B$) limit of the spectrum, where the PSD is constant and equal to A. In this region, there is no significant variation of height in real space. B determines the knee of the PSD and defines a correlation length beyond which the surface height fluctuations are uncorrelated. Beyond this length, the surface is fractal and the PSD is determined by $1/k^C$.

Fig. 4.3(c) shows the measured PSD for the bottom Pt electrodes, together with fits of 4.1 and model parameters shown in the inset. The results confirm the correlation between surface topography and film thickness. For the thinnest layer, the correlation length, B is ∼1.5 nm, which suggests that the roughness is dominated by lateral features with dimensions less than this value. In contrast, for the 150 nm film B is ∼8 nm. Comparison of these curves suggests that the roughness of the thicker films is dominated by large features, consistent with an increase in the Pt grain size with

increasing film thickness [133].

4.3.2. Dielectric Breakdown of HfO_2

Forming measurements were performed by measuring the current between top and bottom electrodes while scanning the applied voltage from 0 to 10 V. The bottom electrode was grounded and the test voltage was applied to the top electrode. An instrumental compliance of 10 μA was applied to avoid permanent damage to the test device. Fig. 4.4(a) shows that the I-V characteristics are asymmetric under positive and negative bias due to the different Schottky barrier heights. However, the effect of electrode roughness is qualitatively the same for both polarities. Here we report data for positive polarities only.

Specifically, a series of dielectric breakdown measurements was performed with a positive bias on top electrode on each sample and representative results are shown in Fig. 4.4(b-d). Fig. 4.4(b) shows cumulative probability distributions depicting the fraction of devices that undergo breakdown at a given voltage.

Analysis of these distributions was undertaken assuming a Weibull distribution [134] which has a cumulative distribution function, $P(V_f)$, defined as

$$P(V_f) = 1 - \exp\left[-\left(\frac{V_f}{\alpha}\right)^{\beta}\right] \tag{4.2}$$

where α is the scale parameter, which is closely related to the mean breakdown voltage, and β is the shape parameter, which is inversely related to the width of the distribution. A small value of β indicates widely dispersed data, i.e., the data tend to distribute over a relatively wide range of breakdown voltages, whereas for large values of β the majority of breakdown tends to fall around the mean voltage. Thus, the reliability of devices can be represented by the Weibull parameters. The solid lines in Fig. 4.4(b) represent least square fits of Eq. (4.2). Comparison of the various distributions and fitting parameters confirm the reduction in mean breakdown voltage

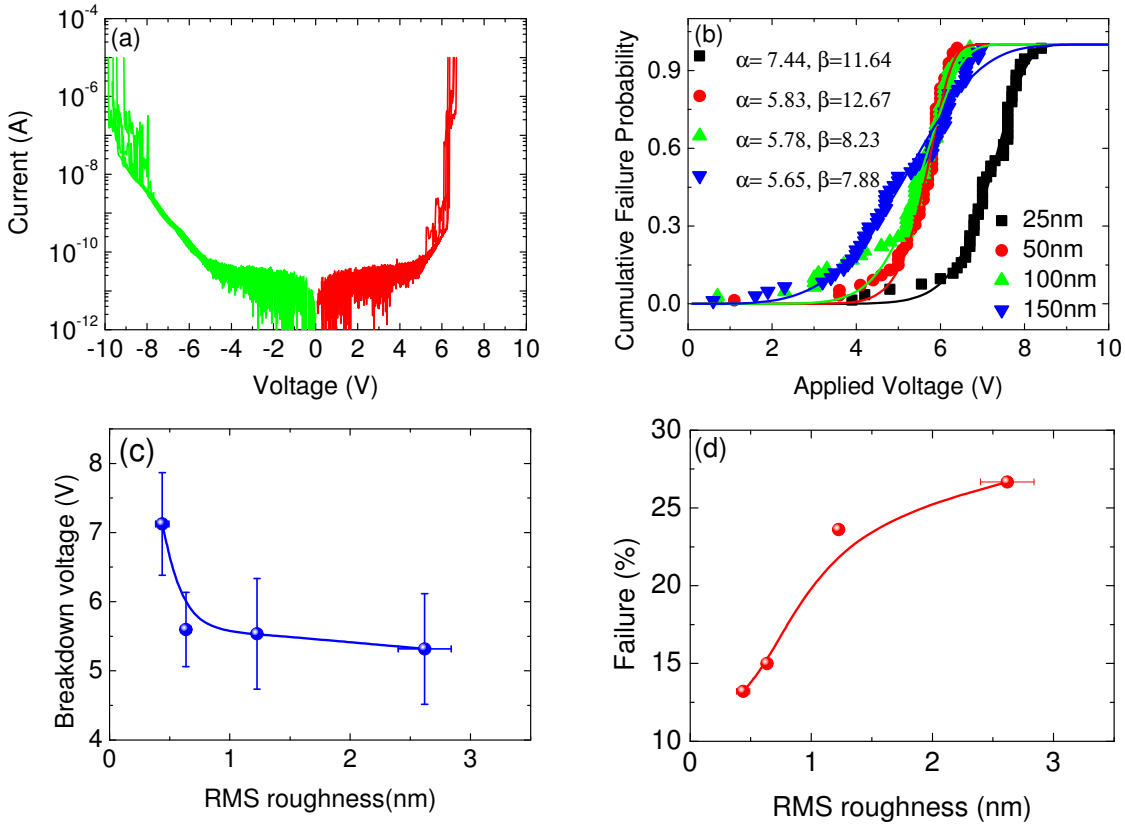

Figure 4.4 (a) Forming characteristics of Pt/Ti/HfO_2/Pt device with both polarities. (b) Weibull distribution of forming voltage of Pt/Ti/HfO_2 /Pt as a function of bottom electrode thickness. Variation of (c) breakdown voltage and (d) failure with RMS roughness.

and a significant increase in dispersion of the breakdown voltage with increasing bottom electrode thickness (roughness).

The effects of electrode roughness on the mean breakdown voltage of MIM devices, such as that shown in Fig. 4.4(c), highlight a reduction in voltage with increasing electrode thickness. The reduction in breakdown voltage can arise from roughness-induced variations in the thickness [135, 136], variations in the structure and quality of the deposited dielectric film [137]; an increase in the effective surface area of the device [138]; or local electric field enhancement in the vicinity of high aspect-ratio asperities [90]. The first of these effects is particularly evident for films deposited from directional sources, such as evaporation or sputter deposition, where shadowing by surface features is significant [135, 136]. This is not a significant problem for films deposited by ALD as these have been shown to grow conformally on surfaces with complex morphologies, including nanowires, nanoparticles and high-aspect ratio

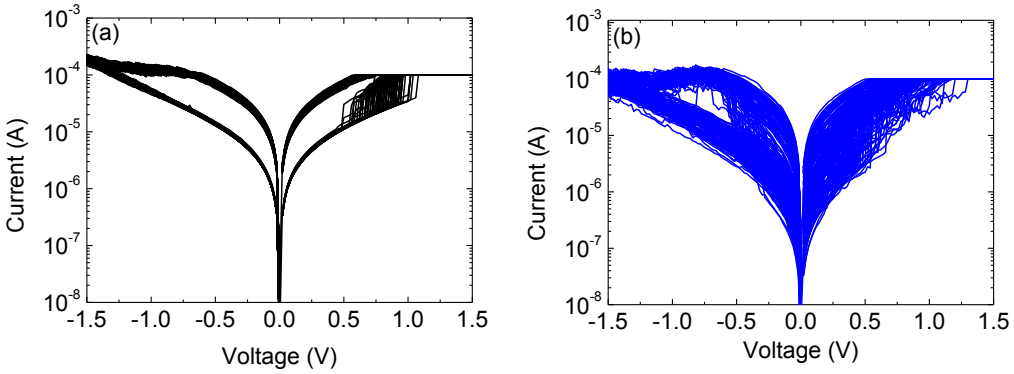

Figure 4.5 DC switching characteristics of Pt/Ti/HfO2/Pt device with (a) 25 nm Pt and (b) 150 nm Pt bottom electrode.

trenches. However, an increase in the density of intrinsic defects with increasing substrate roughness can still be expected for ALD films [139–144] and is consistent with the increase in the device failure rate with increasing roughness shown in Fig. 4.4(d). Here the failure rate is the fraction of test devices found to be in a low resistance state prior to testing (i.e. device yield). These data show that the average forming voltage, V_f, and device yield both decrease with increasing mean surface roughness.

4.3.3. Switching Characteristics

The DC resistive switching characteristics of devices with the smoothest and roughest electrodes are compared in Fig. 4.5. These measurements show that the reliability (i.e. variations in SET/RESET voltage and resistance during repetitive DC switching cycles) and endurance are significantly worse for rough electrodes than for smooth electrodes, despite the reduction in forming voltage. This is attributed to an increased probability for random filament generation during the set process. However, such behaviour is also expected to depend on device area as both forming and the probability for random filament generation will depend on the number of dominant asperities within the active device area [86, 87]. One possible implication of this is that a smaller cell with a single dominant asperity (patterned electrode) may result in better uniformity and reliability.

4.3.4. Modeling of Forming Process

4.3.4.1. Model Physics

To gain insight into the significance of field-enhancement effects on forming a finite element model was developed to simulate local field enhancement and defect dynamics, including the role of defect generation and migration on the electric field distribution. The model is a relatively simple representation of the physical system and does not include detailed chemical (e.g. reduction of HfO_2 by Ti) or electrical effects (i.e. Schottky barrier heights, depletion layers, etc.). However, it does capture the essential physics of the electroforming process and because defects are generated in the vicinity of electrodes (due to the local field enhancement in this region) it is consistent with the current understanding of oxygen vacancy generation at the metal-insulator interface. Specifically it comprises a 2D axisymmetric model of a 20 nm HfO_2 layer sandwiched between two Pt electrodes, one of which has a Gaussian shaped asperity.

The model assumes that charged defects are generated by the applied field; that defects can drift and diffuse in the dielectric film; and that the presence of defects modifies the local conductivity of the dielectric. According to the thermochemical model [51, 52], the local electric field distorts molecular bonds and reduces the activation energy required for defect generation. These defects are assumed to be charged (e.g. positively charged vacancies V_O^{2+}) and to migrate by drift and diffusion, driven by the local electric field and Joule heating. Their presence also increases the local conductivity of the dielectric (HfO_2) in the present case).

Defect generation, drift and diffusion is described by the transport equation:

$$\frac{\partial \mathrm{n_D}}{\partial \mathrm{t}} = \nabla \cdot \mathrm{D}\left(\nabla \mathrm{n_D} - v\mathrm{n_D}\right) + \mathrm{G} \tag{4.3}$$

where D the is defect diffusivity, v the defect drift velocity and G the defect generation rate. The diffusion coefficient is assumed to be independent of defect concentration,

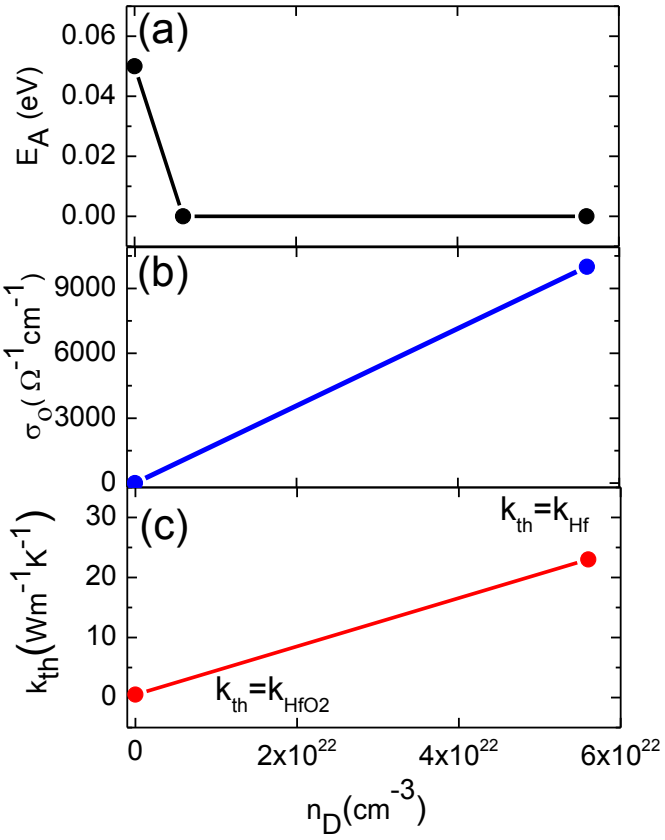

Figure 4.6 (a) Activation energy, E_{AC} as function of defect density n_D (b) electrical conductivity pre-exponential factor σ_0, and (c) thermal conductivity k_{th} as a function of local defect density n_D.

and its temperature dependence to be described by an Arrhenius relation:

$$\mathrm{D} = \mathrm{D}_0 \exp(-\mathrm{E_A}/\mathrm{k_B T}) \tag{4.4}$$

where D_0 is a preexponential factor, E_A is the defect migration energy, k_B is Boltzmann constant and T is the temperature. The ion mobility μ is assumed to be related to diffusivity through the Einstein relation:

$$\mu = \frac{\mathrm{qD}}{\mathrm{k_B T}} \tag{4.5}$$

The defect generation rate, G, is defined as

$$\mathrm{G} = \mathrm{G}_0 \mathrm{exp}\left(\frac{\mathrm{E_b} - \gamma\varepsilon}{\mathrm{k_B T}}\right) \tag{4.6}$$

where G_0 is a pre-exponential constant, E_b is the energy to form an oxygen vacancy at zero electric field, γ is the bond polarization factor [52] and ε is the local electric field. The electric field and current distributions were determined from the continuity equation:

$$\nabla \cdot \sigma \nabla \psi = 0 \tag{4.7}$$

where σ is the local electrical conductivity of the dielectric layer and ψ is the potential.

Following the work of Larentis *et al.* [145] the electrical conductivity σ is assumed to vary between semiconducting and metallic behavior depending on the defect density. This is represented by an Arrhenius equation $\sigma = \sigma_0 exp(-E_{AC}/k_B T)$ in which the pre-exponential factor, σ_0, and the activation energy, E_{AC}, depend on the defect concentration, as shown in Figure 4.6(b,a) respectively. The thermally activated conductivity is consistent with Poole-Frenkel conduction, which has a relatively low energy barrier for conduction [146]. The initial activation energy, E_{AC} is considered to be 0.05 eV at $n_D = 0$, which is in agreement with the semiconducting state of HfO_x based ReRAM [147]. E_{AC} then decreases for increasing n_D and becomes zero at $\mathrm{n_D} = 6 \times 10^{21}$ $\mathrm{cm^{-3}}$ (i. e. metallic) [Fig. 4.6(a)]. This assumption is based on the fact that the conducting filament is equivalent to a highly doped semiconductor, where the Fermi level is very close to, or even above, the conduction/valance band [146]. The pre-exponential factor for insulating HfO_2 is taken as $\sigma_0 = 10^{-6}$ $\Omega^{-1} cm^{-1}$ and that of the metallic filament as $\sigma_0 = 10^4$ $\Omega^{-1}\mathrm{cm^{-1}}$ at $\mathrm{n_D} = 6 \times 10^{22}\mathrm{cm^{-3}}$ as shown in Fig. 4.6(b). The threshold value for conducting HfO_2 is $\mathrm{n_D} = 6 \times 10^{21}\mathrm{cm^{-3}}$, which corresponds to 10% of oxygen vacancies for p-type conductivity. These assumptions are based on the experimental results of Hildebrandt *et al.* [148].

The temperature distribution was determined from the Fourier heat equation:

$$\rho \mathrm{C_p} \frac{\partial \mathrm{T}}{\partial \mathrm{t}} - \nabla \cdot \mathrm{k_{th}} \nabla \mathrm{T} = \mathrm{Q} \tag{4.8}$$

where ρ is the mass density, C_p is the specific heat, k_{th} is the thermal conductivity and $Q = |\sigma \nabla \psi|^2$ is the heat flux density supplied by the electric current. Following

Table 4.1 Simulation parameters used in the forming model of HfO_2

Parameter	Value	Reference
D_0	$2 \times cm^{-2}s$	[145]
E_A	1 eV	[149]
E_b	2.8 eV	[150]
γ	10.13 eÅ	[51]
n_A	5.54×10^{22} cm^{-3}	[148]
G_0	7×10^{13} Hz	[51]
C_p	60 $Jkg^{-1}K^{-1}$	[151]
k_{HfO_2}	0.5 $Wm^{-1}K^{-1}$	[152]
k_{Hf}	23 $Wm^{-1}K^{-1}$	[153]

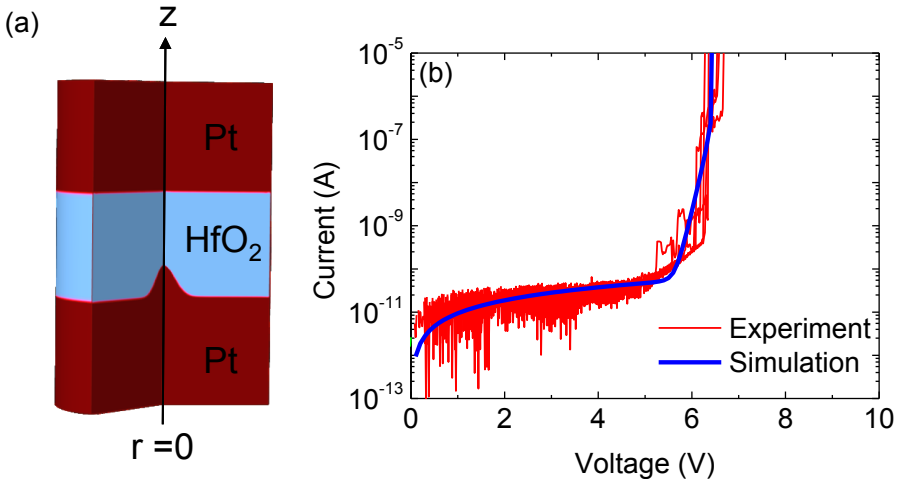

Figure 4.7 (a) Schematic of the simulated device structure with a Gaussian asperity at the bottom interface. (b) Comparison of experimental and simulated current-voltage characteristics obtained by applying ramp bias.

Larentis *et al.* [145], a linear relationship between k_{th} and n_D is assumed as shown in Fig. 4.6(c). The minimum value of thermal conductivity, k_{HfO_2} (0.5 $Wm^{-1}K^{-1}$) refers to the thermal conductivity of the insulating HfO_2. The maximum k_{th} value at high n_D corresponds to that of the metallic conducting filament, and is assumed to be that of Hafnium, k_{Hf} (23 $Wm^{-1}K^{-1}$ [153]). All parameters and values used in the simulation are listed in Table 4.1.

The simulation therefore involves the self-consistent solution of the drift-diffusion equation for defect transport with a source term given by G [Eq. (4.6)], the continuity equation for electrical conduction [Eq. (5.1)] and the Fourier heat equation [Eq. (5.2)] including Joule heating.

4.3.4.2. Forming Process

The effect of surface roughness was modeled by adding a simple Gaussian shaped asperity to the bottom electrode, centered on the symmetry axis [Fig. 4.7(a)]. This shape helps to avoid singularities caused by sharp edges and gives numerical simplicity. The height and width of the asperity were varied to study the effects of the asperity aspect ratio on breakdown. Note however that the model differs from the experimental situation in that the upper electrode is assumed to be flat rather than reflect the conformal growth of the dielectric layer on the bottom electrode. A voltage ramp was applied across the electrodes with a step size of 1 V/s. Nonetheless, the simulation captures the essential features of the breakdown process as is evident from Fig. 4.7(b). This compares a calculated breakdown characteristic with experimental data, and clearly reproduces the most important and obvious features of the measurements. In both cases the current is observed to increase slowly with increasing voltage before rising rapidly at the point of breakdown, which represents a soft breakdown process prior to the irreversible thermal runaway characteristic of hard breakdown.

Since electrode topography alters the local electric field, it will also alter the defect generation rate and thereby modify the breakdown behavior. This is illustrated in Fig. 4.8 (a), which shows the initial electric field distribution in the vicinity of a Gaussian asperity of height 2 nm and FWHM (hereafter referred as width) of ∼20 nm. Both the average electric field and the peak field increase in the vicinity of the asperity, as expected. Consequently, as the applied voltage increases defects are preferentially generated in the vicinity of the asperity [Fig. 4.8(b)]. Once generated they drift towards the anode to create a filamentary conduction path through the dielectric layer [Fig. 4.8(c)]. The development of the filament confines the electric current and causes an increase in the local temperature due to Joule heating [Fig. 4.8(d)]. This accelerate defect generation and leads to soft dielectric breakdown, as shown previously in Fig. 4.7.

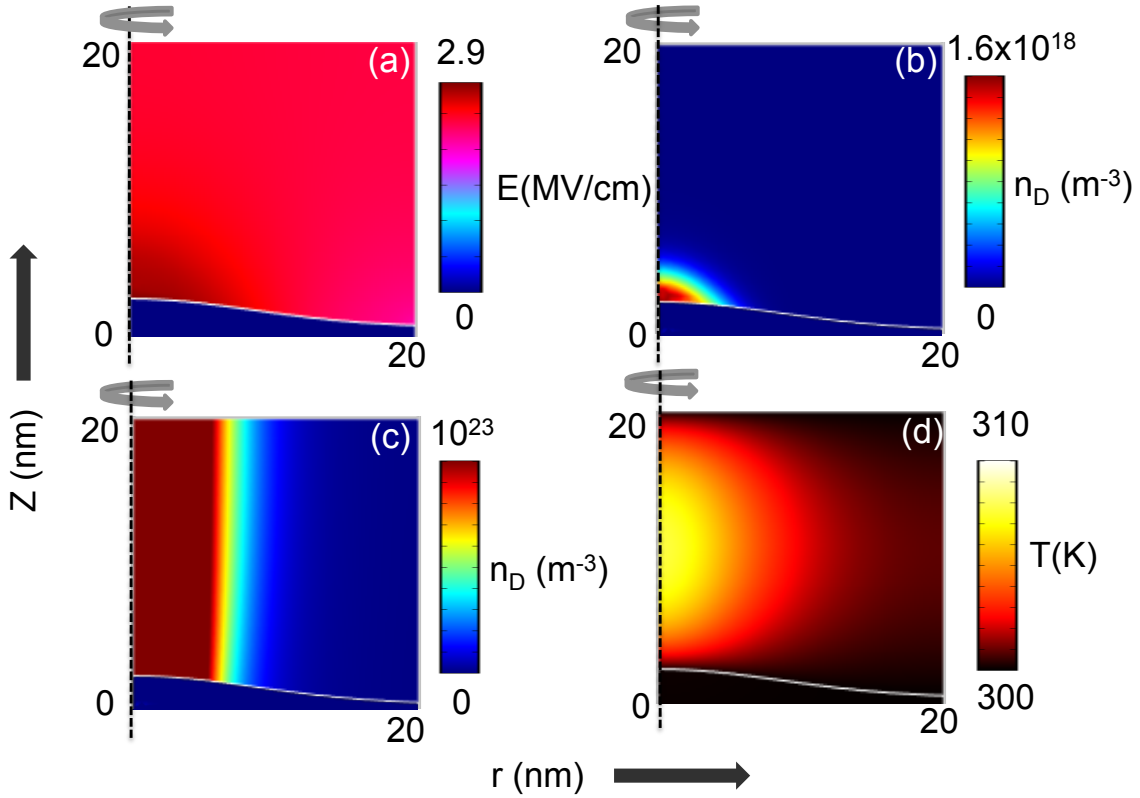

Figure 4.8 (a) 2D plot of Electric field ($E = -\nabla\psi$) and (b) defect density n_D at critical field with an asperity height of 2 nm. Both electric field and defect density are concentrated on the top of asperity. (c) Defect density n_D and (d) temperature T distributions at forming voltage in the same device structure.

4.3.4.3. Defect Moderation of Field Enhancement

As an approximation, the local electric field at the asperity, E_{loc}, can be expressed as $E_{loc} = \eta E_{app}$, where η is a field enhancement factor and $E_{app} = V_{app}/d$, is the average electric field across the dielectric in the absence of any asperities, with V_{app} the applied voltage and d the thickness of the layer. In general η has a complicated dependence on the height, width and aspect ratio of an asperity [88]. The sensitivity of field enhancement factor η to the shape of the asperity can be estimated from comparison of η versus aspect ratio (h/w) of the Gaussian asperity. The geometric field enhancement factor (η) is plotted as a function of aspect ratio in Fig. 4.9(a). This is well represented by a curve of:

$$\eta = \mathrm{p} + \mathrm{m}\left(\frac{\mathrm{h}}{\mathrm{w}}\right)^{\mathrm{n}} \tag{4.9}$$

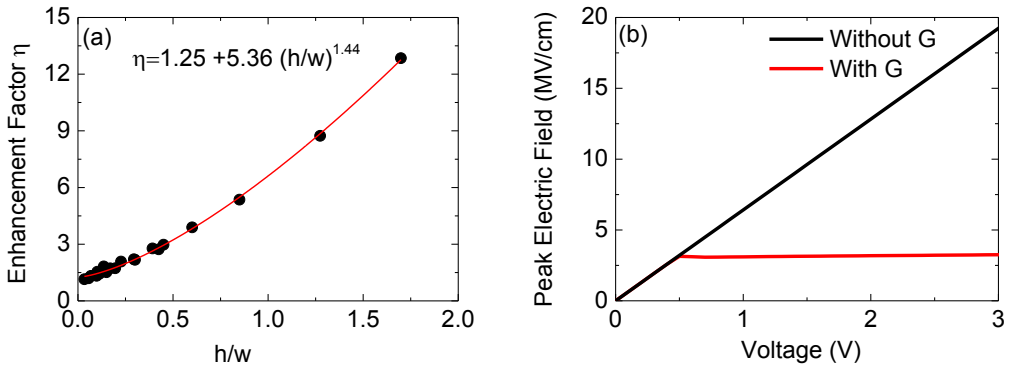

Figure 4.9 (a) The electric field enhancement (η) factor as a function of width of the asperity. The solid line is a fit by a power law. (b) Peak field as function of applied field with and without defect generation for an asperity of 8 nm height and width 4.71 nm.

where p, m and n are fitting parameters depending on the geometry of the asperity. To demonstrate that defects can moderate electric field simulations were performed with and without defect generation. Fig. 4.9(b) shows the peak electric field as a function of applied voltage for an asperity of height 8 nm, and width 4.71 nm. The peak field is observed to increase linearly with voltage when defect generation is neglected but to saturate at 2.9 MV/cm when defect generation is included. This is clear evidence that the generation of defects acts to moderate geometric field enhancement.

Fig. 4.10(a) summarizes the effect of the asperity shape on the forming voltage by plotting the calculated voltage as a function of the peak height and width of the bottom electrode asperity. An increase in peak height is shown to reduce the forming voltage, consistent with the fact that it acts to reduce the local film thickness and increase the local electric field. For a fixed asperity width of ∼4.6 nm the forming voltage is shown to decrease from ∼6.5 V to ∼4.4 V as the asperity height increases from 2 to 8 nm. This reduction is of similar order to that observed experimentally. In contrast, changes in the width of the asperity have only a weak effect on the forming voltage, reducing it by just a few percent for width variations of more than an order of magnitude. This is a much smaller effect than expected from the calculated field enhancement.

The effect of defect moderation of the electric field is reflected in Fig. 4.10(b), which

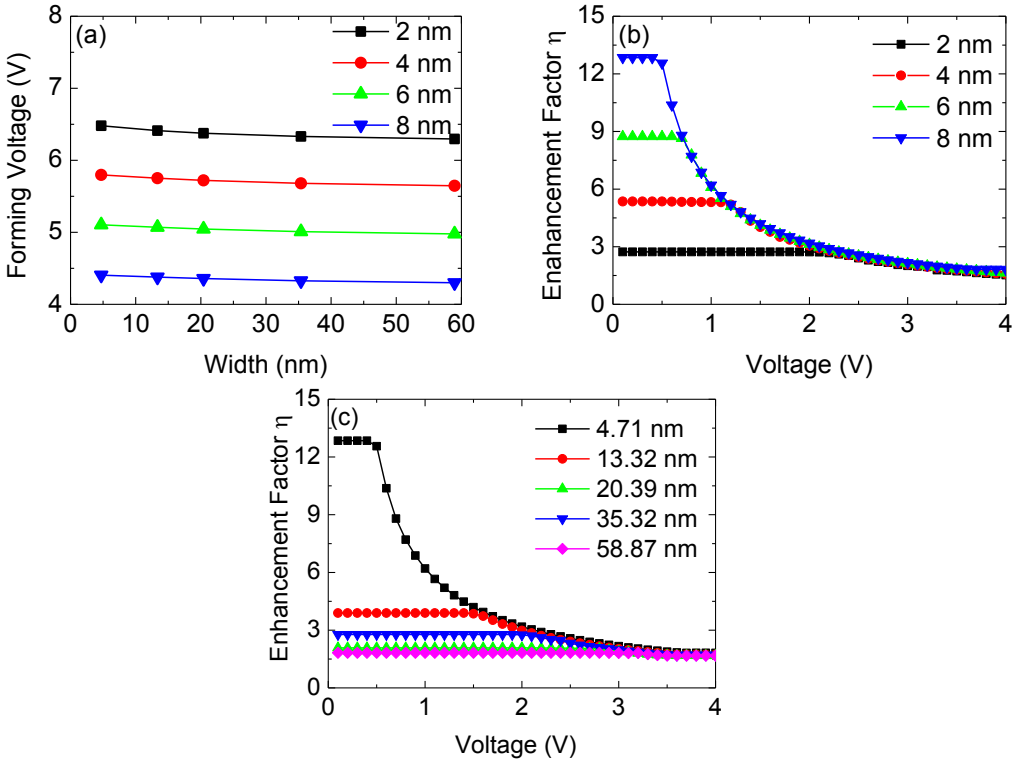

Figure 4.10 (a) Forming voltage as a function of height and width of the asperity. (b) Electric field enhancement factor as a function of applied bias for different height of the asperity but fixed width (∼4.7 nm). (c) The field enhancement as function bias for different width but fixed height (8 nm).

shows the peak enhancement factor as a function of applied bias for asperities of different height and constant width (∼4.7 nm). The tallest asperity (8 nm high) produces an initial field that is 12 times that of a flat electrode, partly due to the effective reduction in film thickness (a factor of 1.7) but mostly due to the height and shape of the asperity. This initially remains constant and is determined by the electrode geometry only. However, the field enhancement begins to decrease for voltages above ∼0.5 V, which corresponds to the critical electric field (∼2.9 MV/cm) for enhanced defect generation. A similar effect is observed for asperities of different height, with the reduction in field enhancement occurring at different voltages but at the same peak field of ∼2.9 MV/cm. Clearly the generation and redistribution of defects acts to reduce the local field around the asperity and at high voltages the field enhancement approaches a value similar to that calculated from the local film thickness (i.e. between 1.1 and 1.7 for peaks of heights of 2 nm and 8 nm, respectively). Significantly, this saturation occurs at voltages much less than the breakdown voltage so that the latter is determined more by the field at saturation than by

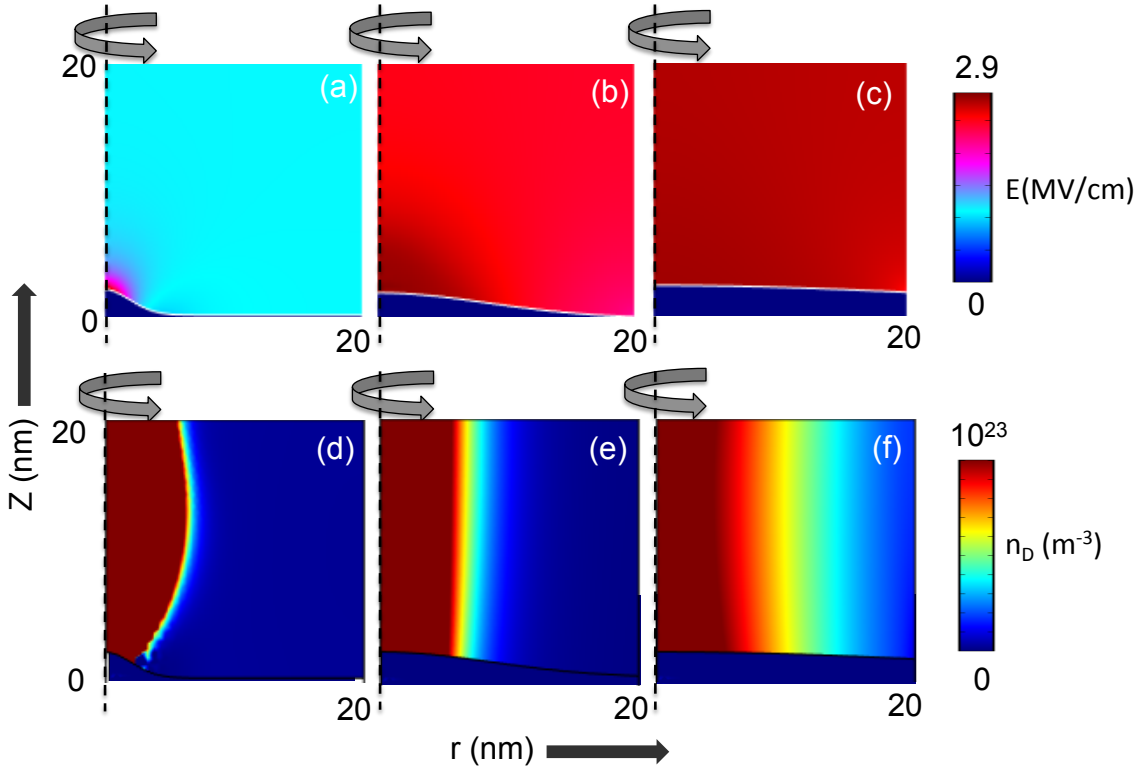

Figure 4.11 (a-c) Initial field distribution prior breakdown and (e-f) defect distribution at soft breakdown for different widths of asperity but same height.

the initial field enhancement. Fig. 4.10 (c) shows a similar effect as a function of asperity width for a constant asperity height of 8 nm. From these results we conclude that the electric field enhancement around electrode asperities is reduced by the generation and migration (drift and diffusion) of defects and that as a consequence the effect on dielectric breakdown is less than anticipated from geometric effects alone.

It is also worth noting that the diameter of conductive filaments increases with increasing width of the asperity and that this can have a direct impact on the dynamic evolution of the temperature and current in the filament. Fig. 4.11 shows the initial electric field distribution and filament shape after soft breakdown as a function of asperity width. For very sharp (small width) asperities the filament resistance can limit the current and thereby reduce the local temperature increase. As defect generation and migration are thermally activated this reduces the rate of filament evolution and can act to increase the forming voltage. Such effects are responsible for the small increase in forming voltage with decreasing asperity width (increasing sharpness) evident in Fig. 4.10(a). From Fig. 4.11(a-c), it is evident that

the effective volume of material subjected to enhancement is a function of the width of the asperity. For a wider asperity, defect generation is initiated over a broader volume and attracted toward the top electrode along electric field direction. This results a wider filament formation as shown in Fig. 4.11(d-f).

4.4. Conclusion

The surface roughness of electron-beam evaporated Pt electrodes was shown to have a strong dependence on film thickness, consistent with the differential growth rate of Pt grains. The effect of electrode roughness on the forming characteristics of Pt/Ti/HfO_2/Pt metal-insulator-metal resistive random access memory (ReRAM) structures was investigated. The electroforming voltage of HfO_2 films was found to decrease with increasing electrode roughness. However, any advantage afforded by this effect was compromised by a concomitant increase in the forming voltage dispersion and an increase in the failure rate of the devices. Finite element simulations of dielectric breakdown around an asperity provided considerable insight into the role of local electric field enhancement. The electrode's asperity geometry was found to have a significant effect on the electric field distribution, with field enhancements of more than an order of magnitude observed for high aspect ratio asperities. However, the peak field was shown to be moderated by the generation and redistribution of defects prior to dielectric breakdown. As a consequence the effect of field enhancement on dielectric breakdown is less than anticipated from geometric affects alone. Finally, it is suggested that the increase in device failure rate with increasing electrode roughness is consistent with an increase in film defect density and effective device area and that these effects contribute to the reduction in breakdown voltage.

CHAPTER 5

Effect of Current Confinement in Integrated Devices

5.1. Introduction

Resistive switching memory (ReRAM) in crossbar architectures faces sneak current problems, which lead to data reading errors. Integrating a selector element with each memory element can solve this problem [92]. However, threshold switching selector elements require relatively high operating currents compared to resistive switching memory devices, with typical currents to initiate to threshold switching in the range 1-10 mA, which are much higher than those of resistive switching (1-100 μA) [96, 97]. This limits the potential for integration as high currents can permanently damage the resistive memory element. Lower operating currents are therefore required for integration with memory devices. Strategies to realize low current operation are based on modified device designs that either reduce the active volume of the threshold switching material and maximise the local temperature rise for a given electric stress (e.g. 3D vertical structure has been used in Ref. [98]); or concentrate the electric-field and/or current in a specific region of the device in order to reach the transformation temperature at a lower current [154, 155]. The latter can be achieved by controlling the conductive filament size in the memory layer [155, 156]. The local electric field at the top of a filamentary conduction path in an adjacent dielectric layer can be

used to confine switching to the region around the filament. In this chapter, we have investigated the effect of residual and permanent filaments in integrated 1S1R structures.

5.2. Experiments

Bottom electrodes consisted of a 10 nm Ti wetting layer and a 150 nm Pt layer deposited on a thermally oxidized Si substrate by electron beam evaporation without breaking vacuum. For homogeneous 1S1M structures, Nb_2O_{5-y} (∼20 nm) and NbO_{2-x} (∼30 nm) layers were subsequently deposited by reactive sputter deposition, with the stoichiometry controlled by varying the argon to oxygen ratios in the plasma. The Ar : O_2 pressure ratio for Nb_2O_{5-y} and NbO_{2-x} are 18:2 and 19:1 respectively (described in Chapter 3). For heterogeneous structures, a 20 nm thick HfO_2 layer was first deposited on the bottom contact layer using atomic layer deposition (ALD). This was achieved by heating the sample to 200°C and exposing it to alternate pulses of tetrakis-(dymethylamido)-hafnium ($Hf(NMe_2)_4$) and H_2O vapor, with an N_2 purge between pulses. To complete the heterogeneous 1S1M structure an NbO_{2-x} layer was subsequently deposited on the HfO_2 layer using reactive sputter deposition, as described above. In principle the memory layer can be put above or below the selector layer but in this study the memory layer was deposited first to avoid unnecessary heating of the NbO_{2-x} layer during ALD of the HfO_2 layer. Finally, 50 nm Pt top contacts with diameters in the range 150-250 μm were deposited on 1S1M structures to complete the test devices. Pt/NbO_{2-x}/Pt (1S) and Pt/Nb_2O_{5-y}/Pt (1M) structures were also fabricated as reference samples.

5.3. Effect of Current Confinement

5.3.1. Effect of Residual Filament

Fig. 5.1(a) shows a schematic of the NbO_x-based 1S, 1M and 1S1M structures employed in this study, and subsequent panels [Fig. 5.1(b-d)] show the corresponding

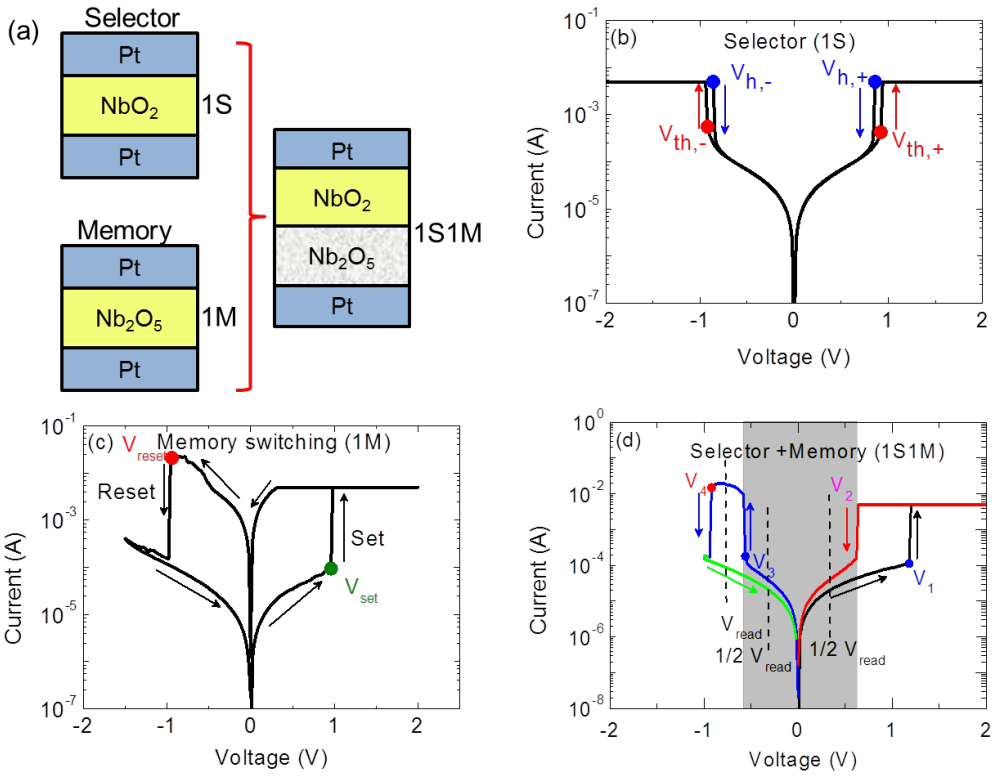

Figure 5.1 (a) Schematics of 1S, 1M and 1S1M devices. Typical current-voltage (I-V) curves of (b) NbO_{2-x}(1S), (c) Nb_2O_{5-y} (1M), (d) NbO_{2-x}/Nb_2O_{5-y}(1S1M) hybrid memory, along the arrows showing switching direction. Here all I-V curves have same set current compliance (5 mA).

current-voltage (I-V) characteristics of these devices. Initially, $Pt/NbO_{2-x}/Pt$ (1S) devices are in a high resistance state and require an electroforming step. Electroforming was performed by applying a positive bias to the top electrode with an instrumental compliance of 5 mA to avoid permanent damage to the device. I-V characteristics of the 1S device [Fig. 5.1(b)] show threshold switching behavior after an initial forming process. When a positive bias is applied, the NbO_{2-x} undergoes an IMT at a threshold voltage $V_{th,+}$ and the current increases rapidly to the compliance limit as the selector is turned "ON". When the applied bias is reduced to the hold voltage $V_{h,+}$, the layer reverts to the insulating state and the current suddenly decreases -the device is turned "OFF". Similar behavior is observed for negative voltage bias, i.e. the threshold I-V curve is symmetric with respect to applied voltage polarity and $V_{th,+} = V_{th,-}$, $V_{h,+} = V_{h,-}$.

Fig. 5.1(c) shows memory (1M) switching in the $Pt/Nb_2O_{5-y}/Pt$ device. This device also requires an electroforming voltage sweep that uses a compliance current (∼5

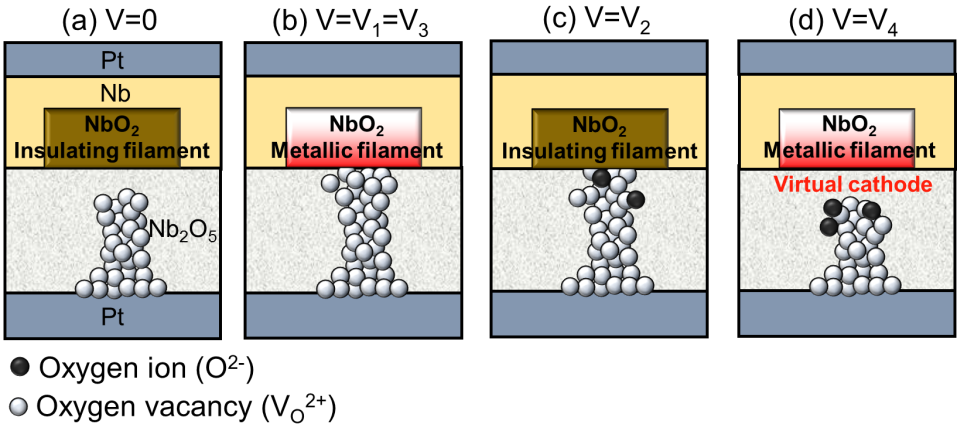

Figure 5.2 Schematic diagrams of operating mechanism of NbO_{2-x} /Nb_2O_{5-y} 1S1M hybrid switching: (a) initial state (S-off/M-OFF); (b) NbO_{2-x} filament undergoes an IMT transition at threshold voltage (S-ON/M-ON); (c) NbO_{2-x} filament goes back to insulating state at hold voltage (S-OFF/M-ON); (d) The oxygen vacancy filament in the Nb_2O_{5-y} layer ruptures during the RESET process (S-on/M-OFF).

mA) limit to protect it from irreversible breakdown. Once formed, the device was switched from low to high resistance by applying a negative bias (RESET process), and from high resistance to low resistance by applying a positive bias (SET process). This behavior is generally attributed to the rupture and repair of a filamentary conduction path caused by the drift and diffusion of defects (i.e. oxygen ions and vacancies) under the action of the applied field and local Joule heating respectively.

Finally, Fig. 5.1(d) shows the I-V characteristics of a hybrid 1S1M device, in which the NbO_{2-x} and Nb_2O_{5-y} layers are stacked. To clarify the physical basis of the hybrid device we refer to the I-V characteristics in Fig. 5.1(d), and the schematics in Fig. 5.2 which depict the evolution of the conductive filament and IMT during SET and RESET operations. Fig. 5.2(a) shows the device after an initial forming and RESET process. The forming process creates a conductive filament in the insulating Nb_2O_{5-y} layer via a soft-breakdown-like process. This requires a higher voltage than that employed for the SET/RESET operations and also induces the IMT in the neighboring NbO_{2-x} layer due to local Joule heating. A negative voltage sweep is then used to RESET the device, leaving it in the high resistance state depicted in Fig. 5.2(a). At this stage the NbO_{2-x} (1S) layer is in an insulating state ("OFF" state) and the Nb_2O_{5-y}(1M) layer is in a high-resistance state (HRS, "OFF" state) but with a vestigial filament traversing most of the layer, i.e. the "S-OFF/M-OFF"

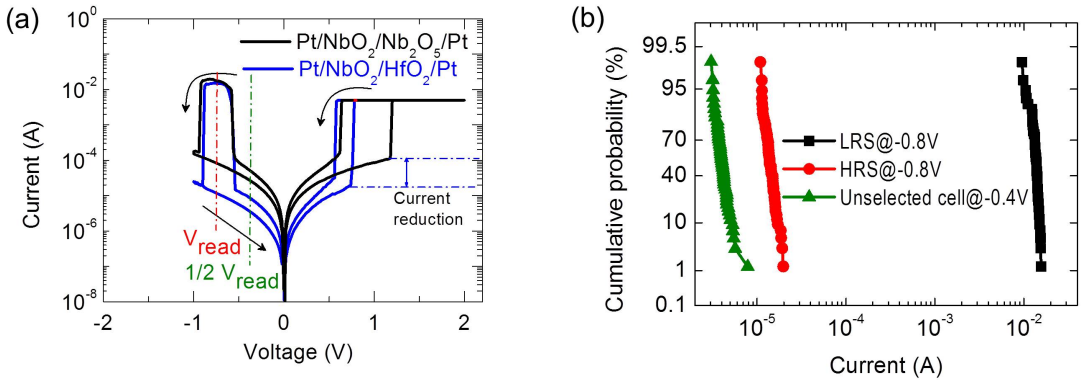

Figure 5.3 (a) Typical I-V characteristics of homogeneous NbO_{2-x}/Nb_2O_{5-y} and heterogeneous NbO_{2-x}/HfO_2 devices. The improved device properties such as current reduction, SET voltage reduction and higher ON/OFF ratio are obtained in NbO_{2-x}/HfO_2 devices. (b) Cumulative probability of LRS, HRS, and half read state of heterogeneous NbO_{2-x}/HfO_2 hybrid memory from the continuous DC switching cycles.

state of the hybrid device. This is the starting point for evaluation of the 1S1M response of the device.

As the voltage increases above the threshold value (V_1) [Fig. 5.1(d)], the Nb_2O_{5-y} layer undergoes a "SET" operation and induces an IMT in the adjacent NbO_{2-x} layer due to local Joule heating. As a consequence the current increases to the compliance limit. This corresponds to the "S-ON/M-ON" state of the hybrid 1S1M device [Fig 5.2(b)]. As the applied voltage is then reduced, the temperature of the NbO_{2-x} layer decreases, and at a threshold voltage V_2 [see Fig. 5.1(d)] it reverts to an insulation state while leaving the Nb_2O_{5-y} layer in the conductive "ON" state, i.e. the "S-OFF/M-ON" state of the hybrid device [Fig 5.2(c)]. During a subsequent negative sweep, the insulating NbO_{2-x} phase undergoes an IMT at the negative threshold voltage V_3 [see Fig 5.1(d)] due to local Joule heating while the resistive Nb_2O_{5-y} layer remains in its low resistance state, which corresponds to the "S-ON/M-ON" state of the hybrid device [Fig 5.2(b)]. As the negative voltage sweep is increased to V_4, the conductive filament in the Nb_2O_{5-y} (1M) layer is ruptured by the drift and diffusion of charged defects [Fig 5.2(d)] and it reverts to a HRS.

In one SET/RESET cycle the hybrid device therefore undergoes the following sequence: S-OFF/M-OFF →S-ON/M-ON → S-OFF/M-ON → S-ON/M-ON → S-ON/M-OFF → S-OFF/M-OFF, where the S-OFF/M-OFF and S-ON/M-ON can

Table 5.1 The parameters of the threshold voltages/currents, sneak current and R_{OFF}/R_{ON} ratio in in homogeneous $Pt/NbO_{2-x}/Nb_2O_{5-y}/Pt$ and heterogeneous $Pt/NbO_{2-x}/HfO_2/Pt$ devices.

Bias	Homo	Heter	Current	Homo	Heter
V_1	1.18 V	0.75 V	I_1	∼120 μA	∼20 μA
V_2	0.62 V	0.56 V	I_2	∼170 μA	∼32 μA
V_3	0.53 V	0.55 V	I_3	∼120 μA	∼15 μA
V_4	0.94 V	0.9 V	I_4	∼180 μA	∼20 μA
R_{OFF}/R_{ON} ratio	∼150	∼1100	I_{sneak} @0.4V	∼30 μA	4 μA

be recognized as logic "0" and "1" states. The read voltage V_{read} is usually chosen to lie between V_3 and V_4, where logic "0" and "1" states can be detected and the R_{OFF}/R_{ON} ratio calculated. For high-density cross-point memory applications a 1/2 V_{read} scheme is generally employed [157], in which V_{read} is applied to the addressed cell and 1/2 V_{read} is applied to non-addressed cells. As the selector remains in its high resistance state at voltages around 1/2 V_{read}, the sneak current is minimized.

We note that the threshold current ($I_1 \sim 100$ μA) at V_1 (∼1.2 V from Fig 5.1(d)) is less than that observed in the NbO_{2-x}/Nb_2O_{5-y} device (∼ 300 μA) reported by Mahne et al. [95]. The threshold current is related to the lowest operation current and sneak current level, where sneak current is defined as the current at 1/2 V_{read}.

To check the effect of the memory layer on the switching properties of the hybrid 1S1M devices, the sputtered Nb_2O_{5-y} memory layer was replaced by an ALD-deposited HfO_2 film. The 1S1M switching mechanisms in the homogeneous NbO_{2-x}/Nb_2O_{5-y} and heterogeneous NbO_{2-x}/HfO_2 structures are identical but the switching characteristics are modified. Fig. 5.3(a) compares the current-voltage characteristics of the NbO_{2-x}/Nb_2O_{5-y} and NbO_{2-x}/HfO_2 1S1M hybrid devices. Both devices were tested with the same set compliance current (∼5 mA) and have similar peak reset currents. However, the heterogeneous NbO_{2-x}/HfO_2 devices show significantly lower sneak current (∼4 μ A @ 0.4V) and a larger R_{OFF}/R_{ON} resistance ratio (about three orders of magnitude) than the comparable homogeneous NbO_{2-x}/Nb_2O_{5-y} structure. Table 5.1 summarizes the threshold voltages and currents for the homogeneous and heterogeneous structures.

As shown in Fig. 5.3(b) excellent uniformity in LRS, HRS and half-bias-read states

was also obtained in NbO_{2-x}/HfO_2 hybrid (1S1M) devices over 100 consecutive DC measurement cycles, which is important for high-density ReRAM cell integration. The DC endurance of NbO_{2-x}/HfO_2 hybrid devices was typically in the range of $10^2 - 10^3$ cycles. This could be increased to a much larger endurance (more than 10^6 cycles) in pulsed mode assuming that degradation is limited by the total dissipated energy. This might be expected for failure resulting from inter-diffusion between NbO_{2-x} and HfO_2 layers and/or oxygen out-diffusion during I-V cycling. Evidence for this mode of failure comes from the fact that device endurance can be improved by the use of active electrodes (e.g. W, TiN, Ti) that form an additional oxygen diffusion barrier at the electrode/NbO_{2-x} interface [18, 158].

The better performance of the HfO_2 1M film compared to the Nb_2O_{5-y} 1M film is of particular interest and can result from several factors. One possibility is that a thinner conductive filament is formed in the high-quality ALD-deposited HfO_2 dielectric oxide memory layer as an indirect consequence of its higher resistance which acts to reduce the effective compliance current during the initial forming or SET/RESET processes. Another is that local Joule heating of the NbO_{2-x} 1S layer is influenced by the thermal and electrical conductivity of the 1M layer, which differs between HfO_2 and Nb_2O_{5-y}.

5.3.2. Effect of Permanent Filament

Fig. 5.4(a) shows schematic of single layer and bilayer selectors. In a single the threshold-switching layer is NbO_x, whereas in a bilayer selector (NbO_{2-x}/Nb_2O_{5-y} or NbO_{2-x}/HfO_2) a permanent filament in the dielectric is created to confine the electric current in the filamentary region. As a result the threshold switching volume is reduced. Threshold switching in the bilayer device is achieved by continuing DC switching cycles by setting a compliance current limit for both polarities (preventing the device from resetting during negative cycles).

Fig. 5.4(b) shows a current-voltage (I-V) curve for a Pt/NbO_{2-x}/Pt device, which demonstrates typical threshold switching behavior. As the applied voltage is increased

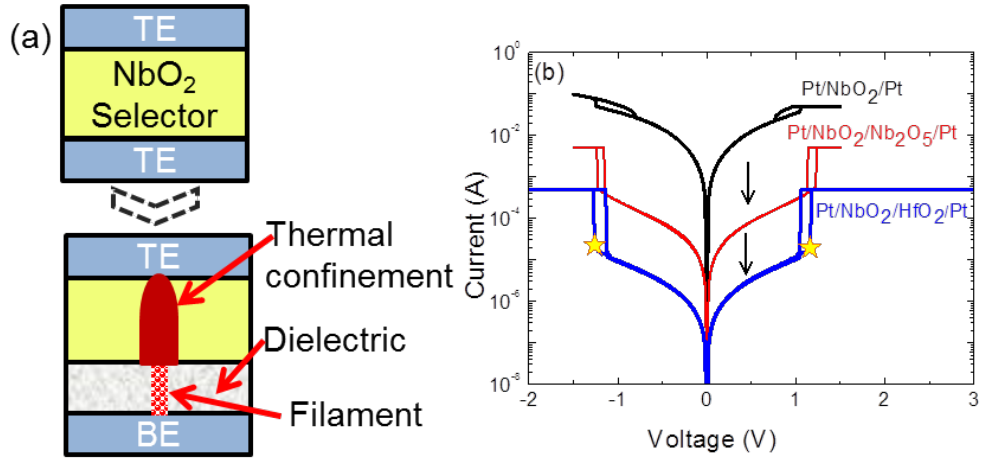

Figure 5.4 (a) Strategic schematic of a dielectric "control" layer with a conductive filament on textured BE to decrease the threshold currents (I_{th}). A permanent filament in the memory layer is created to localized the current in the filamentary region. (b) Reduction in Ith using strategy (a) was demonstrated as shown by typical I-V characteristics for three devices: $Pt/NbO_{2-x}/Pt$, NbO_{2-x}/Nb_2O_{5-y} and NbO_{2-x}/HfO_2. The stars show the decreased Ith ~20 μA in NbO_{2-x}/HfO_2.

from 0 to 2 V the current is observed to increase discontinuously, with a sudden rise evident at ~1.0 V, called the threshold voltage (V_{th}). This corresponds to the onset of the IMT and the device remains in this "ON" state as the voltage is increased above the threshold value. The maximum current in the "ON" state is limited by instrumental compliance to avoid device damage. As the applied voltage is reduced from 2 to 0 V, the current undergoes a sudden reduction at ~0.8 V as the film reverts to the insulating state, referred to as the "OFF" state. The electrical properties of NbO_{2-x} therefore exhibit volatile switching between insulating and metallic states. Similar behavior is also observed for negative voltage sweeps, consistent with the nonpolar nature of a thermally induced IMT. It is important to note, however, that the threshold current (I_{th}) of ~36 mA, defined at the corresponding V_{th}, is too large to be useful as the selector in cross-point memory arrays.

Also shown in Fig. 5.5(a-b) are I-V curves for devices containing intermediate Nb_2O_{5-y} and HfO_2 layers. Inserting a sputtered Nb_2O_{5-y} layer reduces the threshold current by almost two orders of magnitude, to ~560 μA for similar V_{th} (~1.2 V), dramatically improving the device selectivity ("ON/OFF" current ratio). This cannot be explained simply by treating the Nb_2O_{5-y} layer as a constant series resistor. Instead, it results from the formation of a permanent conductive filament in the Nb_2O_{5-y}

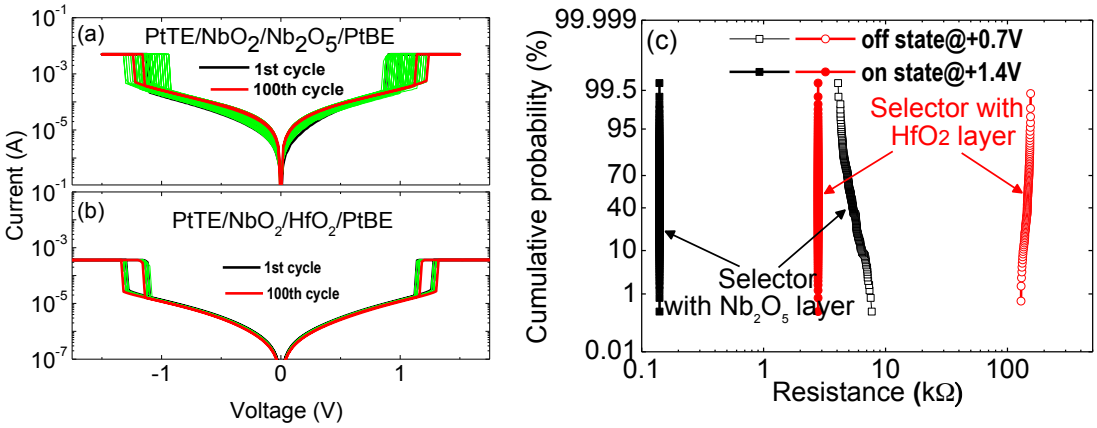

Figure 5.5 (a) I-V characteristics for NbO_2 selector with different dielectric layer, obtained from the continuous threshold switching of 100 cycles. (b) The corresponding cumulative probability distributions of ON state (solid symbol) and OFF state (open symbol) for two devices: $Pt/NbO_{2-x}/Nb_2O_{5-y}/Pt$ (square) and $Pt/NbO_{2-x}/HfO_2/P$ (circle).

dielectric layer, which confines conduction around the filament region. Inserting an HfO_2 layer instead of the Nb_2O_{5-y} layer further reduces I_{th} to $\sim$20 μA [Fig. 5.5(c)]. Such a reduction is particularly significant as it is close to that realized in nanoscale (ϕ $\sim$10 nm) 3D vertical ReRAM (I_{th} is $\sim$10 μA) [18].

As shown in Fig. 5.5(a) and (b), good uniformity in volatile threshold switching was obtained for 100 consecutive DC measurements for both $Pt/NbO_{2-x}/Nb_2O_{5-y}/Pt$ and $Pt/NbO_{2-x}/HfO_2/Pt$ devices. Furthermore, no significant change in V_{th} was observed even after 100 switching cycles for $Pt/NbO_{2-x}/HfO_2/Pt$ devices [Fig. 5.5(a)], which is important for selector device applications.

5.4. Numerical Simulations

5.4.1. Model Physics

To study how key parameters affect the threshold voltages/currents in 1S1M hybrid memory devices, numerical simulations were performed for the memory ON state at V_2 and V_3. The same effect is expected for the memory OFF state at V_1 and V_4, where a broken filament exists [97], the only difference being a larger memory OFF resistance. The simulations assume the existence of a stable conductive filament in

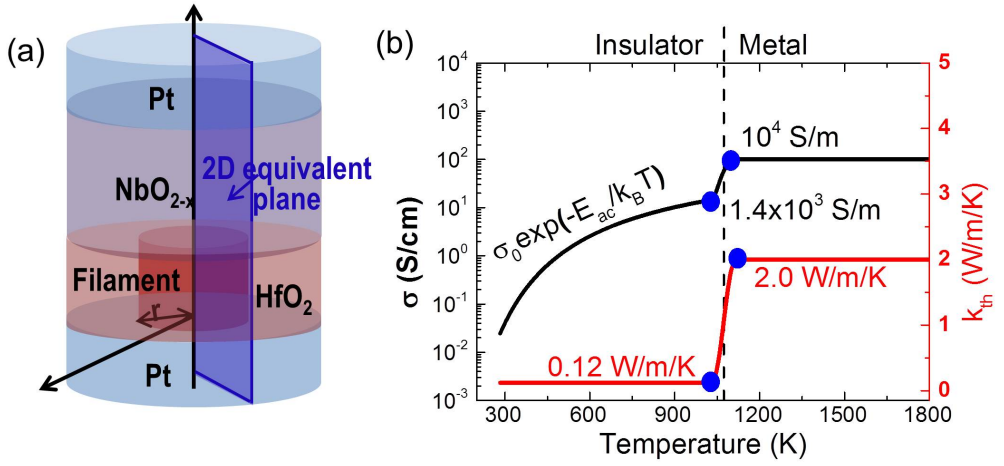

Figure 5.6 (a) Simulated geometry used in calculation. (b) Assumed electrical conductivity σ, and thermal conductivity k_{th} as a function of temperature T.

Table 5.2 Material parameters for electrode (Pt) and memory layers (Nb_2O_5 and HfO_2).

Symbol	Quantity	Pt	Nb_2O_5	HfO_2
σ (S/m)	Electrical conductivity	10^7	-	-
σ_0 (S/m)	Pre-exponential factor of electrical conductivity	-	$\sim 10^{-4}$	$\sim 10^{-6}$
k (W/m/k)	Thermal conductivity	72	4.6	1
ρ (kg/m^3)	Density	21450	4600	9680
C_p (J/kgK)	Specific heat	133	498	287

the memory oxide layer, and calculate the current and temperature distributions as a function of applied voltage. The threshold switching in the 1S layer is modelled by temperature dependent thermal and electrical conductivities that vary between those of the insulating and metallic phases over a temperature range of ~100 K, centred at the nominal transition temperature of 1073 K. These parameters were chosen to match published data on the IMT in NbO_2 [159].

Simulations were performed with the COMSOL Multiphysics code, assuming a 2D axially symmetric device geometry based on the Pt/NbO_{2-x}/HfO_2/Pt structure as shown in Fig. 5.6 (a). The electric field and current distributions were calculated from the Poisson equation:

$$\nabla \cdot \sigma \nabla \psi = 0 \tag{5.1}$$

where σ and ψ are the conductivity and electric potential, respectively. This equation accounts for the perturbation of electric field due to the stable conductive filament.

The electrical conductivity (σ) of the NbO_{2-x} insulating phase is assumed to take

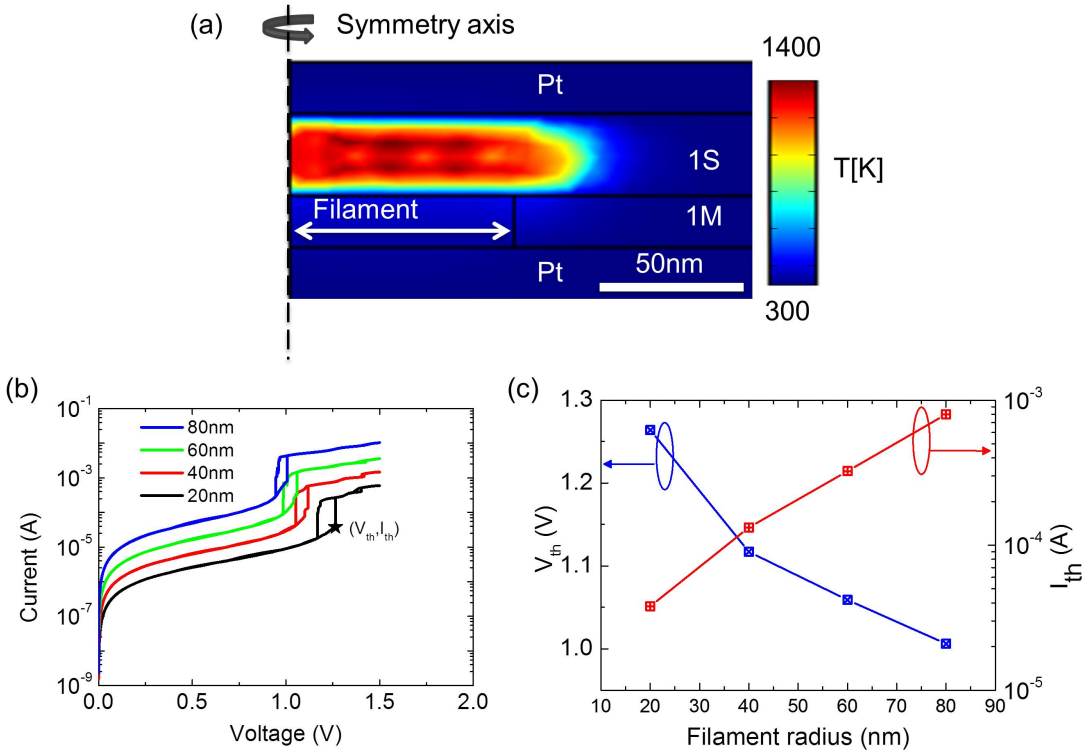

Figure 5.7 (a) Calculated expanding temperature distributions where red color region in NbO_2(1S) layer represents the high-temperature metallic phases during IMT process. (b) Calculated I-V characteristics for 1S1M with different filament size in the memory layer. These I-V curves of selector "ON" state correspond to the read process, after the positive set, not equal to the set process. (c) These results show that thermal confinement can produce significant reductions in threshold current (I_{th}).

the form of an Arrhenius equation $\sigma_{\text{insulator}} = \sigma_0 \exp(-E_A C/k_B T)$, and that of the metallic phase is assumed to have a constant value $\sigma_{\text{metal}} = 1 \times 10^4\ \Omega^{-1}\text{m}^{-1}$ as depicted in Fig. 5.6(b). Here σ_0 is a pre-exponential factor, and E_{AC} is the carrier activation energy. The temperature distribution in the device was obtained by solving the Fourier heat equation and the Poisson equation self-consistently using a finite element model. The Fourier heat equation takes the form:

$$\rho C_p \frac{\partial T}{\partial t} - \nabla \cdot k_{\text{thermal}} \nabla T = Q \tag{5.2}$$

where ρ is the mass density, C_p is the specific heat, k_{thermal} is the thermal conductivity and $Q = |\sigma \nabla \psi|^2$ is the heat flux density due to the electric current (i.e. Joule heating). The k_{thermal} values for the NbO_{2-x} film also depend on its state. Here we used $k_{\text{insulator}} = 0.12\,\text{Wm}^{-1}\text{K}^{-1}$ and $k_{\text{metal}} = 2.0\,\text{Wm}^{-1}\text{K}^{-1}$ [Fig. 5.6(b)]. Other materials (electrode and memory layers) parameters used in the simulations are given

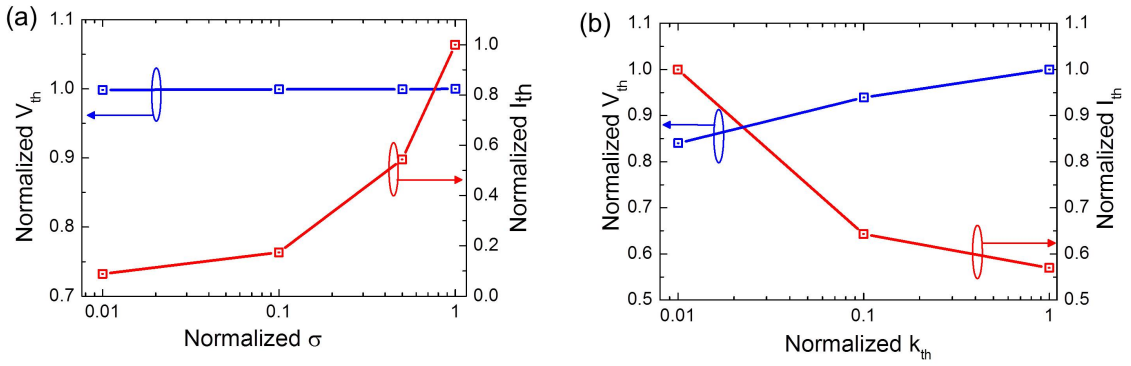

Figure 5.8 Calculated threshold current (I_{th}) and voltage (V_{th}) as function of (a) electrical and (b) thermal conductivity of HfO_2 layer. These simulations are considering a filament size of 20nm in the memory layer.

in Table 5.2 [145,160,161]. The electrical and thermal conductivities of the permanent filament were assumed to be those of metallic Hf, and those of the remaining HfO_2 layer were varied from 0.1 to 10 times the bulk value to test their effect on the device characteristics. Note that the electrical and thermal conductivities of ALD HfO_2 films are expected to be lower those of sputtered Nb_2O_{5-y} films, since the sputtered films contain higher local concentrations of oxygen vacancies.

5.4.2. Effect of Filament Size

Fig. 5.7 shows finite element simulations for the IMT as a function of filament radius in the 1M oxide layer. The device geometry is shown in Fig. 5.7(a), including the expanding IMT phase-change region (at a voltage higher than V_{th}) [49]. The corresponding I-V characteristics are shown in Fig. 5.7(b) and clearly show that the threshold current decreases with decreasing filament radius, a dependence shown more explicitly in Fig. 5.7(c). This reduction occurs because the IMT transition in the NbO_{2-x} layer is localized at the top of the filament in the memory oxide layer. As the filament size decreases, heating is confined to a smaller volume of NbO_{2-x} and it consequently reaches the IMT temperature at lower current. The smaller volume of the IMT region also increases its resistance, leading to a slight increase in threshold voltage as the filament radius is reduced.

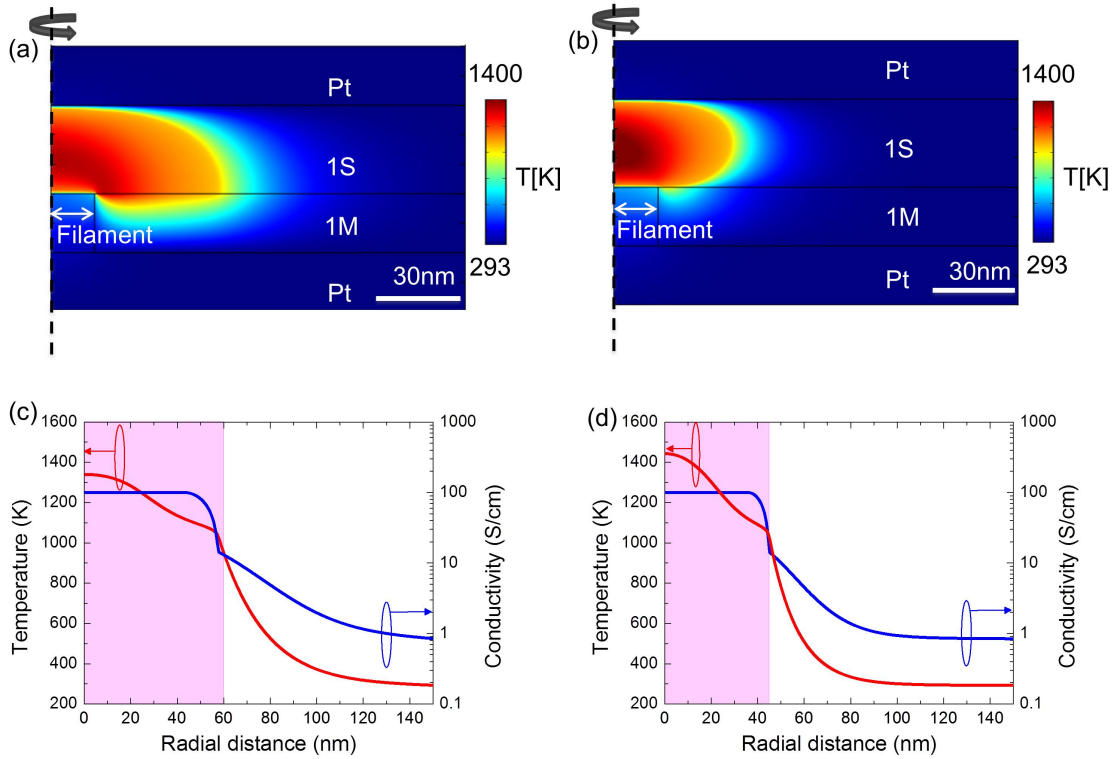

Figure 5.9 2D temperature distribution at threshold voltage as a function of normalized thermal conductivity of the dielectric (a) 0.01 (b) 1. The corresponding temperature and electrical conductivity profiles at middle of the NbO_2 (1S) layer are plotted in (c) and (d), respectively. For a lower thermal conductivity (normalized value 0.01) IMT region is larger (panel c) whereas for higher value of thermal conductivity IMT region is smaller (panel d) due to faster heat dissipation.

5.4.3. Effect of Electrical and Thermal Conductivity

The effects of electrical and thermal conductivity on the threshold voltage and current are demonstrated in Fig. 5.8, where the V_{th} and I_{th} are defined in Fig. 5.7(b). Increasing the electrical conductivity of the memory layer is observed to increase the threshold current, as shown in Fig. 5.8(a). Here it is important to note that the threshold current, I_{th}, represents the total device current and includes contributions from the conductive filament and an increasing contribution from the remaining film as its conductivity is increased. In contrast, the threshold voltage, V_{th}, remains almost constant [Fig. 5.8(a)]. This threshold current can therefore be reduced by using a high resistivity memory layer, and by reducing the device area.

The effect of thermal conductivity on I_{th} is shown in Fig. 5.8(b), clearly demonstrating that the threshold current for the IMT decreases with increasing thermal

conductivity of the memory layer. This initially seems counter-intuitive as one might expect the threshold current to increase due to additional heat loss through the thermally conductive 1M layer. The explanation is evident from the data in Fig. 5.8 which shows the temperature distribution in the structure for two different values of 1M thermal conductivity. The increase in thermal conductivity reduces the thermal resistance of the layer and increases heat loss from the NbO_{2-x} 1S layer. This confines the temperature increase and the current to a smaller volume of NbO_{2-x} and as a consequence the IMT is achieved at a lower threshold current. This is clearly evident from a comparison of the 2D temperature plots in Fig. 5.9(a-b) and from the radial distributions of the temperature and electrical conductivity shown in Fig. 5.9(c) and (d). The threshold voltage shows a slight increase with increasing thermal conductivity due to an increase in the resistance of the smaller NbO_{2-x} IMT volume [see Fig. 5.8(b)]. From these simulations it is clear that the threshold current for the IMT in a 1S1M hybrid structure depends on the filament diameter in the neighboring 1M layer and on the thermal and electrical conductivity of this layer, with the dominant effect being the size of the conductive filament.

5.5. Effect on Readout Margin

The reduction in threshold/sneak current dramatically improves cell selectivity and reduces the write/erase power. Therefore, a larger array size can be realized for the NbO_{2-x}/HfO_2 hybrid memory. To confirm the suitability of these devices for high-density cross-point ($4F^2$) memory applications the readout margin can be estimated for different array sizes using measured device characteristics as shown in Fig 5.10. We estimate the readout margin for the 1S1M hybrid structure. This depends on the resistance window, the ON- and OFF-voltages in the memory device, and the threshold- and hold-voltages in the selector device. To demonstrate the effect of low current on crossbar integration, the simplified equivalent circuit for a crossbar array is shown in Fig. 5.10(a). However, as the top electrode connects all the cells in a row to each other, and all cells in a column are connected to each other by the bottom electrode, the hybrid device can suffer from sneak paths, as illustrated in Fig. 5.10(a).

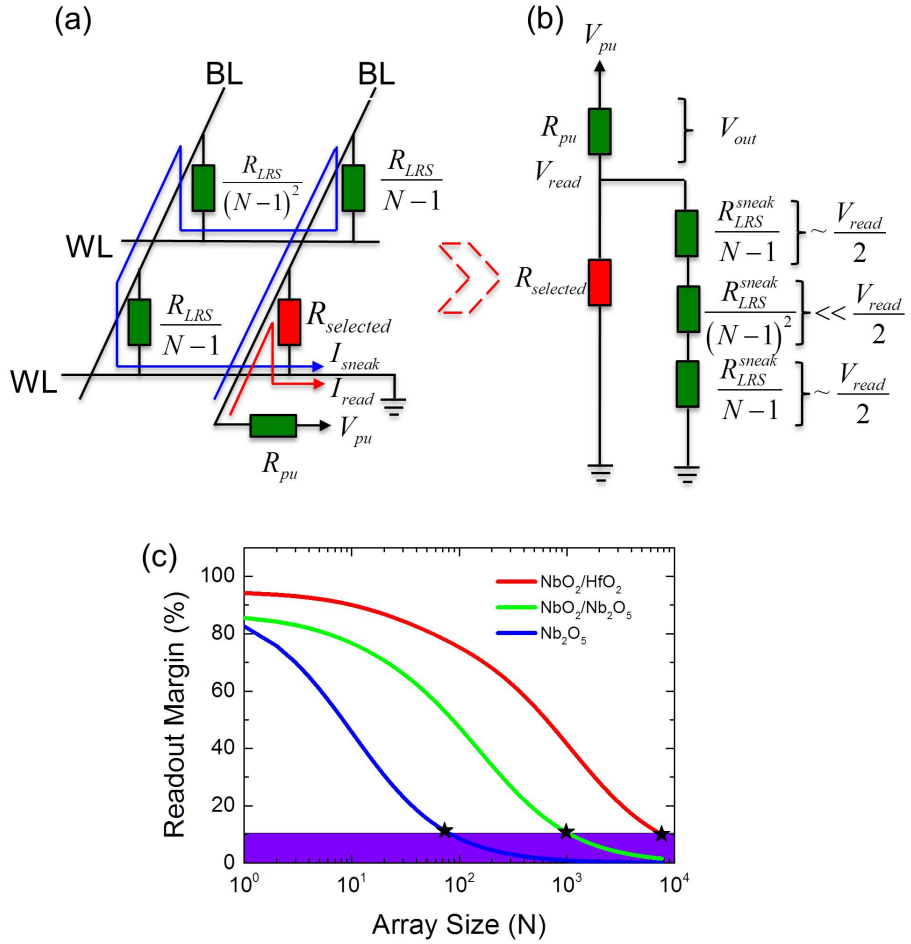

Figure 5.10 (a) Schematic of N×N crossbar array of ReRAM and (b) equivalent circuit of an N × N crossbar array for the one bit-line pull-up read scheme. Only the addressed element of the crossbar array is in the HRS (red), all surrounding elements are in the LRS (green). (c) Read margin $\Delta V/V_{pu}$ as a function of N in various crossbar configurations.

When a reading voltage (V_{read}) is applied to the selected bit-line, the voltage across the pull-up resistor (V_{out}) can be used to distinguish between the HRS and the LRS in the selected bit. Though the current flows through the selected bit (I_{select}), a sneak current flows through unselected bits (I_{sneak}). Thus, V_{out} is dependent on I_{sneak}. Using various circuit transformations, this assumption leads to a simple equivalent circuit template for the ReRAM circuit, as shown in Fig. 5.10(b). The read margin (ΔV_{out}) normalized to pull-up voltage (V_{pu}) [Fig. 5.10(c)] can then be calculated by solving the Kirchhoff equation with these parameters:

$$\frac{\Delta V_{out}}{V_{pu}} = \frac{R_{pu}}{\left[R_{LRS}^{sneak} \parallel \left[\frac{2R_{LRS}^{sneak}}{N-1} + \frac{R_{LRS}^{sneak}}{(N-1)^2}\right] + R_{pu}\right]} - \frac{R_{pu}}{\left[R_{HRS}^{sneak} \parallel \left[\frac{2R_{LRS}^{sneak}}{N-1} + \frac{R_{LRS}^{sneak}}{(N-1)^2}\right] + R_{pu}\right]} \tag{5.3}$$

The read margin decreases when the crossbar-line number (N) increases for both 1M and 1S1M devices. Using the superposition theory [162], the maximum values of N with at least 10% read margin for our 1M and 1S1M devices is calculated as a function of the number of words in the ideal cross-point array [Fig. 5.10(c)]. The memory density is estimated to be $\sim 10^6(10^3 \times 10^3, m = n)$ in NbO_{2-x}/Nb_2O_{5-y} devices. Further increasing the R_{HRS}/R_{LRS} ratio and suppressing the LRS current at $1/2\,V_{read}$ of unselected cells in NbO_{2-x}/HfO_2device substantially increases the memory density to $\sim 10^8(10^4 \times 10^4, m = n)$. This demonstrates that the anti-crosstalk properties of the NbO_{2-x}/HfO_2-based 1S1M devices can increase the crossbar array size substantially. Significantly, the values obtained for these micro-scale devices ($\sim 150\ \mu$m) are similar to those realized in nanoscale ($\sim$10 μm) 3D vertical ReRAM [18], consistent with the filamentary nature of the switching elements.

5.6. Conclusion

The performance of homogeneous $NbO_{2-x}/Nb_2O_{5-y}$and heterogeneous NbO_{2-x}/HfO_2 1S1M hybrid devices have been compared and it has been shown that the existence of a filamentary conduction path in the memory layer can produce a significant reduction in threshold current. The threshold current was also shown to be much lower for a HfO_2 memory layer than for a Nb_2O_{5-y} memory layer. Finite element modeling of the hybrid devices showed that this was likely due to greater current confinement in the HfO_2 layer as a result of a smaller diameter filament forming in this material. The electrical and thermal conductivities of the 1M layer were also found to affect the threshold current of the device but to a lesser effect. These concepts have so far only been tested on large-scale device structures and further work is proposed to test their scalability and to explore alternative patterning approaches.

CHAPTER 6

Self-assembly of an NbO_2 interlayer

6.1. Introduction

The threshold switching response is of particular interest as a potential selector element (1S) in ReRAM arrays where it can be used to reduce current sneak paths [18, 163]. Sneak paths arise from the fact that resistive memory devices pass current in either direction when in the "on" (low resistance) state and can thereby give rise to unintended addressing of memory elements via indirect addressing routes [164]. The integration of a threshold switch in series with the ReRAM memory element acts to limit the current at voltages below the threshold value and can enable unambiguous memory addressing in high-density memory arrays [18, 98]. In its simplest form an integrated selector-memory (1S1M) element can be fabricated as a transition metal oxide bilayer comprised of resistive switching and threshold switching oxide layers [95, 97]. In Chapter 5, we demonstrated the efficacy of such 1S1M structures in which the selector element was based on threshold switching in $NbO_{2-\delta}$.

One of the problems with this approach is that the selector element typically requires a high forming current ($\sim$5 mA) to initiate the threshold switching response, and because the memory element is necessarily subjected to the same current as a result

it is typically formed in a very low resistance state. As a consequence, the memory element requires a large initial reset current and often exhibits unipolar operation (thermally driven) with a large on/off resistance ratio. This does not preclude subsequent bipolar operation but it can directly affect device uniformity and reliability. Clearly alternative approaches are required to achieve reliable low-power, bipolar memory operation in integrated 1S1M structures.

In this chapter we report configurable switching modes in a Pt/Nb/HfO_2/Pt device structure as a function of the set compliance current, and show that these changes (bipolar 1M to 1S1M and 1S) are consistent with the formation of an $NbO_{2-\delta}$ interlayer at the Nb/HfO_2 interface, the extent of which is controlled by the compliance current. The role of an active $NbO_{2-\delta}$ interlayer is supported by a physics based model which reproduces the experimental reset response of the proposed 1S1M structure.

6.2. Experiments

The test structures employed in this study consisted of simple metal-insulator-metal structures of the form: Pt/Nb/HfO_2/Pt as shown in Fig. 6.1(a). Ti (10 nm) and Pt (25 nm) bottom contact layers were deposited onto an oxidized Si wafer (150 nm SiO2/Si) by electron-beam evaporation. A 20 nm HfO_2 layer was subsequently deposited on the electrode by atomic layer deposition. This involved heating the substrates to 200^o C and exposing them to alternating pulses of pure tetrakis-(dymethylamido)-hafnium ($Hf(NMe_2)_4$) and H_2O vapor, with N_2 purge of the reaction chamber between pulses. The top electrode, consisting of 70 nm Nb and 10 nm Pt layers, was then deposited by dc magnetron sputtering. The top contact layers were deposited through a shadow mask to define 100 μm diameter contact pads. The final layer structure is shown in Fig. 6.1(b), which shows a cross-sectional transmission electron microscope (XTEM) image of the fabricated sample.

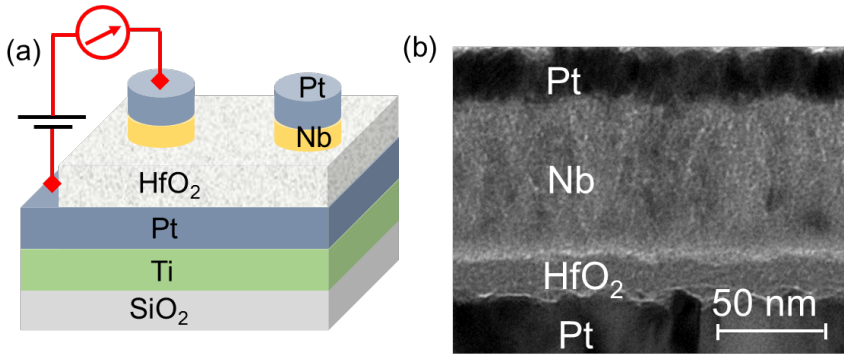

Figure 6.1 (a) Schematic and (b) XTEM image of the fabricated Pt/Nb/HfO2/Pt structure ReRAM.

6.3. Switching Behaviour of Nb/HfO_2/Pt

As-fabricated devices were highly insulating and required an electroforming process prior to switching. This was achieved by applying a positive bias to the top electrode (bottom electrode grounded) and increasing the voltage until a sudden increase in current was observed. An instrumental compliance current of 10 μA and a series resistor (10 kΩ) were used to avoid permanent damage (hard breakdown) of the dielectric due to excessive Joule heating [Fig. 6.2(a)]. The cummulative probability (Weibull distribution) of forming voltage is also presented in Fig. 6.2 (b). After electroforming, the devices were reset into a high resistance state using a negative voltage sweep from 0 V to -1.5 V. I-V switching characteristics were then measured using successive positive and negative voltage sweeps. A current compliance limit was used during set operations (positive voltage sweep) and during threshold switching operations (both positive and negative voltage sweeps). Three distinct current-voltage (I-V) responses were observed depending on the compliance current employed, as illustrated in Fig. 6.3.

For a SET compliance of $\sim$100 μA devices exhibited bipolar resistive switching [Fig. 6.3(a)] with excellent switching characteristics. The bipolar switching behavior can be understood in terms of established models of resistive switching [165]; i.e. during electroforming a filamentary HfO_{2-x} conduction path is created in the stoichiometric HfO_2 layer and oxygen ions are transported to the Nb-HfO_2 interface.

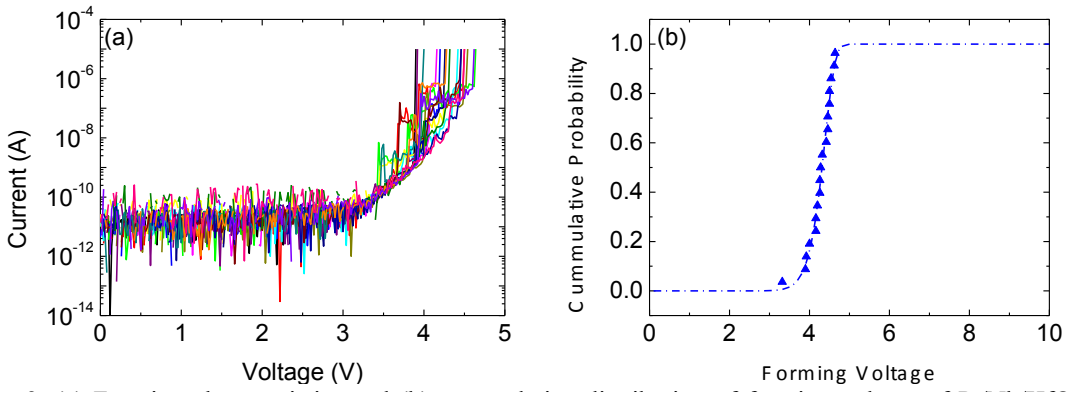

Figure 6.2 (a) Forming characteristics for $Nb/HfO_2/Pt$ devices and (b) cumulative probability distribution of forming voltage of $Pt/Nb/HfO_2/Pt$ device structure with a 10 kΩ resistor in series (blue curve represents a fit of the Weibull distribution).

Switching is then controlled by the opening and closing of a tunnelling gap in the filament due to field-induced transport of oxygen ions at the interface and devices exhibit bipolar resistive switching as shown in Fig. 6.3(a). While the low compliance current was maintained ($\leq$ 100 μA in the present case), these devices continued to exhibit stable bipolar operation suggesting that oxygen transport is conservative (i.e. there is no net loss or gain).

When the compliance current was subsequently increased to ~500 μA (with a -2 V, +2 V voltage sweep) the devices transitioned to a new mode of operation and after repeated sweeps (10-20 cycles) exhibited stable 1S1M behavior, as shown in Fig. 6.3(b). It is important to note that the devices survived a few tens of cycles in an ideal 1S1M switching mode then stabilize into a highly nonlinear switching mode. Comparison with the response of related NbO_2-based 1S and 1S1M structures (as discussed in the Chapater 5) suggests that the 1S response results from threshold switching in an $NbO_{2-\delta}$ interlayer. The formation of such a layer is not unreasonable as the amount of oxygen transported to the anode/oxide interface is expected to increase with increasing compliance current, as is evident from the formation of oxygen bubbles at the interface when inert electrode metals (e.g. Pt) and high compliance currents are used. The higher current is also expected to generate higher temperature as a result of Joule heating. This local increase in temperature is expected to enhance ion transport and interfacial reactions to form a $NbO_{2-\delta}$ region. On this basis the 1S1M switching characteristics would result from a combination

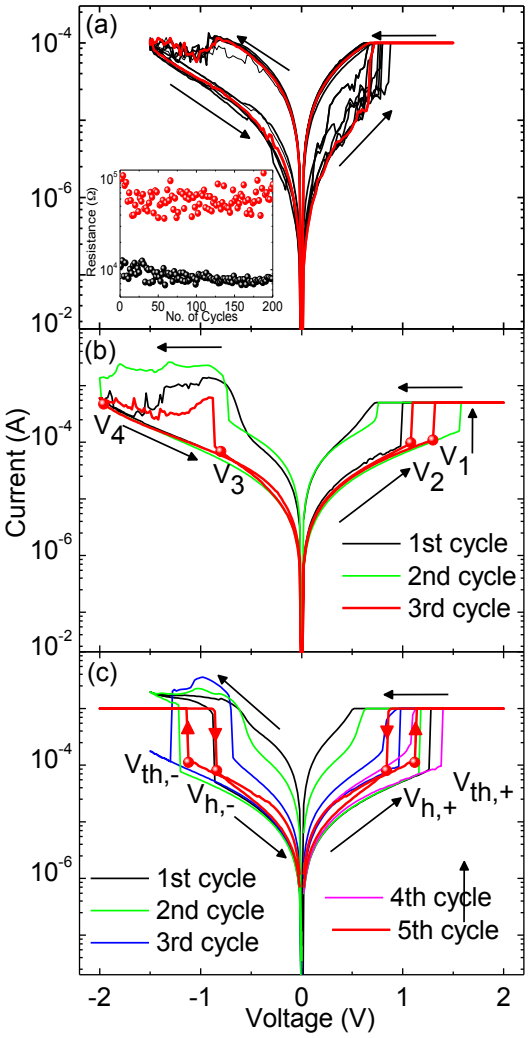

Figure 6.3 (a) Typical bipolar current-voltage (I-V) curves during the SET/RESET process with the arrows showing switching direction. Inset is the DC endurance for 200 cycles. (b) Transition from bipolar to 1S1M switching mode in the same device at ∼500 μA. Negative cycle contains components of threshold and memory switching. (c) Nonpolar/unipolar to threshold switching transitions in the same device at higher compliance (∼1 mA).

of threshold switching in the $NbO_{2-\delta}$ layer and bipolar resistive switching in the HfO_{2-x} layer, as observed in Fig. 6.3(b). During the positive cycle, as the voltage is increased to the threshold value V_1 the filament in the memory layer reforms (sets) and simultaneously induces the threshold switching in the NbO_2 due to Joule heating. As the applied voltage is reduced the NbO_2 volume cools and reverts to its insulating state. This results in a reduction in current at V_2 as the selector turns "off" but the memory remains in a "LRS" as shown Fig. 6.3(b). During a subsequent reset operation (i.e. negative bias) the temperature of the $NbO_{2-\delta}$ volume rises again due to Joule heating and this induced threshold switching at V_3. At the end of the sweep at bias V_4 the selector remains "on" and the memory layer is in a "HRS" (further

details are presented in the modelling section).

When the compliance current is further increased to 1 mA the device transitions to a threshold switching mode, and after five cycles [red curve in Fig. 6.3(c)] exhibits symmetric threshold switching behavior characteristic of NbO_2, as discussed above. It is noteworthy that during the first few cycles at this higher compliance the device exhibits transitionary nonpolar/unipolar resistive switching, consistent with the development of a lower resistance filament in the HfO_2 layer. This is expected as a consequence of additional O-ion transport from the filament to the $NbO_{2-\delta}$ layer, and as the number of switching cycles increases the conducting filament in the HfO_{2-x} layer becomes more stable and finally acts as a permanent filament and virtual electrode [166]. The resulting active device structure has the form Nb/$NbO_{2-\delta}$/metallic-HfO_{2-x} and exhibits symmetric threshold switching. The $NbO_{2-\delta}$ undergoes threshold switching at a voltage exhibits IMT at threshold voltage ($V_{th+} = V_{th+}$) and reverts to an insulating state at hold voltage ($V_{h+} = V_{h-}$) when bias direction is reversed. The response of the device is then controlled by the $NbO_{2-\delta}$ layer.

6.4. Pt/Nb/NbO_2/HfO_2/Pt 1S1M device

It is clear from the above discussion that bipolar switching is favoured at low compliance currents and threshold switching is dominant at high compliance currents, with 1S1M behavior observed at moderate compliance currents. It has been proposed that these responses originate from the development of an NbO_δ/NbO_2 inter-layer at the Nb/HfO_2 interface during repeated I-V cycling at a given compliance current. It is known that Nb has an oxygen (O_2) getter nature, and the Gibbs free energies of formation for niobium oxides are -921 kJ/mole (Nb_2O_5), -771 kJ/mole (NbO_2), -416 kJ/mole (NbO) whereas for Hf is -1010 kJ/mol at 300 K [167, 168]. The possible interface reactions between Nb and HfO_2 can be describe as

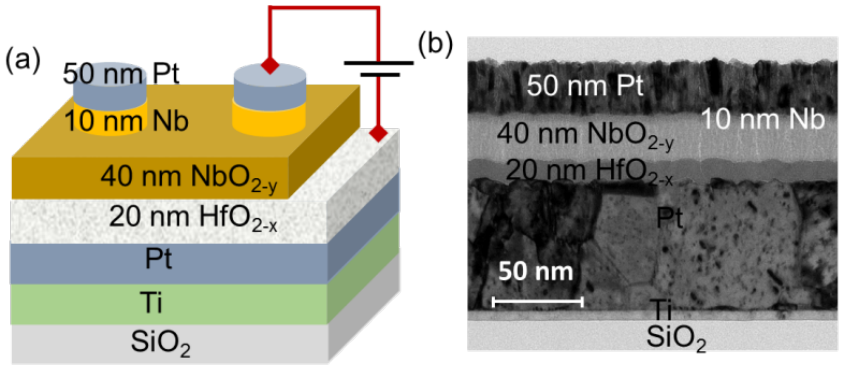

Figure 6.4 (a) Schematic of the Pt/Nb/NbO_2/HfO_2/Pt 1S1M device structure and (b) a cross-sectional transmission electron microscopy image of the same device structure.

$$4\mathrm{Nb} + 5\mathrm{HfO_2} \rightarrow 2\mathrm{Nb_2O_5} + 5\mathrm{Hf} \quad \Delta\mathrm{G} = 3208\,\mathrm{kJ/mol} \tag{6.1}$$

$$\mathrm{Nb} + \mathrm{HfO_2} \rightarrow \mathrm{NbO_2} + \mathrm{Hf}, \quad \Delta\mathrm{G} = 239\,\mathrm{kJ/mol} \tag{6.2}$$

$$2\mathrm{Nb} + \mathrm{HfO_2} \rightarrow 2\mathrm{NbO} + \mathrm{Hf}, \quad \Delta\mathrm{G} = 178\,\mathrm{kJ/mol} \tag{6.3}$$

Since $\Delta G > 0$, reactions can not proceeds spontaneously; thus, oxides of Nb cannot present at the Nb-HfO_2 interface.

To test this hypothesis, further measurements were performed on Pt/Nb/$NbO_{2-\delta}$/HfO_{2-x}/Pt devices, where the $NbO_{2-\delta}$ layer is incorporated directly during reactive sputter deposition as shown in Fig. 6.4. In this case the $NbO_{2-\delta}$ layer is expected to exhibit volatile threshold switching and act as the selector element, whilee the HfO_{2-x} layer is expected to exhibit nonvolatile resistive switching and act as the memory element. $NbO_{2-\delta}$ (40 nm) layer was deposited by reactive sputtering with argon to oxygen mass flow ratio 18.5/1.5 sccm at a constant total pressure of 4 mTorr and constant power of 300 W. The HfO_{2-x}(20 nm) layer was deposited by ALD at 200° C on 150 nm Pt. The devices showed typical 1S1M behavior as depicted in Fig. 4(a) and devices are structurally similar to that proposed in Fig. 6.3(b). Fig. 6.4(b) shows a cross-sectional transmission electron microscopy (XTEM) image of the fabricated sample.

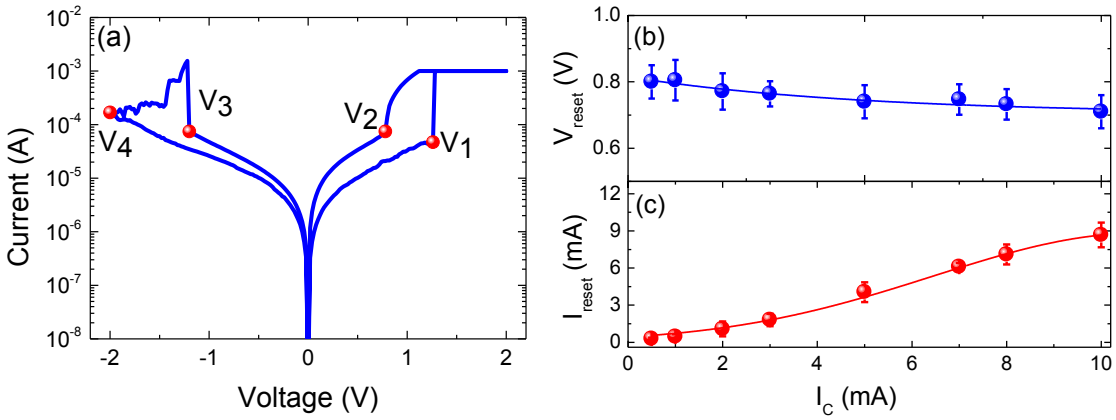

Figure 6.5 (a) I-V characteristics of the $Pt/Nb/NbO_{2-\delta}/HfO_{2-x}/Pt$ device structure and inset is the XTEM of the device structure. (b) I_{reset} and (c) absolute values of V_{reset} (V_3) as function of I_C are plotted for $Pt/Nb/NbO_{2-\delta}/HfO_{2-x}/Pt$ device structure.

A typical I-V characteristic from one of these structures is shown in Fig. 6.5(a). It is also important to note that the 1S1M behavior reported previously for a $Pt/NbO_{2-\delta}/HfO_{2-x}/Pt$ device structure involved a nonpolar (thermally induced) reset response rather than the gradual bipolar (field induced) reset observed here (as discussed in Chapter-5). The reset response at negative bias is clearly similar to that observed for the $Nb/HfO_2/Pt$ structure in Fig. 6.3(b). Analogous to bipolar switching, I_{reset} is defined as the maximum current during the reset (negative bias) process and V_{reset} (V_3) as the threshold voltage during reset sweep. I_{reset} and V_{reset} are plotted for the 1S1M response of this device as a function of I_C in Fig. 6.5(b-c), respectively. It is important to note that in voltage driven bipolar switching, I_C controls the I_{reset} and V_{reset} is almost constant, thus leading to to the relation $I_{reset} \propto 1/R_{filament}$ [169]. As shown in Fig. 6.5(c) I_{reset} increases with I_C, consistent with a reduction in the filament resistance.

6.5. Numerical Modelling of RESET Behaviour

A finite element model was constructed to represent the 1S1M behaviour based on the above understanding. Specifically, the model considers the evolution of a "memory" filament in a HfO_2 layer and the threshold switching response in a NbO_2 layer, as shown in Fig. 6.6(a). The threshold switching response of NbO_2 is assumed to result from a thermally-induced insulator-metal transition (IMT) as proposed by Pickett

et al [159] although recent works suggest that this model is not unique [170, 171]. A 10 nm NbO_2 interfacial oxide is consider for the threshold switching layer based on the thickness of the suboxide region observed in XTEM. This is similar to that reported for related material systems [172] but the simulation results are not strongly influenced by this value. The temperature distribution in the device is determined by solving the Fourier heat equation, taking account of Joule heating, and the IMT is modeled by assigning temperature dependent electrical and thermal conductivities for the NbO_2 layer (described in Chapter 5). Switching in the memory layer is based on the drift and diffusion of charged oxygen vacancies with temperature-dependent mobility and diffusivity and requires the solution of a suitable transport equation subject to local temperature and electric field [145]. The sample structure is defined in a 2-D axisymmetric geometry [Fig. 6.6(a)] and solved self-consistently. Results from the simulation are depicted in Fig. 6.6(b) which compares the experimentally measured 1S1M and the simulated RESET responses. The simulation is seen to accurately reproduce the experimental data, with the RESET transition starting at $\sim$0.8 V and the resistance gradually increasing with increasing voltage up to a voltage of -2 V.

The physical basis of 1S1M switching is further clarified in Fig. 6.6(c), which shows 2D plots of the temperature (upper row) of the selector layer and the defect density (lower row) in the memory layer during a reset sweep. The plots correspond to the five different points A, B, C, D and E indicated in Fig. 6.6(b). Fig. 6.6(c-A) reflects the pre-reset situation corresponding to point A at -0.5 V. As the voltage increases during the negative sweep the temperature increases as a result of Joule heating and initiates an IMT in the NbO_2 layer at the threshold voltage (point B). As soon as the temperature of the NbO_2 filament reaches the IMT temperature the current increases abruptly and reaches its maximum value, at which point the IMT region acts as a virtual cathode. A gap then opens in the memory filament due to defect drift and diffusion, and this increases with the increasing applied voltage (panel C-E), as shown in Fig. 6.6(c). The migration of ions is localized close to the NbO_2/HfO_2 interface due to the strong temperature dependence of the ion mobility but the gap is self-limiting due to the reduction in electric field and temperature as the gap increases, dependencies that gives rise to the gradual RESET response.

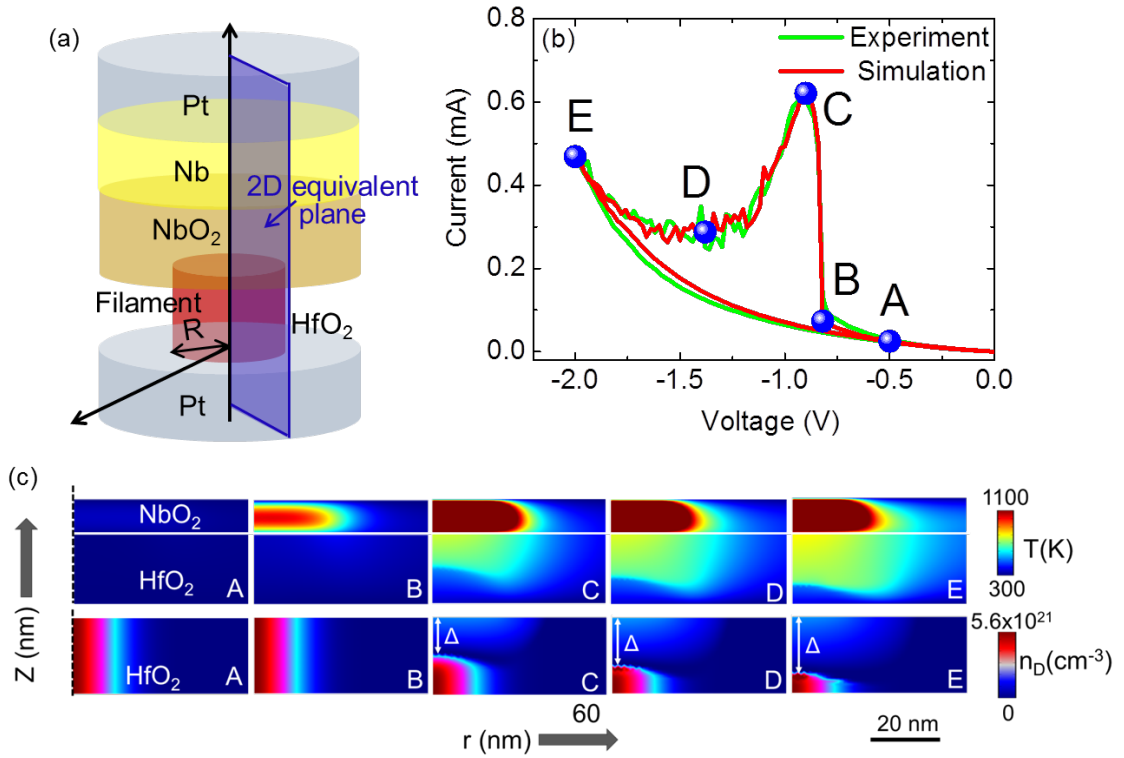

Figure 6.6 (a) Geometry of the simulated device structure assuming formation of NbO_2 interlayer. (b) The comparison of simulated and experimental 1S1M reset I-V characteristics of $Pt/Nb/HfO_2/Pt$. (c) 2D plots of temperature (upper row) for NbO_2 and HfO_2 layers, and defects (lower row) only for HfO_2 layer at five distinct points (A, B, C, D and E) as shown in the I-V curve of the simulation results.

At the end of the RESET cycle the NbO_2 volume reverts to its insulating state leaving the broken filament in the memory layer. In one reset cycle the hybrid device therefore undergoes the following sequence: S-off/M-LRS → S-on/M-LRS →S-on/M-HRS→S-off/M-HRS, where the S-on/M-HRS and S-on/M-LRS can be recognized as logic "0" and "1" states respectively. The read voltage V_{read} is usually chosen to lie between V_3 and V_4, where logic "0" and "1" states can be detected and the R_{OFF}/R_{ON} resistance ratio calculated.

The dependence of the 1S1M RESET process on filament size is shown in Fig. 6.7. I_{reset} increases and V_{reset} decreases with increasing filament radius in the memory layer, consistent with the I_C dependence depicted in Fig. 6.5(b). Fig. 6.7 (c-d) compare the 1D temperature and conductivity profiles in the NbO_2 layer at the reset voltage as a function of filaments radius. As the filament radius increases Joule heating increases and as a result the volume of heated NbO_2 also increases. Such

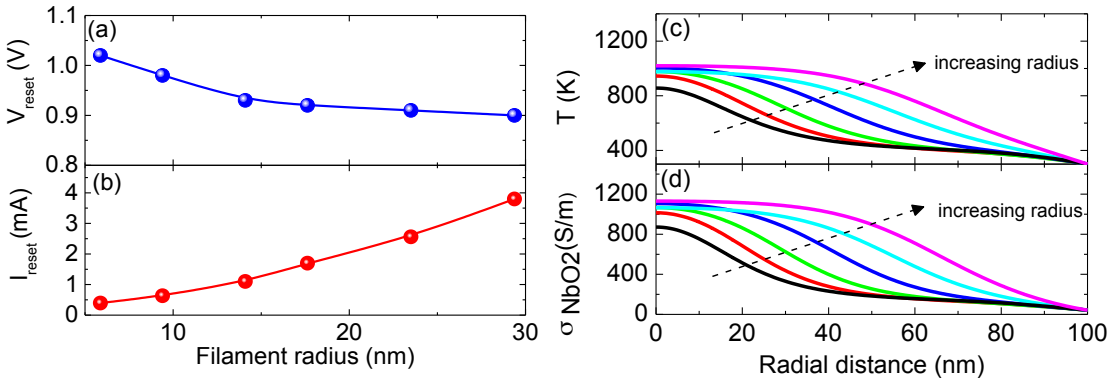

Figure 6.7 Calculated (a) absolute values V_{reset} and (b) I_{reset} as a function of the filament radius. (c) Temperature (T) and (d) electrical conductivity (σ_{NbO_2}) profile at the middle of the NbO_2 layer for different filament radius. simulation results.

data provides important insight into the scalability of devices.

6.6. Conclusion

It has been shown that the switching mode of Pt/Nb/HfO2/Pt ReRAM devices depends on the compliance current employed for the set operation. When operated at low compliance current (∼100 μA) the devices exhibited uniform bipolar resistive switching, as expected for filamentary switching in the HfO_2 layer. At intermediate currents (∼500 μA) the response transitioned to integrated 1S1M behavior and this was shown to be consistent with the development of an $NbO_{2-\delta}$ interlayer at the Nb/NbO_2 interface, with the switching characteristics reflecting the combined filamentary resistive-switching in the HfO_2 layer and threshold switching in the $NbO_{2-\delta}$ interlayer. At high currents (∼1 mA) the devices exhibited 1S threshold switching which was attributed to the development of a permanent filament in the HfO_2 layer and threshold switching in the $NbO_{2-\delta}$ interlayer. These changes were explained by an increase in oxygen ion transport from the conductive filament to the Nb/HfO_2 interface with increasing compliance current, and its reaction with the Nb electrode to form an $NbO_{2-\delta}$ interlayer. This was supported by an observed reduction in filament resistance with increasing set compliance current and by comparing measured characteristics with those predicted by finite element modeling.

These results demonstrate the important role of interface reactions in controlling device performance and provide a basis for the self-assembly of integrated 1S1M ReRAM structures.

CHAPTER 7

Conclusion

7.1. Conclusion and Summary

In this dissertation we have addressed: (a) the role of electrode roughness in electroforming and resistive switching characteristics, (b) strategies for making integrated memory-selector structures and dependence on memory layer; and (c) self assembly of a selector layer for low power integrated selector-memory.

Chapter 3 reported on an investigation of the stoichiometry, thickness and electronic structure of ALD HfO_2 and plasma deposited NbO_x films by electron Rutherford backscattering. This study was particularly useful for understanding the relationship between composition and electronic transport properties and for identifying the NbO_x composition range suitable for threshold and resistive switching. The study focussed on films with composition in the range NbO_2 to Nb_2O_5, with NbO_2 known to exhibit a thermally induced metal-insulator transition in its crystalline form and Nb_2O_5 known to be an excellent insulator. Comparison of these studies with electrical measurements reported in later chapters shoed that amorphous films with composition close to Nb_2O_5 were highly resistive and best suited to resistive switching, while those close to NbO_2 were relatively conductive and resulted in high leakage current. Films with compositions around $Nb_2O_{4.3}$ were found to have

moderate conductivities and to be the best for threshold switching applications.

Chapter 4 investigated the role of interface roughness on the electroforming and resistive switching characteristics of Pt/Ti/HfO_2/Pt device structures, and exploited that fact that the roughness of electron beam evaporated Pt electrodes was found to have a near exponential dependence on film thickness. Increasing the electrode roughness was shown to lead to a reduction in the electroforming voltage of HfO_2 and to a corresponding reduction in the resistive switching reliability. However, the observed effect was much less than expected from estimates of the electric field enhancement around electrode asperities. Finite element simulations showed that geometric effects could produce order-of-magnitude field-enhancements but that this was moderated by the generation and redistribution of charged defects in the high-field region prior to dielectric breakdown. As a consequence the effect of electrode geometry has much less impact than would be anticipated from the initial electric field distribution.

Chapter 5 investigated the integration of passive selector (1S)/memory (1M) elements and the role of material choices on the resulting switching characteristics. Two types of 1S1M device were studies: a homogeneous structure (NbO_{2-x}/Nb_2O_{5-y}) and a heterogeneous (NbO_{2-x}/HfO_2) structure. Integration was shown to result in reliable 1S1M operation and to reduce the threshold switching current of the selector element. The threshold current for the heterogeneous structure ($\sim$10 μA) was also found to be significantly lower than that of the homogeneous structure ($\sim$120 μA). Comparison with similar structures in which a permanent (i.e. non-switchable) filament was formed in the memory layer suggested that the reduction in threshold current was due to current confinement caused by the filamentary conduction (residual of permanent) path in the memory layer. This was confirmed by finite element modelling of the 1S1M switching response. The simulations further suggested that current confinement was greater in the HfO_2 layer than in the Nb_2O_5 layer as a result of a smaller diameter filament forming in this switching layer. The main limitation of these devices was shown to be the high compliance current ($\sim$5 mA) required to initiate threshold switching in the selector element. In the 1S1M structure this

current is also applied to the memory element and tends to form it in a very low resistance state that favours high-current unipolar operation.

Chapter 6 demonstrated an alternative approach to the fabrication of an integrated memory/selector device using the configurable resistive switching behaviour of Pt/Nb/HfO_2/Pt device structures subjected to different SET compliance currents. These devices required an initial compliance current of only ∼10 μA for the forming process but were shown to undergo modified behavior due to materials changes induced by subsequent operating conditions, and specifically the SET compliance current. At low SET compliance (∼100 μA) they showed uniform bipolar resistive switching behaviour characteristic of the HfO_2 active layer. As the compliance current was increased to ∼500 μA the switching mode changed from bipolar to 1S1R, similar to that observed for integrated threshold-switching and resistive switching elements. At even higher SET compliance (1 mA) the behaviour changed again to symmetric threshold switching only. These switching transitions were speculated to arise from the formation of a NbO_{2-x} interlayer at the Nb/HfO_2interface. This was verified by comparison with the switching response of isolated memory and selector structures and by finite element modelling of the proposed 1S1R structure which was found to accurately reproduce the reset response of the proposed 1S1M structure. This approach provides a means of limiting the forming current in the memory element and ensuring 1S1M operation with a bipolar memory response.

7.2. Future Research Directions

- This present study was concerned with relatively large device structures (typically 50-250 μm in diameter). While these are adequate for testing and understanding general behaviour extension to nanoscale devices is required to evaluate their full potential. For example, it is expected that the leakage current in 1S1M structures will be reduced by reducing the device area due to a reduction in parallel leakage currents that compete with the primary filamentary conduction.

- The study of threshold switching in this thesis was predicated on the assumption that it results from a thermally-induced metal-insulator transition. However, the actual mechanism remains unclear and there is growing evidence that it may results from self-filamentation due to local Joule heating and the temperature dependence of Pool-Frenkel transport. Further work is clearly required to determine the dominant mechanism and its implications.

- The present study has been concerned with non-volatile memory applications of resistive and threshold switching. However, there are many other applications of interest, including neuromorphic computing where these switching devices are of interest for artificial synapses and neurons. While based on the same physical processes these applications have different functional requirements and require further work to explore their full potential.

Bibliography

[1] F. Masuoka, M. Momodomi, Y. Iwata, and R. Shirota. New ultra high density EPROM and flash EEPROM with NAND structure cell. In *Electron Devices Meeting, 1987 International*, volume 33, pages 552–555. IEEE, 1987.

[2] J. A. Hutchby, R. Cavin, V. Zhirnov, J. E. Brewer, and G. Bourianoff. Emerging nanoscale memory and logic devices: a critical assessment. *Computer*, 41(5):28–32, 2008.

[3] H.-S. P. Wong, H.-Y. Lee, S. Yu, Y.-S. Chen, Y. Wu, P.-S. Chen, B. Lee, F. T. Chen, and M.-J. Tsai. Metal-oxide RRAM. *Proceedings of the IEEE*, 100(6):1951–1970, 2012.

[4] T. Hickmott. Low-frequency negative resistance in thin anodic oxide films. *J. Appl. Phys.*, 33(9):2669–2682, 1962.

[5] H. Pagnia and N. Sotnik. Bistable switching in electroformed metal-insulator-metal devices. *Phys. Status Solidi A*, 108(1):11–65, 1988.

[6] S. D. Ha and S. Ramanathan. Adaptive oxide electronics: a review. *J. Appl. Phys.*, 110(7):071101, 2011.

[7] J. Robertson. High dielectric constant gate oxides for metal oxide Si transistors. *Rep. Prog. Phys.*, 69(2):327, 2005.

[8] R. Waser, R. Dittmann, G. Staikov, and K. Szot. Redox-based resistive switching memories–nanoionic mechanisms, prospects, and challenges. *Adv. Mater.*, 21(25-26):2632–2663, 2009.

[9] I. Valov, R. Waser, J. R. Jameson, and M. N. Kozicki. Electrochemical metallization memories-fundamentals, applications, prospects. *Nanotechnology*, 22(25):254003, 2011.

[10] D. Ielmini, R. Bruchhaus, and R. Waser. Thermochemical resistive switching: materials, mechanisms, and scaling projections. *Phase Transitions*, 84(7):570–602, 2011.

[11] L. Goux, J. Lisoni, M. Jurczak, D. Wouters, L. Courtade, and C. Muller. Coexistence of the bipolar and unipolar resistive-switching modes in NiO cells made by thermal oxidation of ni layers. *J. Appl. Phys.*, 107(2):024512, 2010.

[12] C. Kim, Y. Jang, H. Hwang, Z. Sun, H. Moon, and J. Cho. Observation of bistable resistance memory switching in CuO thin films. *Appl. Phys. Lett.*, 94(10):102107, 2009.

[13] J. S. Kwak, Y. H. Do, Y. C. Bae, H. Im, and J. P. Hong. Reproducible unipolar resistive switching behaviors in the metal-deficient CoO_x thin film. *Thin Solid Films*, 518(22):6437–6440, 2010.

[14] J.-Y. Lee, Y.-J. Baek, Q. Hu, Y. J. Choi, C. J. Kang, H. H. Lee, H.-M. Kim, K.-B. Kim, and T.-S. Yoon. Multimode threshold and bipolar resistive switching in bi-layered $Pt - Fe_2O_3$ core-shell and Fe_2O_3 nanoparticle assembly. *App. Phys. Lett.*, 102(12):122111, 2013.

[15] W.-Y. Chang, Y.-C. Lai, T.-B. Wu, S.-F. Wang, F. Chen, and M.-J. Tsai. Unipolar resistive switching characteristics of ZnO thin films for nonvolatile memory appl.ications. *Appl. Phys. Lett.*, 92(2):2110, 2008.

[16] X. Cao, X. Li, X. Gao, W. Yu, X. Liu, Y. Zhang, L. Chen, and X. Cheng. Forming-free colossal resistive switching effect in rare-earth-oxide Gd_2O_3 films for memristor applications. *J. Appl. Phys.*, 106(7):073723, 2009.

[17] M. K. Yang, J.-W. Park, T. K. Ko, and J.-K. Lee. Bipolar resistive switching behavior in Ti/MnO_2/Pt structure for nonvolatile memory devices. *App. Phys. Lett.*, 95(4):2105, 2009.

[18] S. Kim, X. Liu, J. Park, S. Jung, W. Lee, J. Woo, J. Shin, G. Choi, C. Cho, S. Park, et al. Ultrathin ($\sim$ 10nm) Nb_2O_5/NbO_2 hybrid memory with both memory and selector characteristics for high density 3D vertically stackable RRAM applications. In *VLSI Technology (VLSIT), 2012 Symposium on*, pages 155–156. IEEE, 2012.

[19] L. Goux, P. Czarnecki, Y. Y. Chen, L. Pantisano, X. Wang, R. Degraeve, B. Govoreanu, M. Jurczak, D. Wouters, and L. Altimime. Evidences of oxygen-mediated resistive-switching mechanism in TiN/HfO_2/Pt cells. *Appl. Phys. Lett.*, 97(24):243509, 2010.

[20] K. P. Biju, X. Liu, M. Siddik, S. Kim, J. Shin, I. Kim, A. Ignatiev, and H. Hwang. Resistive switching characteristics and mechanism of thermally grown WO_x thin films. *J. App. Phys.*, 110(6):064505, 2011.

[21] C.-Y. Lin, C.-Y. Wu, C.-Y. Wu, C. Hu, and T.-Y. Tseng. Bistable resistive switching in Al_2O_3 memory thin films. *J. Electrochem. Soc.*, 154(9):G189–G192, 2007.

[22] H. Jiang and Q. Xia. Effect of voltage polarity and amplitude on electroforming of TiO_2 based memristive devices. *Nanoscale*, 5(8):3257–3261, 2013.

[23] N. Ge, M. Zhang, L. Zhang, J. J. Yang, Z. Li, and R. S. Williams. Electrode-material dependent switching in TaO_x memristors. *Semiconductor Science and Technology*, 29(10):104003, 2014.

[24] C. He, Z. Shi, L. Zhang, W. Yang, R. Yang, D. Shi, and G. Zhang. Multilevel resistive switching in planar graphene/sio2 nanogap structures. *ACS nano*, 6(5):4214–4221, 2012.

[25] C. Chen, Y. Yang, F. Zeng, and F. Pan. Bipolar resistive switching in Cu/AlN/Pt nonvolatile memory device. *Appl. Phys. Lett*, 97(8):083502–1, 2010.

[26] H.-D. Kim, M. J. Yun, and T. G. Kim. Self-selection bipolar resistive switching phenomena observed in NbON/NbN bilayer for cross-bar array memory applications. *Appl. Phys. Lett.*, 105(21):213510, 2014.

[27] H.-D. Kim, H.-M. An, and T. G. Kim. Ultrafast resistive-switching phenomena observed in NiN-based ReRAM cells. *IEEE Trans. Electron Devices*, 59(9):2302–2307, 2012.

[28] K. Szot, R. Dittmann, W. Speier, and R. Waser. Nanoscale resistive switching in $SrTiO_3$ thin films. *Phys. Status Solidi -Rapid Res. Lett.*, 1(2):R86–R88, 2007.

[29] C.-Y. Liu, P.-H. Wu, A. Wang, W.-Y. Jang, J.-C. Young, K.-Y. Chiu, and T.-Y. Tseng. Bistable resistive switching of a sputter-deposited *cr*-doped $SrZrO_3$ memory film. *IEEE Electron Device Lett.*, 26(6):351–353, 2005.

[30] J. van den Hurk, I. Valov, and R. Waser. Preparation and characterization ofGeS_x thin-films for resistive switching memories. *Thin Solid Films*, 527:299–302, 2013.

[31] S. Rahaman, S. Maikap, H.-C. Chiu, C.-H. Lin, T.-Y. Wu, Y.-S. Chen, P.-J. Tzeng, F. Chen, M.-J. Kao, and M.-J. Tsai. Bipolar resistive switching memory using Cu metallic filament in $Ge_{0.4}Se_{0.6}$ solid electrolyte. *Electrochem. Solid-State Lett.*, 13(5):H159–H162, 2010.

[32] X. Liu, M. T. Mayer, and D. Wang. Negative differential resistance and resistive switching behaviors in Cu_2S nanowire devices. *App. Phys. Lett.*, 96(22):223103, 2010.

[33] C. Collier, E. Wong, M. Belohradskỳ, F. Raymo, J. Stoddart, P. Kuekes, R. Williams, and J. Heath. Electronically configurable molecular-based logic gates. *Science*, 285(5426):391–394, 1999.

[34] A. Elsharkawi. Switching and memory phenomena in anthracene thin films. *J. Phys. Chem. Solids*, 38:95–96, 1977.

[35] A. Szymanski, D. Larson, and M. Labes. A temperature-dependent conducting state in Tetracene thin film C. *App. Phys. Lett.*, 14(3):88–90, 1969.

[36] F. Moresco, G. Meyer, K.-H. Rieder, H. Tang, A. Gourdon, and C. Joachim. Conformational changes of single molecules induced by scanning tunneling microscopy manipulation: a route to molecular switching. *Phys. Rev. Lett.*, 86(4):672, 2001.

[37] J. Cornil, Y. Karzazi, and J. Bredas. Negative differential resistance in phenylene ethynylene oligomers. *J. Am. Chem. Soc.*, 124(14):3516–3517, 2002.

[38] J. J. Yang, D. B. Strukov, and D. R. Stewart. Memristive devices for computing. *Nat. Nanotechno.*, 8(1):13–24, 2013.

[39] J. S. Lee, S. B. Lee, B. Kahng, and T. W. Noh. Two opposite hysteresis curves in semiconductors with mobile dopants. *Appl. Phys. Lett.*, 102(25):253503, 2013.

[40] S. H. Jeon, W.-J. Son, B. H. Park, and S. Han. Multiscale simulation on electromigration of the oxygen vacancies in metal oxides. *Appl. Phys. A*, 102(4):909–914, 2011.

[41] M.-J. Lee, C. Lee, D. Lee, S. Lee, M. Chang, J. Hur, Y.-B. Kim, C.-J. Kim, D. Seo, S. Seo, U.-I. Chung, I.-K. Yoo, and K. Kim. A fast, high-endurance and scalable non-volatile memory device made from asymmetric Ta_2O_5/TaO_{2-} bilayer structures. *Nat. Mater.*, 10(8):625–630, 2011.

[42] M. Uenuma, Y. Ishikawa, and Y. Uraoka. Joule heating effect in nonpolar and bipolar resistive random access memory. *Appl. Phys. Lett.*, 107(7):073503, 2015.

[43] D.-H. Kwon, K. M. Kim, J. H. Jang, J. M. Jeon, M. H. Lee, G. H. Kim, X.-S. Li, G.-S. Park, B. Lee, S. Han, et al. Atomic structure of conducting nanofilaments in TiO_2 resistive switching memory. *Nat. Nanotech.*, 5(2):148–153, 2010.

[44] Q. Liu, J. Sun, H. Lv, S. Long, K. Yin, N. Wan, Y. Li, L. Sun, and M. Liu. Real-time observation on dynamic growth/dissolution of conductive filaments in oxide-electrolyte-based ReRAM. *Adv. Mater.*, 24(14):1844–1849, 2012.

[45] H. Y. Jeong, J. Y. Lee, and S.-Y. Choi. Direct observation of microscopic change induced by oxygen vacancy drift in amorphous TiO_2 thin films. *Appl. Phys. Lett.*, 97(4), 2010.

[46] J. P. Strachan, M. D. Pickett, J. J. Yang, S. Aloni, A. David Kilcoyne, G. Medeiros-Ribeiro, and R. Stanley Williams. Direct identification of the conducting channels in a functioning memristive device. *Adv. Mater.*, 22(32):3573–3577, 2010.

[47] C. Yoshida, K. Kinoshita, T. Yamasaki, and Y. Sugiyama. Direct observation of oxygen movement during resistance switching in NiO/Pt film. *App. Phys. Lett.*, 93(4):042106, 2008.

[48] M.-J. Lee, S. Han, S. H. Jeon, B. H. Park, B. S. Kang, S.-E. Ahn, K. H. Kim, C. B. Lee, C. J. Kim, I.-K. Yoo, et al. Electrical manipulation of nanofilaments in transition-metal oxides for resistance-based memory. *Nano Lett.*, 9(4):1476–1481, 2009.

[49] S. Kumar, M. D. Pickett, J. P. Strachan, G. Gibson, Y. Nishi, and R. S. Williams. Local temperature redistribution and structural transition during joule-heating-driven conductance switching in VO_2. *Adv. Mater.*, 25(42):6128–6132, 2013.

[50] H. Frohlich. On the theory of dielectric breakdown in solids. In *Proceedings of the Royal Society of London A: Mathematical, Physical and Engineering Sciences*, volume 188, pages 521–532. The Royal Society, 1947.

[51] J. McPherson, J.-Y. Kim, A. Shanware, and H. Mogul. Thermochemical description of dielectric breakdown in high dielectric constant materials. *Appl. Phys. Lett.*, 82(13):2121–2123, 2003.

[52] J. McPherson and H. Mogul. Underlying physics of the thermochemical E model in describing low-field time-dependent dielectric breakdown in SiO_2 thin films. *J. Appl. Phys.*, 84(3):1513–1523, 1998.

[53] J. Stathis. Percolation models for gate oxide breakdown. *J. Appl. Phys.*, 86(10):5757–5766, 1999.

[54] S. Clima, B. Govoreanu, M. Jurczak, and G. Pourtois. HfO_x as rram material-first principles insights on the working principles. *Microelectronic Engineering*, 120:13–18, 2014.

[55] M. K. Yang, H. Ju, G. H. Kim, J.-K. Lee, and H.-C. Ryu. Direct evidence on Ta-metal phases igniting resistive switching in TaO_x thin film. *Scientific Rep.*, 5, 2015.

[56] G. H. Kim, J. H. Lee, J. Y. Seok, S. J. Song, J. H. Yoon, K. J. Yoon, M. H. Lee, K. M. Kim, H. D. Lee, S. W. Ryu, et al. Improved endurance of resistive switching TiO_2 thin film by hourglass shaped magnéli filaments. *Appl. Phys. Lett.*, 98(26):262901, 2011.

[57] S. Johnson, A. Sundararajan, D. Hunley, and D. Strachan. Memristive switching of single-component metallic nanowires. *Nanotechnology*, 21(12):125204, 2010.

[58] H. Akinaga and H. Shima. Resistive random access memory (ReRAM) based on metal oxides. *Proceedings of the IEEE*, 98(12):2237–2251, 2010.

[59] H. Shima, F. Takano, H. Akinaga, Y. Tamai, I. H. Inoue, and H. Takagi. Resistance switching in the metal deficient-type oxides: NiO and CoO. *App. Phys. Lett.*, 91(1):2901, 2007.

[60] P. Zhou, M. Yin, H. Wan, H. Lu, T. Tang, and Y. Lin. Role of TaON interface for Cu_xO resistive switching memory based on a combined model. *Appl. Phys. Lett.*, 94(5):053510, 2009.

[61] X. Liu, S. M. Sadaf, S. Kim, K. P. Biju, X. Cao, M. Son, S. H. Choudhury, G.-Y. Jung, and H. Hwang. Improvement of resistive switching uniformity by introducing a thin NbO_x interface layer. *ECS Solid State Lett.*, 1(5):Q35–Q38, 2012.

[62] Y. Y. Chen, L. Goux, S. Clima, B. Govoreanu, R. Degraeve, G. S. Kar, A. Fantini, G. Groeseneken, D. J. Wouters, and M. Jurczak. Endurance/retention trade-off on cap 1T1R bipolar RRAM. *IEEE Trans. Electron Devices*, 60(3):1114–1121, 2013.

[63] S. Jung, J. Shin, and H. Hwang. Effect of ZrO_x/HfO_x bilayer structure on switching uniformity and reliability in nonvolatile memory applications. *Appl. Phys. Lett.*, 97:172105, 2010.

[64] J. H. Hur, M.-J. Lee, C. B. Lee, Y.-B. Kim, and C.-J. Kim. Modeling for bipolar resistive memory switching in transition-metal oxides. *Phys. Rev. B*, 82(15):155321, 2010.

[65] G.-S. Park, Y. B. Kim, S. Y. Park, X. S. Li, S. Heo, M.-J. Lee, M. Chang, J. H. Kwon, M. Kim, U.-I. Chung, et al. In situ observation of filamentary conducting channels in an asymmetric Ta_2O_{5-x}/TaO_{2-x} bilayer structure. *Nat. Commun.*, 4, 2013.

[66] X. Y. Li, X. L. Shao, Y. C. Wang, H. Jiang, C. S. Hwang, and J. S. Zhao. Thin TiO_x layer as a voltage divider layer located at the quasi-ohmic junction in the $Pt/Ta_2O_5/Ta$ resistance switching memory. *Nanoscale*, 9(6):2358–2368, 2017.

[67] F. Miao, J. J. Yang, J. Borghetti, G. Medeiros-Ribeiro, and R. S. Williams. Observation of two resistance switching modes in TiO_2 memristive devices electroformed at low current. *Nanotechnology*, 22(25):254007, 2011.

[68] H. Lee, P. Che, T. Wu, Y. Che, C. Wan, P. Tzen, C. Lin, F. Chen, C. Lien, and M. Tsai. Low power and high speed bipolar switching with a thin reactive Ti buffer layer in robust HfO_2 based RRAM. In *Electron Devices Meeting, 2008. IEDM 2008. IEEE International*, pages 1–4. IEEE, 2008.

[69] F. Chudnovskii, L. Odynets, A. Pergament, and G. Stefanovich. Electroforming and switching in oxides of transition metals: the role of metal-insulator transition in the switching mechanism. *J. Solid State Chem.*, 122(1):95–99, 1996.

[70] S. H. Chang, S. B. Lee, D. Y. Jeon, S. J. Park, G. T. Kim, S. M. Yang, S. C. Chae, H. K. Yoo, B. S. Kang, M.-J. Lee, et al. Oxide double-layer nanocrossbar for ultrahigh-density bipolar resistive memory. *Adv. Mater.*, 23(35):4063–4067, 2011.

[71] M.-J. Lee, Y. Park, D.-S. Suh, E.-H. Lee, S. Seo, D.-C. Kim, R. Jung, B.-S. Kang, S.-E. Ahn, C. B. Lee, et al. Two series oxide resistors applicable to high speed and high density nonvolatile memory. *Adv. Mater.*, 19(22):3919–3923, 2007.

[72] J. Lee, E. Cha, Y. Kim, B. Chae, J. Kim, S. Lee, H. Hwang, and C. Park. A study of threshold switching of NbO_2 using atom probe tomography and transmission electron microscopy. *Micron*, 79:101–109, 2015.

[73] K. J. Norris, J. J. Yang, and N. P. Kobayashi. Self-aligned NbO_2 nano-cap for negative differential resistance resistive switching devices. *Materials Growth and Characterization of Thermoelectric and Resistive Switching Devices*, page 128, 2015.

[74] Z. Yang, C. Ko, and S. Ramanathan. Oxide electronics utilizing ultrafast metal-insulator transitions. *Annual Rev. Mater. Res.*, 41:337–367, 2011.

[75] V. Eyert. The metal-insulator transition of NbO_2: an embedded peierls instability. *EPL (Europhys. Lett.)*, 58(6):851, 2002.

[76] A. O'Hara, T. N. Nunley, A. B. Posadas, S. Zollner, and A. A. Demkov. Electronic and optical properties of NbO_2. *J. App. Phys.*, 116(21):213705, 2014.

[77] J. D. Budai, J. Hong, M. E. Manley, E. D. Specht, C. W. Li, J. Z. Tischler, D. L. Abernathy, A. H. Said, B. M. Leu, L. A. Boatner, et al. Metallization of vanadium dioxide driven by large phonon entropy. *Nature*, 515(7528):535–539, 2014.

[78] V. Iglesias, M. Porti, M. Nafría, X. Aymerich, P. Dudek, T. Schroeder, and G. Bersuker. Correlation between the nanoscale electrical and morphological properties of crystallized hafnium oxide-based metal oxide semiconductor structures. *Appl. Phys. Lett.*, 97(26):262906, 2010.

[79] K. McKenna, A. Shluger, V. Iglesias, M. Porti, M. Nafría, M. Lanza, and G. Bersuker. Grain boundary mediated leakage current in polycrystalline HfO_2 films. *Microelectron. Eng.*, 88(7):1272–1275, 2011.

[80] K. McKenna and A. Shluger. The interaction of oxygen vacancies with grain boundaries in monoclinic HfO_2. *App. Phys. Lett.*, 95(22):2111, 2009.

[81] G. Bersuker, D. Gilmer, D. Veksler, P. Kirsch, L. Vandelli, A. Padovani, L. Larcher, K. McKenna, A. Shluger, V. Iglesias, et al. Metal oxide resistive memory switching mechanism based on conductive filament properties. *J. Appl. Phys.*, 110(12):124518, 2011.

[82] K. McKenna and A. Shluger. First-principles calculations of defects near a grain boundary in MgO. *Phys. Rev. B*, 79(22):224116, 2009.

[83] G. Bersuker, J. Yum, L. Vandelli, A. Padovani, L. Larcher, V. Iglesias, M. Porti, M. Nafria, K. McKenna, A. Shluger, et al. Grain boundary-driven leakage path formation in HfO_2 dielectrics. *Solid-State Electron.*, 65:146–150, 2011.

[84] N. Raghavan. Performance and reliability trade-offs for high-κ RRAM. *Microelectron. Reliab.*, 54(9):2253–2257, 2014.

[85] G.-S. Park, X.-S. Li, D.-C. Kim, R.-J. Jung, M.-J. Lee, and S. Seo. Observation of electric-field induced Ni filament channels in polycrystalline NiO_x film. *App. Phys. Lett.*, 91(22):222103–222103, 2007.

[86] J. Molina, R. Valderrama, C. Zuniga, P. Rosales, W. Calleja, A. Torres, J. D. Hidalga, and E. Gutierrez. Influence of the surface roughness of the bottom electrode on the resistive-switching characteristics of $Al/Al_2O_3/Al$ and $Al/Al_2O_3/W$ structures fabricated on glass at 300°c. *Microelectronics Reliability*, 54(12):2747–2753, 2014.

[87] H.-D. Kim, M. J. Yun, S. M. Hong, J. H. Park, D. S. Jeon, and T. G. Kim. Impact of roughness of bottom electrodes on the resistive switching properties of platinum/nickel nitride/nickel $1\times$ 1 crossbar array resistive random access memory cells. *Microelectron. Eng.*, 126:169–172, 2014.

[88] Y.-P. Zhao, G.-C. Wang, T.-M. Lu, G. Palasantzas, and J. T. M. De Hosson. Surface-roughness effect on capacitance and leakage current of an insulating film. *Phys. Rev. B*, 60(12):9157, 1999.

[89] P. Lazić and B. Persson. Surface-roughness–induced electric-field enhancement and triboluminescence. *Europhys. Lett.*, 91(4):46003, 2010.

[90] N. Gaillard, L. Pinzelli, M. Gros-Jean, and A. Bsiesy. In situ electric field simulation in metal/insulator/metal capacitors. *Appl. Phys. Lett.*, 89(13):133506–133506, 2006.

[91] Y. Kim, M. Sung, Y. Lee, B. Ju, and M. Oh. The influence of surface roughness on the electric conduction process in amorphous Ta_2O_5 thin films. *J. Electrochem. Soc.*, 146(9):3398–3402, 1999.

[92] S. Yu, H.-Y. Chen, B. Gao, J. Kang, and H.-S. P. Wong. HfO_x-based vertical resistive switching random access memory suitable for bit-cost-effective three-dimensional cross-point architecture. *ACS Nano*, 7(3):2320–2325, 2013.

[93] X. Tran, B. Gao, J. Kang, L. Wu, Z. Wang, Z. Fang, K. Pey, Y. Yeo, A. Du, B. Nguyen, et al. High performance unipolar AlO_y/HfO_x/Ni based RRAM compatible with Si diodes for 3D application. In *VLSI Technology (VLSIT), 2011 Symposium on*, pages 44–45. IEEE, 2011.

[94] C.-H. Wang, Y.-H. Tsai, K.-C. Lin, M.-F. Chang, Y.-C. King, C.-J. Lin, S.-S. Sheu, Y.-S. Chen, H.-Y. Lee, F. T. Chen, et al. Three-dimensional $4F^2$ ReRAM cell with CMOS logic compatible process. In *Electron Devices Meeting (IEDM), 2010 IEEE International*, pages 29–6. IEEE, 2010.

[95] H. Mahne, H. Wylezich, S. Slesazeck, T. Mikolajick, J. Vesely, V. Klemm, and D. Rafaja. Room temperature fabricated NbO_x/ Nb_2O_5 memory switching device with threshold switching effect. In *Memory Workshop (IMW), 2013 5th IEEE International*, pages 174–177. IEEE, 2013.

[96] X. Liu, S. M. Sadaf, M. Son, J. Park, J. Shin, W. Lee, K. Seo, D. Lee, and H. Hwang. Co-occurrence of threshold switching and memory switching in cells for crosspoint memory applications. *IEEE Electron Device Lett.*, 33(2):236–238, 2012.

[97] X. Liu, S. M. Sadaf, M. Son, J. Shin, J. Park, J. Lee, S. Park, and H. Hwang. Diode-less bilayer oxide ($WO_x - NbO_x$) device for cross-point resistive memory applications. *Nanotechnology*, 22(47):475702, 2011.

[98] E. Cha, J. Woo, D. Lee, S. Lee, J. Song, Y. Koo, J. Lee, C. G. Park, M. Y. Yang, K. Kamiya, et al. Nanoscale ($\sim$ 10 nm) 3D vertical reram and NbO_2 threshold selector with TiN electrode. In *Electron Devices Meeting (IEDM), 2013 IEEE International*, pages 10–5. IEEE, 2013.

[99] Nanolab technologies inc. `http://www.nanolabtechnologies.com`.

[100] *Savannah 100, 200 & 300 Atomic layer deposition system maintenance manual*, 2009.

[101] Aja international inc., atc flagship series sputtering systems. `http://www.ajaint.com`.

[102] Temescal's bjd-1800. `https://www.temescal.net`.

[103] D. Nečas and P. Klapetek. Gwyddion: an open-source software for SPM data analysis. *Open Phys.*, 10(1):181–188, 2012.

[104] Panalytical b.v. `www.panalytical.com/`.

[105] *X'Pert HighScore and HighScore Plus, Total x-ray powder pattern analysis*, 2009.

[106] W. Chu, J. Mayer, and M. Nicolet. *Backscattering spectrometry*. Academic Press, 1978.

[107] B1500a semiconductor device parameter analyze. `http://www.keysight.com`.

[108] Signatone s-1160 probe station. `www.signatone.com`.

[109] A. Sawa. Resistive switching in transition metal oxides. *Mat. Today*, 11(6):28–36, 2008.

[110] L. Pereira, P. Barquinha, E. Fortunato, R. Martins, D. Kang, C. Kim, H. Lim, I. Song, and Y. Park. High k dielectrics for low temperature electronics. *Thin Solid Films*, 516(7):1544–1548, 2008.

[111] X. Wu, D. Migas, X. Li, M. Bosman, N. Raghavan, V. Borisenko, and K. Pey. Role of oxygen vacancies in HfO_2-based gate stack breakdown. *Appl. Phys. Lett.*, 96(17):172901, 2010.

[112] D. P. Woodruff and T. A. Delchar. *Modern techniques of surface science*. Cambridge university press, 1994.

[113] M. Vos and M. Went. Splitting the plasmon peak in high-energy reflection electron energy loss experiments. *J. Electron Spectrosc. Relat. Phenom.*, 162(1):1–7, 2008.

[114] F. Salvat, A. Jablonski, and C. J. Powell. ELSEPA-dirac partial-wave calculation of elastic scattering of electrons and positrons by atoms, positive ions and molecules. *Comp. Phys. Commun.*, 165(2):157–190, 2005.

[115] M. C. Cheynet, S. Pokrant, F. D. Tichelaar, and J.-L. Rouvière. Crystal structure and band gap determination of HfO_2 thin films. *J. App. Phys. , 101 (5), 2007*, 2007.

[116] S. Miyazaki, H. Nishimura, M. Fukuda, L. Ley, and J. Ristein. Structure and electronic states of ultrathin sio2 thermally grown on si (100) and si (111) surfaces. *Applied surface science*, 113:585–589, 1997.

[117] B. Maurel, G. Amsel, and J. Nadai. Depth profiling with narrow resonances of nuclear reactions: theory and experimental use. *Nucl. Instrum. Methods B*, 197(1):1–13, 1982.

[118] M. Went and M. Vos. Rutherford backscattering using electrons as projectiles: underlying principles and possible applications. *Nucl. Instrum. Methods B*, 266(6):998–1011, 2008.

[119] J. F. Ziegler, M. D. Ziegler, and J. P. Biersack. SRIM-the stopping and range of ions in matter. *Nucl. Instrum. Methods B*, 268(11):1818–1823, 2010.

[120] Q. Yang, D. O'Connor, and Z. Wang. Empirical formulae for energy loss straggling of ions in matter. *Nucl. Instrum. Methods B*, 61(2):149–155, 1991.

[121] M. A. Henderson. A surface perspective on self-diffusion in rutile TiO_2. *Surface Science*, 419(2–3):174 – 187, 1999.

[122] J. J. Yang and R. S. Williams. Memristive devices in computing system: promises and challenges. *ACM J. Emerg. Tech. Comp. Syst.*, 9(2):11, 2013.

[123] J. Y. Seok, S. J. Song, J. H. Yoon, K. J. Yoon, T. H. Park, D. E. Kwon, H. Lim, G. H. Kim, D. S. Jeong, and C. S. Hwang. A review of three-dimensional resistive switching cross-bar array memories from the integration and materials property points of view. *Adv. Funct. Mater.*, 24(34):5316–5339, 2014.

[124] M. Lopes, S. dos Santos Fo, C. Hasenack, and V. Baranauskas. $Si - SiO_2$ electronic interface roughness as a consequence of $Si - SiO_2$ topographic interface roughness. *J. Electrochem. Soc.*, 143(3):1021–1025, 1996.

[125] K. Chen, M. Nielsen, S. Soss, E. J. Rymaszewski, T.-M. Lu, and C. T. Wan. Study of tantalum oxide thin film capacitors on metallized polymer sheets for advanced packaging applications. *IEEE Trans. Components, Packaging, and Manufacturing Technology, Part B: Advanced Packaging*, 20(2):117–122, 1997.

[126] Q. Xia, J. J. Yang, W. Wu, X. Li, and R. S. Williams. Self-aligned memristor cross-point arrays fabricated with one nanoimprint lithography step. *Nano Lett.*, 10(8):2909–2914, 2010.

[127] P. A. Kumar, B. Panda, S. Ray, B. Mathur, D. Bhattacharya, and K. Chopra. Effect of electrode microstructure on leakage current in lead–lanthanum–zirconate–titanate multilayer capacitors. *Appl. Phys. Lett.*, 68(10):1344–1346, 1996.

[128] S.-D. Cho and K.-W. Paik. Study on the amorphous Ta_2O_5 thin film capacitors deposited by dc magnetron reactive sputtering for multichip module applications. *Mater. Sci. Eng.: B*, 67(3):108–112, 1999.

[129] Y. S. Kim, Y. H. Lee, K. M. Lim, and M. Y. Sung. The effect of $Al - Ta_2O_5$ topographic interface roughness on the leakage current of TiO_2 thin films. *Appl. Phys. Lett.*, 74(19):2800–2802, 1999.

[130] J. Zhang and J. B. Adams. Modeling and visualization of polycrystalline thin film growth. *Computational materials science*, 31(3):317–328, 2004.

[131] A. Czanderna, T. Madey, and C. Powell. *Beam Effects, Surface Topography, and Depth Profiling in Surface Analysis*. Infectious Agents and Pathogenesis. Springer US, 1998.

[132] G. Palasantzas. Roughness spectrum and surface width of self-affine fractal surfaces via the k-correlation model. *Phys. Rev. B*, 48(19):14472, 1993.

[133] V. Jovanov, X. Xu, S. Shrestha, M. Schulte, J. Hupkes, and D. Knipp. Predicting the interface morphologies of silicon films on arbitrary substrates: application in solar cells. *ACS Appl. Mater. Interfaces*, 5(15):7109–7116, 2013.

[134] D. Fabiani and L. Simoni. Discussion on application of the weibull distribution to electrical breakdown of insulating materials. *Dielectrics and Electrical Insulation, IEEE Transactions on*, 12(1):11–16, 2005.

[135] S. Yao. Theoretical model of thin-film deposition profile with shadow effect. *J. App. Phys.*, 50(5):3390–3395, 1979.

[136] R. Karunasiri, R. Bruinsma, and J. Rudnick. Thin-film growth and the shadow instability. *Phys. Rev. Lett.*, 62(7):788, 1989.

[137] M. S. Mathur. *The engineering and optimization of the hafnium based metal oxide semiconductor structure*. ProQuest, 2008.

[138] A. Chen. Area and thickness scaling of forming voltage of resistive switching memories. *IEE Electron Device Lett.*, 35(1):57–59, 2014.

[139] M. Elrawemi, L. Blunt, L. Fleming, D. Bird, D. Robbins, and F. Sweeney. Modelling water vapour permeability through atomic layer deposition coated photovoltaic barrier defects. *Thin Solid Films*, 570:101–106, 2014.

[140] M. Groner, J. Elam, F. Fabreguette, and S. M. George. Electrical characterization of thin Al_2O_3 films grown by atomic layer deposition on silicon and various metal substrates. *Thin Solid Films*, 413(1):186–197, 2002.

[141] Y. Zhang, J. A. Bertrand, R. Yang, S. M. George, and Y. Lee. Electroplating to visualize defects in Al_2O_3 thin films grown using atomic layer deposition. *Thin Solid Films*, 517(11):3269–3272, 2009.

[142] J. Dendooven, K. Devloo-Casier, M. Ide, K. Grandfield, K. F. Ludwig, S. Bals, P. Van Der Voort, and C. Detavernier. In situ study of ALD processes using synchrotron-based x-ray fluorescence and scattering techniques. *ECS Trans.*, 50(13):35–42, 2013.

[143] A. Lankhorst, B. Paarhuis, H. Terhorst, P. Simons, and C. Kleijn. Transient ALD simulations for a multi-wafer reactor with trenched wafers. *Surface and Coatings Technology*, 201(22):8842–8848, 2007.

[144] H. Knoops, E. Langereis, M. van de Sanden, and W. Kessels. Conformality of plasma-assisted ALD: physical processes and modeling. *J. Electrochem. Soc.*, 157(12):G241–G249, 2010.

[145] S. Larentis, F. Nardi, S. Balatti, D. Gilmer, and D. Ielmini. Resistive switching by voltage-driven ion migration in bipolar RRAM − Part − II: modeling. *IEEE Trans. Electron Devices*, 59(9):2468–2475, 2012.

[146] D. Ielmini, F. Nardi, and C. Cagli. Physical models of size-dependent nanofilament formation and rupture in NiO resistive switching memories. *Nanotechnology*, 22(25):254022, 2011.

[147] C. Walczyk, D. Walczyk, T. Schroeder, T. Bertaud, M. Sowińska, M. Lukosius, M. Fraschke, D. Wolansky, B. Tillack, E. Miranda, et al. Impact of temperature on the resistive switching behavior of embedded-based RRAM devices. *IEEE Trans. Electron Devices*, 58(9):3124–3131, 2011.

[148] E. Hildebrandt, J. Kurian, M. M. Müller, T. Schroeder, H.-J. Kleebe, and L. Alff. Controlled oxygen vacancy induced p-type conductivity in HfO_{2-x} thin films. *Appl. Phys. Lett.*, 99(11):112902, 2011.

[149] M. Vos, P. Grande, D. Venkatachalam, S. Nandi, and R. Elliman. Oxygen self-diffusion in HfO_2 studied by electron spectroscopy. *Phys. Rev. Lett.*, 112(17):175901, 2014.

[150] A. Padovani, L. Larcher, G. Bersuker, and P. Pavan. Charge transport and degradation in HfO_2 and HfO_x dielectrics. *IEEE Electron Device Lett.*, 34(5):680–682, 2013.

[151] N. P. Long, Y. Tanaka, Y. Uesugi, and Y. Yamaguchi. Numerical investigation of the effect of cathode holder shape on hafnium cathode evaporation for an oxygen plasma cutting arc. *J. Phys. D: Appl. Phys.*, 46(22):224012, 2013.

[152] M. A. Panzer, M. Shandalov, J. Rowlette, Y. Oshima, Y. W. Chen, P. C. McIntyre, K. E. Goodson, et al. Thermal properties of ultrathin hafnium oxide gate dielectric films. *IEEE Electron Device Lett.*, 30(12):1269–1271, 2009.

[153] L. Vandelli, A. Padovani, L. Larcher, and G. Bersuker. Microscopic modeling of electrical stress-induced breakdown in poly-crystalline hafnium oxide dielectrics. *IEEE Trans. Electron Devices*, 60(5):1754–1762, 2013.

[154] Y.-C. Huang, W.-L. Tsai, C.-H. Chou, C.-Y. Wan, C. Hsiao, and H.-C. Cheng. High-performance programmable metallization cell memory with the pyramid-structured electrode. *IEEE Electron Device Lett.*, 34(10):1244–1246, 2013.

[155] H.-D. Kim, M. J. Yun, S. M. Hong, and T. G. Kim. Effect of nanopyramid bottom electrodes on bipolar resistive switching phenomena in nickel nitride films-based crossbar arrays. *Nanotechnology*, 25(12):125201, 2014.

[156] D. Lee, J. Song, J. Woo, J. Park, S. Park, E. Cha, S. Lee, Y. Koo, K. Moon, and H. Hwang. Optimized lightning-rod effect to overcome trade-off between switching uniformity and on/off ratio in ReRAM. *IEEE Electron Device Lett.*, 35(2):214–216, 2014.

[157] J. Liang and H. P. Wong. Cross-point memory array without cell selectors-device characteristics and data storage pattern dependencies. *IEEE Trans. Electron Devices*, 57(10):2531–2538, 2010.

[158] W. G. Kim, H. M. Lee, B. Y. Kim, K. H. Jung, T. G. Seong, S. Kim, H. C. Jung, H. J. Kim, J. H. Yoo, H. D. Lee, et al. NbO_2based low power and cost effective 1S1R switching for high density cross point ReRAM application.

In *VLSI Technology (VLSI-Technology): Digest of Technical Papers, 2014 Symposium on*, pages 1–2. IEEE, 2014.

[159] M. D. Pickett and R. S. Williams. Sub-100 fJ and sub-nanosecond thermally driven threshold switching in niobium oxide crosspoint nanodevices. *Nanotechnology*, 23(21):215202, 2012.

[160] X. Liu, S. K. Nandi, D. K. Venkatachalam, S. Li, K. Belay, and R. G. Elliman. Finite element modeling of resistive switching in Nb_2O_5-based memory device. In *Optoelectronic and Microelectronic Materials & Devices (COMMAD), 2014 Conference on*, pages 280–282. IEEE, 2014.

[161] R. C. Weast. Handbook of chemistry and physics. *Am. J. Medical Sciences*, 257(6):423, 1969.

[162] C. J. Amsinck, N. H. Di Spigna, D. P. Nackashi, and P. D. Franzon. Scaling constraints in nanoelectronic random-access memories. *Nanotechnology*, 16(10):2251, 2005.

[163] M. Son, J. Lee, J. Park, J. Shin, G. Choi, S. Jung, W. Lee, S. Kim, S. Park, and H. Hwang. Excellent selector characteristics of nanoscale for high-density bipolar ReRAM applications. *IEEE Electron Device Lett.*, 32(11):1579–1581, 2011.

[164] E. Linn, R. Rosezin, C. Kügeler, and R. Waser. Complementary resistive switches for passive nanocrossbar memories. *Nat. Mater.*, 9(5):403–406, 2010.

[165] R. Waser and M. Aono. Nanoionics-based resistive switching memories. *Nat. Mater.*, 6(11):833–840, 2007.

[166] F. Nardi, S. Balatti, S. Larentis, and D. Ielmini. Complementary switching in metal oxides: toward diode-less crossbar RRAMs. In *Electron Devices Meeting (IEDM), 2011 IEEE International*, pages 31–1. IEEE, 2011.

[167] K. Jacob, C. Shekhar, M. Vinay, and Y. Waseda. Thermodynamic properties of niobium oxides. *Journal of Chemical & Engineering Data*, 55(11):4854–4863, 2010.

[168] J. Gmehling. Thermochemical data of pure substances, Part – I/II. von i. barin. vch, weinheim–new york–basel–cambridge 1989. x, 1 829 s., 10 abb., 2406 tab., geb., dm 680,–. *Chemie Ingenieur Technik*, 62(8):644–644, 1990.

[169] D. Ielmini, F. Nardi, and C. Cagli. Universal reset characteristics of unipolar and bipolar metal-oxide RRAM. *Electron Devices, IEEE Transactions on*, 58(10):3246–3253, 2011.

[170] G. A. Gibson, S. Musunuru, J. Zhang, K. Vandenberghe, J. Lee, C.-C. Hsieh, W. Jackson, Y. Jeon, D. Henze, Z. Li, et al. An accurate locally active memristor model for S – type negative differential resistance in NbO_x. *Appl. Phys. Lett.*, 108(2):023505, 2016.

[171] S. Slesazeck, H. Mähne, H. Wylezich, A. Wachowiak, J. Radhakrishnan, A. Ascoli, R. Tetzlaff, and T. Mikolajick. Physical model of threshold switching in NbO_2 based memristors. *RSC Adv.*, 5(124):102318–102322, 2015.

[172] C. Chen, S. Gao, F. Zeng, G. Tang, S. Li, C. Song, H. Fu, and F. Pan. Migration of interfacial oxygen ions modulated resistive switching in oxide-based memory devices. *J. Appl. Phys.*, 114(1):014502, 2013.